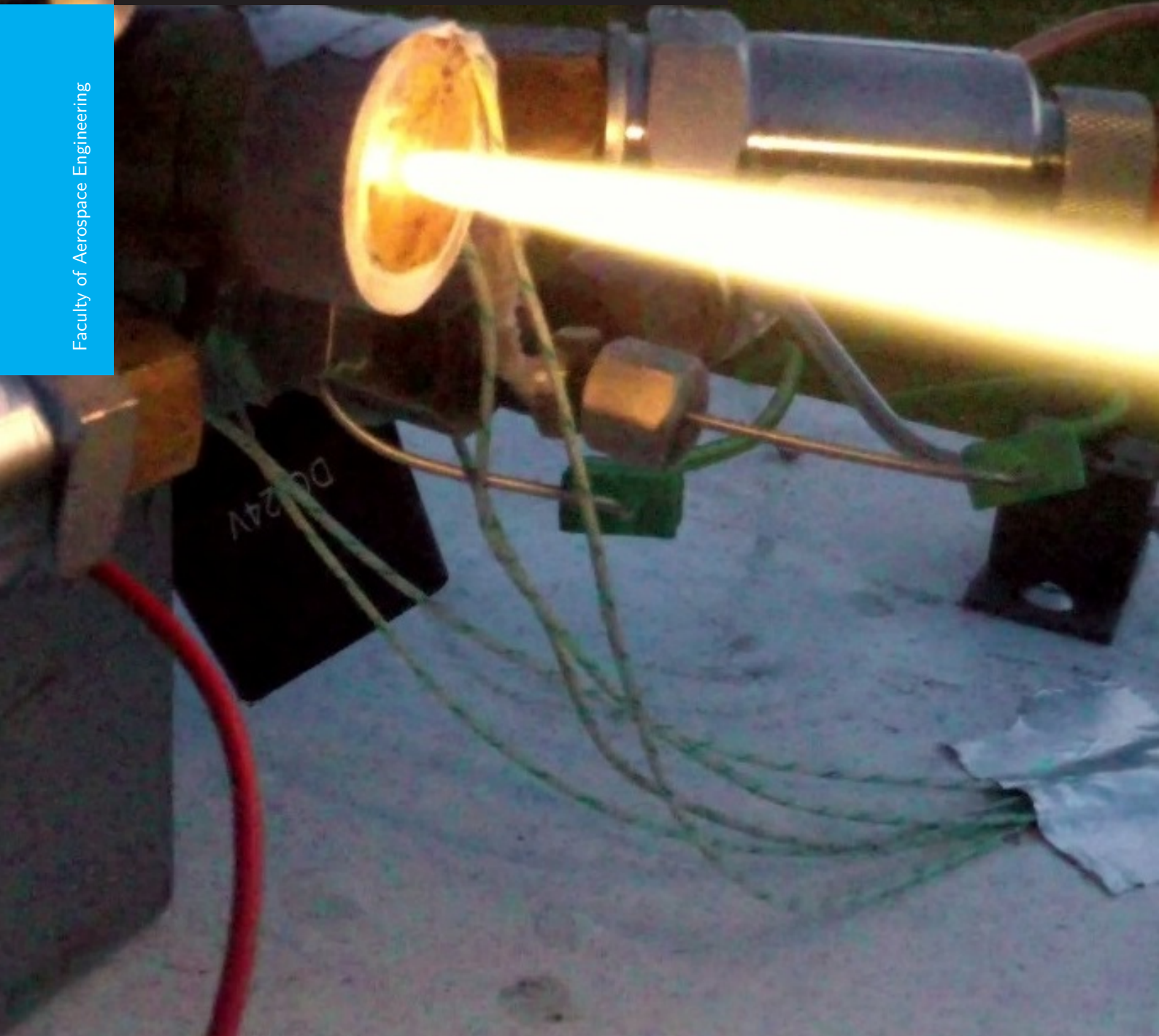


CubeSat Micro-Propulsion

Design and Validation of a Micro Bi-Propellant Rocket Motor

S.J. Powell

Faculty of Aerospace Engineering



CUBESAT MICRO-PROPELLSION

DESIGN AND VALIDATION OF A MICRO BI-PROPELLANT ROCKET MOTOR

by

S.J. Powell

in partial fulfilment of the requirements for the degree of

Master of Science
in Aerospace Engineering

at The Delft University of Technology,
to be defended publicly on Monday November 30, 2015 at 09:30 AM.

Supervisor:	Dr. A. (Angelo) Cervone	TU Delft
Thesis committee:	Prof. E.K.A. (Eberhard) Gill	TU Delft
	Dr. A. (Angelo) Cervone	TU Delft
	Prof. B.A.C. (Boudewijn) Ambrosius	TU Delft

An electronic version of this thesis is available at <http://repository.tudelft.nl/>.

PREFACE

All work conducted in the thesis "CubeSat Micro Propulsion: Design and Validation of a Micro Bi-Propellant Rocket Motor" was carried out in fulfilment of an MSc degree in Space Systems Engineering from The Delft University of Technology. Design and analysis work was carried out at Hyperion Technologies while manufacture and testing was done at Delft Aerospace Rocket Engineering (DARE). The design of the motor was closely coupled with the design of the feedsystem, which was carried out by my colleague and fellow DARE member of 5 years, Tobias Knop. Tobias and myself have been involved in the development of a 10 kN hybrid rocket motor for the Stratos II rocket and thus have a substantial background in rocket propulsion on a practical level. This project was however our first attempt at a motor under 5 N of thrust and thus presented many new challenges which served to keep us motivated over the past 9 months. Tobias Knop has put far more hours into his work than anyone ever asked of him. His hard work has facilitated my research tremendously. Bi-propellants rocket motors don't work without propellants, so for that, I thank him.

This project was undertaken on the request of Steven Engelen of Hyperion Technologies. Steven's enthusiasm for the project is contagious. He was regularly assisting with labour intensive testing and was always very excited to discuss test results as soon as they were available. His TU Delft background also ensured that I stayed focused on producing scientifically valid results.

I would also like to thank my supervisor, Angelo Cervone. Angelo was invaluable in providing critical feedback, particularly in the early stages of the project.

Lastly, I would like to thank my parents for their unrelenting support. Without it, I certainly would not have been able to endure so many years so far away from home.

*S.J. Powell
Delft, November 2015*

CONTENTS

Preface	iii
Glossary	ix
List of Figures	xi
List of Tables	xiii
1 introduction	1
2 Research Objective	3
2.1 Research Questions	3
2.2 Thruster Design Requirements	3
2.3 Thesis goals	4
3 Theoretical Basis	5
3.1 Rocket theory	5
3.1.1 Combustion efficiency	5
3.2 General Rocket motor parameters	6
3.2.1 Characteristic length	6
3.2.2 Contraction ratio	6
3.2.3 Thrust	6
3.2.4 total impulse	7
3.2.5 oxidizer to fuel ratio	7
3.3 Heat transfer	7
4 Design Tools and Modelling	9
4.1 RPA Model	9
4.2 Analytical Thermal Model.	9
4.2.1 Model Purpose	9
4.2.2 Model Description and Assumptions	10
4.2.3 Equations	11
4.2.4 Results	11
4.3 Ansys Model	12
4.3.1 Model description	12
4.3.2 Results	14
5 Experimental Setup	21
5.1 Test bench	21
5.1.1 Feedsystem layout	21
5.1.2 Measurement and control system	22
5.1.3 Pressure sensors	24
5.1.4 Thermocouples	24
5.2 Operations	24
5.3 Motor descriptions	25
5.3.1 Motor 1	25
5.3.2 Motor 2	26
5.3.3 Motor 3	26
5.3.4 Motor 4	28
5.3.5 Spark igniter	28

6 Experimental Results	31
6.1 HypT6, 7 and 8	34
6.2 HypT9.	37
6.3 HypT10	43
6.4 HypT12	48
6.4.1 HypT12-16	48
6.4.2 HypT12-17, Burn #5	53
6.5 Motor burn repeatability	57
6.6 Motor Comparison	60
6.6.1 Startup and shutdown transient	60
6.6.2 $P_{Chamber}$	60
6.7 Minimum impulse bit achieved	63
6.8 Summary	63
6.9 Errors	64
6.9.1 P_c measurement error	65
6.9.2 Throat area.	65
6.9.3 Mass flow measurement	65
6.9.4 Errors summary	66
7 Discussion	67
7.1 Feedsystem related effects	67
7.2 Ignition Characteristics	69
7.3 Noise due to spark igniter	69
7.4 Motor efficiency.	69
7.5 Regenerative Cycle	70
7.6 Comparison to Models	70
7.6.1 Analytical Model	70
7.6.2 Numerical model	71
7.7 Test Repeatability	72
7.8 Evaluation of Requirements	72
8 Application to CubeSats	75
8.1 Thrust and vibrational loading	75
8.2 Thrust vector misalignment.	75
8.3 Thruster plume effects	76
8.4 Thruster Optimization for use in a CubeSat	77
8.4.1 O/F optimization	77
8.4.2 $P_{Chamber}$ optimization.	77
8.5 Electrical requirements	78
8.6 CubeSat manoeuvrability	78
8.7 Vacuum thruster form factor	80
8.8 Thermal design	80
9 Future work	81
9.1 Measurement accuracy	81
9.2 Feed system improvements	81
9.3 Motor Optimization.	82
9.4 Investigate high frequency instability (600Hz)	82
9.5 Further Testing	82
9.6 Requirements verification.	83
9.7 Integration of feedsystem to thruster in a CubeSat configuration	83
10 Conclusion	85
A Hyperion Technology Project Requirements	87
B Keller 23SY Pressure Sensor Data Sheet	89
C DTMTC8 K Type Thermocouple Data Sheet	93

Bibliography	95
--------------	----

GLOSSARY

ADCS	- attitude determination and control system
A_t	- Throat area
C_2H_6	- ethane
CAD	- computer aided design
COTS	- commercial off the shelf
DAQ	- data acquisition system
DARE	- Delft Aerospace Rocket Engineering
DAS	- debris assessment software
EMI	- electromagnetic interference
A_T/A_e	- expansion ratio
g_0	- acceleration due to gravity at sea level, $9.81 \frac{m}{s^2}$
γ	- ratio of specific heats
HDPE	- high-density polyethylene
HTPB	- hydroxyl-terminated polybutadiene
L^*	- characteristic length
N_2O	- nitrous oxide
O/F	- oxidizer to fuel mass ratio
$P_{Chamber}$	- Chamber pressure
PMMA	- poly(methyl methacrylate)
POM	- polyoxymethylene
Pr	- Prandtl number
R	- specific gas constant
RCS	- reaction control system
RPA	- Rocket Propulsion Analysis lite
St	- Stanton number
$T_{Combustion}$	- adiabatic flame temperature
TRL	- technical readiness level
TVC	- thrust vector control

LIST OF FIGURES

4.1 Theoretical maximum specific impulse, expansion ratio (A_T/A_e) = 100, $P_{Chamber}$ = 15 bar	10
4.2 Analytical thermal model output. Contraction ratio of 100, chamber wall thickness = 1mm, Conductive coefficient = 380 W/mK (Copper)	11
4.3 Temperature and total heating power vs function of contraction ratio for a 4N N_2O Ethane thruster, 1mm wall, Conductive coefficient = 120 W/mK (Brass)	12
4.4 Plot of simulation solution vs number of elements used in the simulation.	14
4.5 Unlike impinging injection temperature profile	15
4.6 Unlike impinging injection Streamline (side view)	15
4.7 Unlike impinging injection Streamline (top view)	15
4.8 CoAx Swirl temperature profile distribution	16
4.9 CoAx Swirl oxidizer streamlines and profile	16
4.10 CoAx Swirl fuel streamlines and profile	16
4.11 L^* vs N_2O fraction for various thruster configurations	17
4.12 CoAxS-0.5-0.5-4-40 temperature profile distribution	17
4.13 CoAxS-0.5-0.5-4-40 streamlines	17
4.14 CoAxS-0.5-0.5-4-40 oxidizer streamlines and profile	18
4.15 CoAxS-0.5-0.5-4-40 fuel streamlines and profile	18
4.16 Motor 1 fluid temperature profile	19
4.17 Motor 1 fluid streamlines	19
4.18 Motor 1 oxidizer profile	19
4.19 Motor 1 fuel profile	19
4.20 Motor 4 fluid temperature profile (1000-3300K)	20
4.21 Motor 4 fluid temperature profile (600-1000K)	20
4.22 Motor 4 oxidizer profile	20
4.23 Motor 4 fuel profile	20
5.1 The test bench as setup for a hotfire test	22
5.2 Feedsystem schematic layout	23
5.3 DAQ system used for control and data acquisition during testing	23
5.4 LabView GUI used to control the test bench	24
5.5 Motor 1 section view displaying major features	26
5.6 Motor 1 oxidizer injector and electrode assembly	27
5.7 Motor 1 fuel injector slots showing inconsistency in manufacture. Fuel slots are 0.13mm deep	27
5.8 Motor 2 section view displaying major features	28
5.9 Motor 3 section view displaying major features	29
5.10 Motor 4 section view displaying major features	29
5.11 Rimfire Z3 spark plug (dimensions in inches)	30
6.1 Pressure data of HypT7-10	35
6.2 Temperature data of HypT7-10	35
6.3 Spectrogram of chamber pressure of HypT7-10	36
6.4 Pressure data of HypT9-6	38
6.5 Pressure data of HypT9-6, close-up at 1.3s	38
6.6 Pressure data of HypT9-6, close-up at 11s	39
6.7 Spectrogram of combustion pressure of HypT9-6	39
6.8 Spectrogram of oxidizer injector pressure of HypT9-6	40
6.9 Spectrogram of fuel injector pressure of HypT9-6	40
6.10 Mass flow data of HypT9-6	41
6.11 C Star performance data of HypT9-6	41

6.12 Motor 2 before and after HypT9-6	42
6.13 Pressure data of HypT10-8	44
6.14 Spectrogram of combustion pressure of HypT10-8	44
6.15 Mass flow data of HypT10-8	45
6.16 Temperature data of HypT10-8	45
6.17 Calculated cooling power in regenerative cycle of HypT10-8	46
6.18 C Star performance data of HypT10-8	46
6.19 Motor 3 cross-section after the HypT10 test series.	47
6.20 Pressure data of HypT12-16	49
6.21 Spectrogram of combustion pressure of HypT12-16	49
6.22 Mass flow data of HypT12-16	50
6.23 Temperature data of HypT12-16	50
6.24 Calculated total heating power during HypT12-16	51
6.25 C Star performance data of HypT12-16	51
6.26 Calculated vacuum thrust performance of HypT12-16. $\frac{A_e}{A_t} = 150$, nozzle efficiency factor = 0.96.	52
6.27 Pressure data of HypT12-17, Burn #5	53
6.28 Spectrogram of combustion pressure of HypT12-17, Burn #5	54
6.29 Mass flow data of HypT12-17, Burn #5	54
6.30 Temperature data of HypT12-17, Burn #5	55
6.31 C Star performance data of HypT12-17, Burn #5	55
6.32 Calculated vacuum thrust performance of HypT12-17, Burn #5. $\frac{A_e}{A_t} = 100$, nozzle efficiency factor = 0.96.	56
6.33 Chamber Pressure Comparison of HypT12-17 Burns 3, 4 and 5	57
6.34 Propellant Mass Flow Comparison of HypT12-17 Burns 3, 4 and 5	58
6.35 C* Efficiency Comparison of HypT12-17 Burns 3, 4 and 5	58
6.36 Nozzle Surface Temperature Comparison of HypT12-17 Burns 3, 4 and 5	59
6.37 Chamber Pressure Comparison of Motors 2, 3 and 4 (HypT9-4, HypT10-8, HypT12-17-5)	60
6.38 Chamber Pressure Comparison of Motors 2, 3 and 4 at Startup (HypT9-4, HypT10-8, HypT12-17-5)	61
6.39 Propellant Mass Flow Comparison of Motors 2, 3 and 4 (HypT9-4, HypT10-8, HypT12-17-5)	61
6.40 C* Efficiency Comparison of Motors 2, 3 and 4 (HypT9-4, HypT10-8, HypT12-17-5)	62
6.41 Minimum impulse bit achievable with Motor 4, as demonstrated in HypT12-17, burn 5.	63
8.1 Plume characteristics in the space environment [29]	76
8.2 Angle of plume from centre axis for a 10N MON-1/MMH thruster [31]	77
8.3 debris assessment software (DAS) output showing the ΔV requirements for a transfer from 450 to 520 km circular orbit transfer	79
8.4 Motor 4 configured for vacuum operation, $\frac{A_e}{A_t}=100$, 80% length bell shaped	80

LIST OF TABLES

4.1 Results summary of injector modelling	15
4.2 Summary of CoAx swirl injector geometry types analysed	16
5.1 The eight pressure transmitters of type 'Keller PAA-23SY/XXbar/81549.77' with 4-20 mA output along with their range and location in the test setup.	24
5.2 Motor parameters for motors 1 to 4	25
6.1 Test summary	32
6.2 Test summary (continued)	33
6.3 HypT12-17 burns 3,4 and 5 performance summary	57
6.4 Motors 2, 3 and 4 test summary. All data taken from tests HypT9-6, HypT10-8, HypT12-16 and HypT12-17-5	64
6.5 Pressure measurement error summary	65
6.6 C* error summary	66
7.1 A comparison of experimentally and numerically determined parameters for Motor 4 during HypT12-16	72

1

INTRODUCTION

Nano Satellites have become of interest to satellite manufacturers since the benefit of swarm satellite technologies has become more apparent [1]. A swarm of nanosatellites would call for a group of up to 50 or sometimes 500 satellites to act as a single orbiting constellation, providing greater coverage and faster update rates than can be achieved using conventional single satellite operations. In order for tens or even hundreds of satellites to be used in a swarm, it is beneficial to use a standard platform to achieve economies of scale. A popular format in recent times is the CubeSat platform. CubeSats are a concept developed at California Polytechnic State University and Stanford University in 1999 [2]. They are designed to allow the satellite designer to utilize a standardised platform for which there are a significant number of standard components such as cameras, batteries, solar panels, ACDS and flight computers available as 'plug and play' components. In recent years, this satellite platform has become increasingly popular with subsystems even being sold by online vendors such as ISIS, ClydeSpace and Pumpkin.

As of yet, there are very few practical CubeSat propulsion systems. Some systems do exist, however they are either use highly toxic propellants [3][4] or are characterised by low specific impulse, low impulse density propellants such as cold gas systems [5]. The resulting systems typically have very low total impulse, sometimes as low as 1 Ns. On a 3U CubeSat, such a system can only provide a total ΔV of approximately $0.25 \frac{m}{s}$. While this is a good proof of concept for CubeSat based propulsion, it does not provide the performance required to allow a CubeSat to perform manoeuvres typical of larger satellites such as inclination changes and orbit raises. As a result, CubeSats are currently limited to missions where very little or no control over orbital parameters is required. This is very restrictive to the mission designer, especially considering that the vast majority of CubeSats cannot select their orbital injection parameters as they are typically secondary payloads to much larger satellites. Often this means injection into an orbit of less than 400 km altitude, where orbital lifetime can be less than 2 years due to aerodynamic drag [6]. Many Cubesats which operate in these low orbits intend to perform orbit maintenance, either to extend mission life at low orbits or to maintain a formation [7]. Current CubeSat propulsion systems do not allow for significant lifetime gains when a low performance propulsion system is installed. If a CubeSat could be outfitted with a high ΔV propulsion system, the mission designer would be much more at liberty to select some orbital parameters as he/she desires regardless of whether a dedicated launch was used or not. Formation flying and orbit maintenance become practical realities, massively increasing the operational flexibility and capability of the CubeSat. As CubeSats mature, their capabilities are being extended to include high performance sensory equipment for earth observation purposes. This makes increasing the propulsion capabilities of the CubeSat all the more imperative to maximising the useful life and hence profitability of the satellite.

Hyperion Technologies is a Delft based high performance attitude determination and control system ([ADCS](#)) component manufacturer for CubeSats. CubeSats require a high level of component integration to allow for volumetrically efficient designs. For this reason, it is useful to extend the [ADCS](#) capability to include a thruster capable of performing substantial orbital manoeuvres such as orbit raising. It is Hyperion's intention to develop this capability in-house by developing a bi-propellant thruster system capable of $100\text{-}300 \frac{m}{s} \Delta V$ for a 6U system whereby 2U is occupied by the [ADCS](#) and thruster system. It has been determined by Hyperion Technologies in previous studies that such a system should be of approximately 4N thrust in

vacuum and utilize nitrous oxide (N_2O) and ethane (C_2H_6) in a bi-propellant configuration. It is based on these design parameters that this thesis begins.

This thesis report details the design and performance verification of a prototype thruster intended to meet the requirements set by Hyperion Technologies. Four separate motors have been designed and tested using a variety of analytical and numerical multi physics tools. These motors were then manufactured and tested at the TU Delft using the testing facilities and equipment at Delft Aerospace Rocket Engineering ([DARE](#)).

Section 2 outlines the research questions which this thesis will attempt to answer. Section 3 describes the theoretical bases used to design the thruster as well as process the acquired test data. Section 4 presents the tools and models used in the design of the thruster. Section 5 focuses on the experimental setup used to test motors as well as presenting the motor designs themselves. Section 6 presents the experimental results of four motors tested over 7 test campaigns. These results are then discussed at length in Section 7.

While this thesis focuses on the design and validation of the thruster, it is also interesting to the satellite designer to understand the requirements a thruster would impose on the wider satellite. Section 8 explores these effects in detail.

Due to a paucity of time, not all elements of the project could be completed under the construct of a single thesis. Section 9 identifies the areas of the project that require more work to bring the system to a complete working prototype stage and later to flight-ready hardware.

2

RESEARCH OBJECTIVE

The objective of this thesis is set out in this chapter. Firstly, the research questions will be presented followed by a short discussion on the thruster design requirements. Finally, the specific goals of the thesis will be defined such that the intended output of this thesis is well defined.

2.1. RESEARCH QUESTIONS

At the conclusion of the literature study [8], four research questions were proposed. They intend to encompass the core research objectives of this thesis.

1. Can a nitrous oxide/ethane bi-propellant thruster of 4 N satisfy the requirements set by Hyperion technologies?
2. What are the critical design parameters of such a thruster and how do they affect performance?
3. How does such a thruster perform and how does this compare to the design models used?
4. How could such a system be used effectively in a 6U CubeSat configuration?

2.2. THRUSTER DESIGN REQUIREMENTS

Hyperion Technologies defined a set of requirements which determined the literature study preceding this thesis [8]. Based on the findings of the literature study, these requirements can now be rewritten to make use of new information. Note that requirements such as performance parameters (thrust rating, minimum impulse bit, I_{sp}^{Vac} etc.) and propellant selection have been determined by Hyperion Technologies and are now considered requirements of the systems the thesis is focused on. Most notably, a requirement on time schedule has been added to reflect the need to develop the system within a tight time frame. This is seen as a driving requirement.

1. The system shall have a thrust rating of 4 N.
2. The system shall have a minimum impulse bit of 1 Ns.
3. The system shall have an impulse bit repeatability of better than 10%.
4. The system shall have an I_{sp}^{Vac} in excess of 230 s.
5. The system shall have a maximum single burn time in excess of 100 s.
6. The system shall have a total burn lifetime in excess of 1000 s.
7. The system shall be restartable in excess of 1000 times.
8. The system shall have thrust vector capability of +/- TBD degrees.
9. The system shall not cause adjacent components to become hot to the extent that they cannot reasonably function.
10. The system shall fit inside a 2U CubeSat slot.
11. The system shall be compatible with an ISIS, Clydespace and Pumpkin 6U CubeSat layout.

12. The system shall be manufacturable.
13. The system shall be a working prototype by the 31st of August 2015.

2.3. THESIS GOALS

From the requirements and research questions, a number of goals can be determined. These goals are specific tasks to be performed during the research and should result in the completion of the project as a whole.

- Analyse the thruster design space and find how the system can be optimised with respect to top level requirements.
- Provide a subset of thruster concepts according to the determined optimization.
- Perform detailed design of the selected thruster concept
- Develop a thermal model of the motor
- Determine injector design
- Model internal ballistics of motor
- Model thruster in CAD
- Manufacture thruster
- Experimentally determine the following characteristics of the proposed thruster:
 1. Start-up behavior
 2. Minimum impulse bit
 3. Long duration burn behavior
 4. Total burn lifetime
 5. Restart capability
 6. C* performance
- Analyse results
- Iterate the motor design to improve performance as required
- Present results

The overarching objective of this thesis is to increase the technical readiness level ([TRL](#)) of CubeSat bi-propellant thruster technology. To these ends, an engineering approach to design will be taken. This means that not all design avenues will be explored as would be done if a rigorous scientific method was followed. This is done to reduce the development time of the system as much as reasonably possible. Hence time consuming parametric studies will be avoided in favour of finding a solution which meets requirements while minimizing development risk. While this does not mean that scientific method can be neglected altogether, it means that in some cases, phenomena which require too much investment to understand for little yield in terms of motor performance will be avoided in design all together.

By the end of the thesis, a working prototype should have been built according to a sound design scheme. The performance of the prototype should be well understood. The applicability of this thruster to a CubeSat should be elaborated on and the shortcomings of the motor be identified. Finally, direction for future work should be provided. These activities should all be presented in a technical report.

3

THEORETICAL BASIS

The theoretical basis sets out the formula used in the design and analysis of the proposed motor. These formulas largely come from standard rocket propulsion theory which has been well understood since the early 1950's and has been put into practice over the last 60 years. Therefore, standard literature on the subject is commonly available.

3.1. ROCKET THEORY

General rocket theory is well covered by the works of Sutton [9] in the books 'Rocket Propulsion Elements', Barrere [10] in the Book 'Rocket Propulsion' and Huzel in the book 'Design of Liquid Rocket Engines' [11]. These works are further supplemented through the 'Thermal Rocket Propulsion' course notes of Barry Zandbergen of the TU Delft [12].

3.1.1. COMBUSTION EFFICIENCY

Combustion efficiency, or C^* efficiency is the measure of how efficient the combustion process is inside the chamber. It is defined in Equation 3.1. It is typically displayed as a percentage and is hence multiplied by 100.

$$C_{Efficiency}^* = \frac{C_{Experimental}^*}{C_{Theoretical}^*} * 100 \quad (3.1)$$

C^* is defined as in Equation 3.2.

$$C^* = \frac{\sqrt{\gamma R T_{Combustion}}}{\gamma * \sqrt{\frac{2}{(\gamma+1)^{\gamma-1}}}} \quad (3.2)$$

As shown in Equation 3.2, C^* is a function of the ratio of specific heats (γ), the specific gas constant (R) and the adiabatic flame temperature ($T_{Combustion}$). C^* scales with the square root of R and $T_{Combustion}$ while the relation to γ is more complex. All three parameters can be determined theoretically for a given propellant combination and O/F ratio. While this can be done analytically using standard methods found in literature [12], there are freely available programs such as RPA which allow the designer to perform such computations quickly. $C_{Theoretical}^*$ was thus computed using such a chemical equilibrium program. More details on RPA can be found in Section 4.1.

γ , R and $T_{Combustion}$ cannot be easily experimentally determined, thus the second definition of C^* is used as shown in Equation 3.3.

$$C^* = \frac{P_{Chamber} * A_t}{\dot{m}_{propellant}} \quad (3.3)$$

$P_{Chamber}$ is the pressure of combustion at the nozzle entrance and is measured experimentally. Throat area (A_t) is the area of the nozzle throat. It is not measured but rather assumed to be defined by the tooling used to machine it and consequently is subject to machining errors.

$\dot{m}_{propellant}$ is the total mass flow of propellants into the motor and is defined by Equation 3.4.

$$\dot{m}_{propellant} = \dot{m}_{fuel} + \dot{m}_{oxidizer} \quad (3.4)$$

$\dot{m}_{oxidizer}$ and \dot{m}_{fuel} are the mass flows of oxidizer and fuel into the motor. They are determined using subsonic isentropic flow relations across the injector orifice. These relations assume the fluid is of a single phase. This assumption can be made as both fuel and oxidizer are brought a significant distance from their saturated vapour point before injection into the motor. This assumption is verified with pressure and temperature measurements of both propellants at the injector inlet.

The subsonic isentropic flow relation used to determine the instantaneous mass flow is given in Equation 3.5 [13].

$$\dot{m}_{fuel} = A_{Fuel\ Injector} * C_{d\ inj\ fuel} * \sqrt{\frac{2\gamma}{\gamma-1} * \rho_{fuel} * P_{Fuel\ Injector} * \left(\frac{P_{Chamber}}{P_{Fuel\ Injector}} \right)^{\frac{2}{\gamma}} - \left(\frac{P_{Chamber}}{P_{Fuel\ Injector}} \right)^{\frac{\gamma+1}{\gamma}}} \quad (3.5)$$

$A_{Fuel\ Injector}$ is the area of the fuel injector and determined at manufacture in much the same way as A_t . $C_{d\ inj}$ is the discharge coefficient of flow of the injector orifice. It is the ratio of the actual discharge to the theoretical discharge. $C_{d\ inj}$ can typically vary from 0.5 to 0.9 depending on the orifice inlet shape, surface roughness and length/diameter ratio. The injector inlets used in this research are counter drilled to a 120° cone angle. The experimental work of N. Hay [14] for a tapered inlet orifices specify a value of 0.82 as appropriate for the inlet geometry and flow conditions used. This value is used for both the fuel and oxidizer injector orifices.

ρ_{fuel} is the density of the propellant. Along with γ , it can be determined using the open source code 'Coolprop' [15]. The required input for Coolprop to calculate these parameters is the fluid type, temperature, pressure and phase. Both pressure and temperature are experimentally determined while the phase is assumed to be gaseous as previously stated. Both the fuel and oxidizer mass flow are determined using the same basic methodology.

Using the above set of formula, the $C*_{Efficiency}$ can be evaluated at every data point and hence a curve of the $C*_{Efficiency}$ can be produced.

3.2. GENERAL ROCKET MOTOR PARAMETERS

3.2.1. CHARACTERISTIC LENGTH

The characteristic length (L^*) of the chamber is a parameter used to allow the designer to size the appropriate chamber volume for the given amount of propellants being burnt. The definition of L^* is given in 3.6 .

$$L^* = \frac{V_c}{A_t} \quad (3.6)$$

V_c is defined as the volume of the chamber, typically starting from the injector face until the plane of the nozzle throat. This definition has been maintained here however it is interesting to note that on a small engine such as is the topic of this thesis, the volume in the injector element which does not contribute to the calculated L^* is much larger than that typical of a kN sized engine.

3.2.2. CONTRACTION RATIO

The contraction ratio is the ratio of chamber cross-section area, A_1 to nozzle throat area A_t , as shown in Equation 3.7

$$Contraction\ ratio = \frac{A_1}{A_t} \quad (3.7)$$

3.2.3. THRUST

The thrust generated is not measured and hence is calculated using rocket theory. This is done with Equation 3.8 where ξ_F is the nozzle efficiency, typically taken to be 0.92 to 0.96 [9] or 0.92 to 1 [11]. A value of 0.96 is used for the purposes of this thesis.

$$F = C * \text{Efficiency} * \xi_F * I_{sp \text{ theoretical vac}} \frac{A_e}{A_t} = 100 * g_0 * \dot{m}_{propellant} \quad (3.8)$$

$I_{sp \text{ theoretical vac}} \frac{A_e}{A_t} = 100$ is determined by RPA for an expansion ratio of 100 in vacuum.

3.2.4. TOTAL IMPULSE

The total impulse of a given burn is calculated using Equation 3.9.

$$\text{Total impulse} = \text{Thrust} * t_{burn} \quad (3.9)$$

In practice, the thrust varies and so Equation 3.9 is evaluated at every measurement instance and summed over the entire burn. In this way, the experimental thrust curve can be integrated to find the total impulse.

3.2.5. OXIDIZER TO FUEL RATIO

The O/F is determined directly from the experimentally determined propellant mass flows as in Equation 3.10.

$$O/F_{ratio} = \frac{\dot{m}_{oxidizer}}{\dot{m}_{fuel}} \quad (3.10)$$

3.3. HEAT TRANSFER

Heat transfer of the combustion products to the wall and then further onto the cooling fluid was determined analytically for the use in a first order thermal analysis tool as described in Section 4.2.

For the analytical thermal model described in Section 4.2, heat transfer was modelled using the set of equations below. Radiative and conductive heat transfer were neglected for the purposes of this model. Although it is known that they can contribute up to 20% of total heat transfer [9] [12], it was not considered necessary to include these contributions in order to obtain a preliminary model. Hence only convective heat transfer has been taken into account. Convective heat transfer follows from Newtons' law of cooling, as shown in Equation 3.11.

$$q_a = h_a * (T_S - T_r) \quad (3.11)$$

Where:

- q_a = convective heat flux
- h_a = convective heat transfer coefficient
- T_S = surface temperature
- T_r = fluid reference temperature

q_a is determined via the Stanton number (St) method. St is defined as the ratio of heat transferred by convection compared to the total heat contained in the fluid flow. For gases, St can be written as in Equation 3.12.

$$h_a = \rho_{fluid} * v * C_p * St \quad (3.12)$$

Both ρ_{fluid} and C_p are obtained from RPA and hence St can be used to determine h_a . St is determined using Equation 3.13.

$$St = a * Re_D^{-1/5} * Pr^{-\frac{2}{3}} \quad (3.13)$$

'a' is taken to be 0.023 as per Cornelisse et al [16]. The Prandtl number (Pr) is determined using the gas approximation, Equation 3.14

$$Pr \approx \frac{4\gamma}{9\gamma - 5} \quad (3.14)$$

The Reynolds number is determined using the standard definition as given in Equation 3.15 where the dynamic viscosity, μ , and ρ can be found from RPA, and x is taken as the diameter of the chamber.

$$Re_x = \frac{\rho * v * x}{\mu} \quad (3.15)$$

Using the above formula, the total heat flux can be determined through the wall for a given set of T_S and T_r . For the high temperature heat transfer side, ie from the combusting fluid to the chamber wall, T_r is defined as the average of the adiabatic flame temperature and the wall temperature as shown in Equation 3.16

$$T_r = \frac{T_S + T_{flame}}{2} \quad (3.16)$$

From the above set of equations, the heat flux, q_α can be determined. The temperature change across the wall to the regenerative fluid can be determined using Equation 3.17 where K is the conductive heat transfer coefficient as found in literature [17] and L is the chamber wall thickness which was a user input of the model.

$$\Delta T_{wall} = q_\alpha * -\frac{L}{K} \quad (3.17)$$

Heat transfer from the chamber wall to the coolant can be calculated in much the same way as was calculated from the combusting fluid to the wall. As radiation of the motor to the ambient environment is neglected, the coolant is assumed to absorb all heat generated by the motor. Hence, the coolant temperature can be calculated. The total heat generated over a discretized chamber section is calculated using Equation 3.18 where L is the linear length of a single discretized section.

$$Q = q_\alpha * L \quad (3.18)$$

The change in coolant temperature, $\Delta T_{coolant}$ over a discretized section of chamber can then be calculated as in Equation 3.19

$$\Delta T_{coolant} = \frac{Q * \dot{m}_{coolant}}{C_p \text{ coolant}} \quad (3.19)$$

The change in coolant temperature can then be integrated over the entire length of the chamber to yield the bulk coolant temperature at the end of the regenerative cooling cycle.

4

DESIGN TOOLS AND MODELLING

This section will detail the models used in the design of the proposed motor. Three tools were predominately used; a chemical equilibrium analysis tool, [RPA](#); a 1D excel based analytical thermal model; and a multi-physics model using Ansys 14.5. This section will describe these models, their purpose in the design process, and the results of the models.

4.1. RPA Model

[RPA](#) is chemical equilibrium tool intended for use in conceptual and preliminary design to rocket systems. It allows the designer to determine the theoretical performance of a system based on user input of propellants, O/F and $P_{Chamber}$. [RPA](#) assumes perfect combustion and therefore outputs maximum theoretical performance figures.

For the purposes of this thesis, [RPA](#) was used to determine the optimum O/F for the selected propellants. This was done by performing a nested calculation whereby theoretical performance is calculated for a set of O/F values. This was performed for a $P_{Chamber}$ of 15 bar and an A_T/A_e of 100. Figure 4.1 was produced as a result. From this curve it can be determined that performance is optimum at an O/F of 10. Using this value, the mass flow rates of both N_2O and C_2H_6 can be determined through the use of this simple fraction.

[RPA](#) also was used to determine the characteristic velocity of the motor at ideal O/F which was found to be 1564 m/s. The flame temperature, ratio of specific heats and other fluid properties in the chamber, throat and nozzle were also determined to use as input for the analytical thermal model.

4.2. ANALYTICAL THERMAL MODEL

It is known from literature that high heat transfer in small bi-propellant motors can lead to problems such as flame quenching and high motor temperatures [18]. To approximate the thermal loads, a simple analytical model was formulated.

4.2.1. MODEL PURPOSE

The primary purpose of the tool was to obtain the following parameters at equilibrium operation:

- the maximum temperatures in critical locations (nozzle throat, chamber wall, convergent and divergent sections)
- total heat flux
- total temperature of the coolant
- optimum contraction ratio of the chamber to minimize total heat flux

The maximum temperatures in the motor is useful to know as this often drives the material selection. Higher temperatures typically require more specialist materials. The total heat flux is useful to know as it defines how much waste heat the combustion process is generating. If the motor is to operate at thermal equilibrium, this heat must be rejected in some manner, either through regenerative cooling where by one of the propellants is passed through a heat exchanger to recover heat before being injected into the motor, or

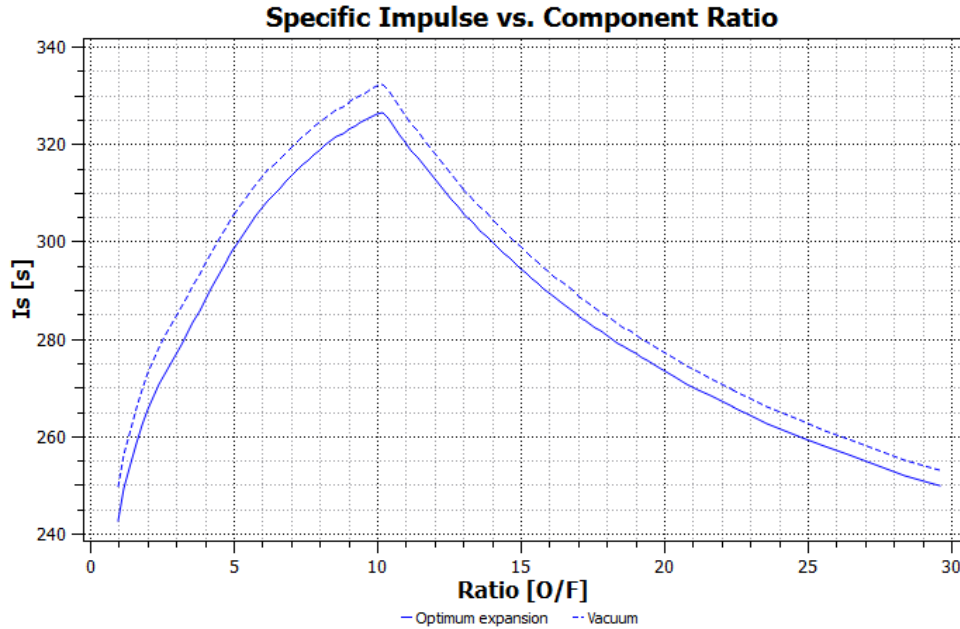


Figure 4.1: Theoretical maximum specific impulse. $A_T / A_e = 100$. $P_{Chamber} = 15$ bar.

through passive cooling means such as radiative cooling. Alternatively, if thermal equilibrium is not required, capacitive cooling can be used whereby the heat is stored in the motor casing. This results in a progressive increase in the chamber temperature until the motor is shut down. The motor requirements specify a burn time of 100s, thus capacitive cooling is not considered an option. Ablative cooling was not considered appropriate for in-space propulsion due to throat erosion which can lead to variable performance which would likely violate requirement 3, "The system shall have an impulse bit reproducibility of better than 10%". The coolant, N_2O is a mono-propellant, meaning it can decompose exothermically. It is also used as the coolant. It is therefore interesting to know the total temperature of the coolant to ensure it stays sufficiently far from its temperature of spontaneous decomposition. The contraction ratio is the ratio

4.2.2. MODEL DESCRIPTION AND ASSUMPTIONS

The model was made in excel, using a marching approach starting at the nozzle exit. The motor was discretized into 40 elements of 0.5mm or less per element, depending on the contraction ratio selected. The system states of each element was computed at beginning and end of each segment.

The system constants are listed below.

- Bulk combustion gas properties at chamber, throat and nozzle exit. (temperature, γ , viscosity, density, velocity) (output of RPA)
- Coolant properties (massflow, specific heat, viscosity, density etc)
- Chamber volume
- Nozzle geometry (diameter, convergent and divergent angles)
- Propellant mass flows and O/F

The bulk combustion gasses are modelled as constant in three separate locations; the chamber, nozzle throat and nozzle exit. Linear interpolation is done between locations to take the convergent and divergent sections of the chamber into account. No allowance is made for local effects such as non-uniform combustion temperature, flow velocity, or other non-linear fluid property variations.

The coolant properties were taken for N_2O at 288 K, at 12 bar pressure. The properties of N_2O change significantly with temperature. These effects are neglected for the purposes of this analysis in order to keep the analysis simple. It is recognised that this is a source for significant error, in particular the effect of a shifting specific heat has a direct effect of the accuracy of the thermal model.

User inputs are listed below.

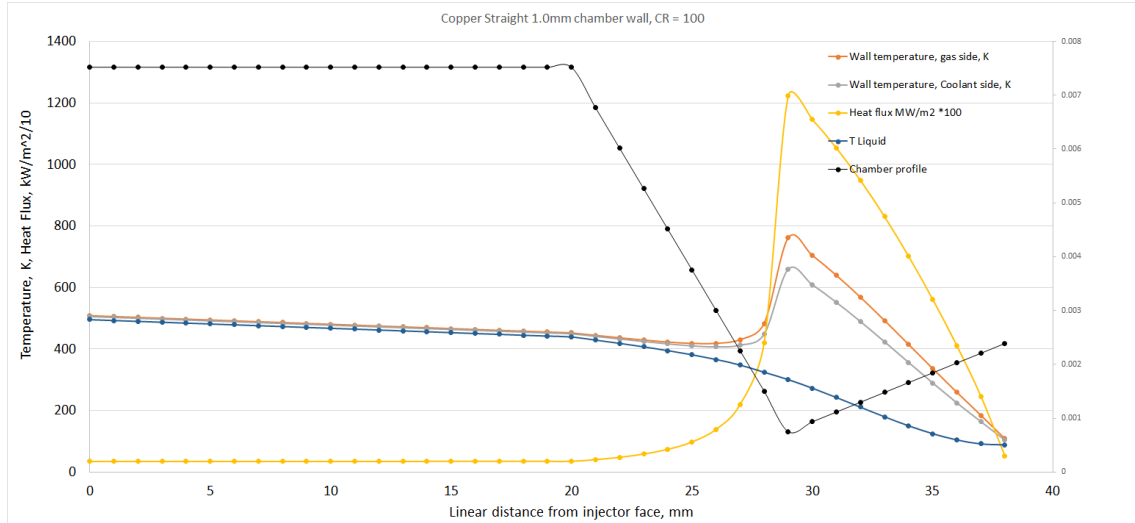


Figure 4.2: Analytical thermal model output.
Contraction ratio of 100, chamber wall thickness = 1mm, Conductive coefficient = 380 W/mK (Copper)

- Contraction ratio (diameter and length are exchanged to maintain a fixed volume)
- Regenerative cooling channel geometry
- Chamber wall thickness
- Chamber wall material properties (Coefficient of conductivity)

The output at each element is given below. This data was then plotted along the contour of the chamber to allow for intuitive data interpretation. The output parameters are given below.

- average heat flux
- wall temperature (gas and coolant side)
- bulk coolant temperature
- total heating power of combustion

4.2.3. EQUATIONS

The equations used in this model have been presented in Section 3.3. They outline the method used to determine the total heat transferred to the cooling fluid as well as the maximum temperatures found in the motor. Note that only convective heat transfer was calculated. This is also elaborated on in Section 3.3.

4.2.4. RESULTS

The model was used to create a profile of the chamber with fluid and wall temperatures displayed as a function of distance from the injector face. This would allow the designer to visualise the temperature profile in the chamber. See Figure 4.2.

The key parameters recorded were the maximum temperature in the chamber, which was typically found at the nozzle throat, and the total heating power of the motor. These values were compiled for contraction ratios ranging from 2 to 500 in order to find a local optimum. This resulted in Figure 4.3 where it can be seen that the minimum temperature in the motor is found for when the contraction ratio is approximately 50. The coolant temperature, as well as motor length both decrease with increasing contraction ratio, both of which properties are advantageous for a CubeSat thruster. Hence, it is wise to set a maximum allowable temperature based on the material selected. At this early stage in the project, it was thought that copper alloys were best suited for manufacturing due to their high conductivity and flight heritage in liquid propulsion. It is known that copper alloys display good mechanical properties at temperatures below 900K, and hence a temperature limit of 900K was selected [19]. From this limit, it can be seen that the maximum allowable contraction ratio becomes approximately 100, as shown in Figure 4.3. At this ratio, there is also very little to gain in terms of

chamber length and minimising coolant temperature properties, hence this choice was most suitable.

Note that the contraction ratio for which the minimum motor temperature is found is dependent on the material conductivity. This is because the thickness of the nozzle wall varies at the throat such that the outer profile of the motor is kept straight. Consequently, a higher contraction ratio also results in a thicker chamber wall at the nozzle throat and thus a higher maximum temperature at the throat. A lower conductivity material will also result in a higher nozzle throat temperature to occur for the same contraction ratio, thus the contraction ratio at which the minimum motor temperature is found changes.

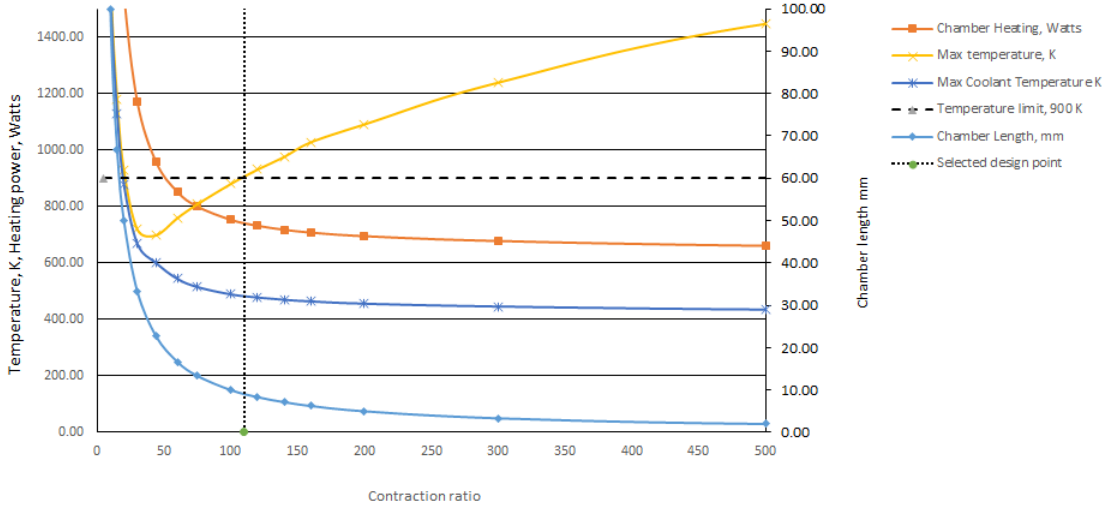


Figure 4.3: Temperature and total heating power vs function of contraction ratio for a 4N N_2O Ethane thruster, 1mm wall, Conductive coefficient = 120 W/mK (Brass)

The analytical model described here provided the rationale for sizing of the critical parameters such as contraction ratio and a first order estimate of what materials would be practicable. From the model, it was determined that a contraction ratio of 100 was appropriate and that copper alloys would be used. This allowed the designer to produce a first order chamber geometry design which would input into the next model, the numerical Ansys model.

4.3. ANSYS MODEL

The numerical model was based in Ansys 14.5, utilizing simulation code for fluid dynamics, combustion and heat transfer modelling. It allowed the designer to assess critical operating parameters of the motor as listed below. Note that these parameters are not exhaustive but were the main parameters used in performance analysis.

- Combustion efficiency (C^*)
- Maximum chamber wall and throat temperature
- Maximum coolant temperature
- Injector pressure drop
- Regenerative cooling cycle pressure drop

These parameters were required in order to determine if a given design was firstly adequate to satisfy the given requirements as well as to provide some quantitative performance parameters for injector concept analysis, for which there are very few ‘standard designs’ or ‘rules of thumb’.

4.3.1. MODEL DESCRIPTION

The model was made using Ansys CFX 14.5. The setup was largely based on the work of Padova University where hybrid rocket motors were modelled as gas/gas injection bi-propellant engines [20] [21]. These

models have been cited as sufficient for assessing combustion efficiencies to within 5.5% with a tendency to over-predict in both efficiency and combustion temperature. Although these models were developed for hybrid rocket motors, they are very well suited to simulation of gas/gas bi-propellant motors. This is because the hybrid motor is actually approximated as a gas/gas bi-propellant motor. Furthermore, DARE has previous experience using these models for their own motor development and thus, little time was required to learn how to apply the model to this specific problem.

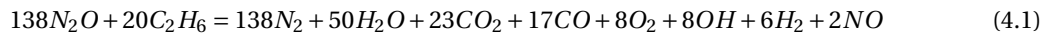
The oxidizer enters the motor at the regenerative cycle inlet as a gas where it encounters a hot chamber. It exits the cycle and then enters the oxidizer injector. The fuel is injected directly into the motor. The reactants then meet and combust, generating reaction products as defined in equation 4.1 and heat.

In total, 4 different boundary conditions have been defined:

1. Inlet: Oxidizer regenerative cooling cycle inlet - massflow defined at 288K
2. Inlet: Fuel Injector - massflow defined at 288K
3. Outlet: nozzle exit, pressure of 0 bar defined
4. Wall: All remaining boundaries (e.g. nozzle, walls, no slip conditions)

The fluid flows are calculated using the K- ϵ turbulence model as it was found to provide good results and a stable solution by other authors[20] [21].

The chemical reaction used by CFX is listed below in equation 4.1. It includes the 8 major reaction products as found using RPA at $P_{Chamber} = 15$ bar.



Eight products were selected as a balance between model accuracy and computational cost. If more than eight come more accurate however the computational time would also be significantly increased. Eight species is considered enough for other N_2O /hydrocarbon reactions used in other simulations [20] and hence is also considered sufficient here.

The eddy dissipation model was selected as the most suitable combustion model. Several authors in the past used the finite rate chemistry to model the combustion inside hybrid motors [22] [23] [24]. In this model, the detailed Arrhenius chemistry equations are used with the local averaged values. This way, the real turbulence-chemistry interaction is not taken into account. In fact, it is not possible to calculate the mean reaction rate directly from the concentration and temperature mean values and, if this is done, large errors could be generated[24]. The eddy dissipation model is a semi-empirical model developed with the hypothesis of fast chemistry. In this case, the reaction rate is controlled by the turbulent mixing of fuel and oxidizer. This model has been widely and successfully applied in the prediction of turbulent non-premixed flames. The reaction rate is proportional to the reactant's molar fraction and to the rate of dissipation of the eddies: the turbulent eddy frequency (the inverse of the large eddy mixing time scale k/ϵ). This model has been used with much success by other authors [20] [21].

A mesh analysis was conducted to find the appropriate mesh size for the given problem. The solver was first run with a course mesh followed by successive finer and finer meshes. The resulting chamber pressures found were then graphed to find at which point the solution was no longer heavily dependent on the mesh size. The mesh size vs solution could then be plotted as in Figure 4.4. It was found that a mesh with 250 000 elements was sufficient as it predicted a pressure within 1.2% of the finest mesh attempted.

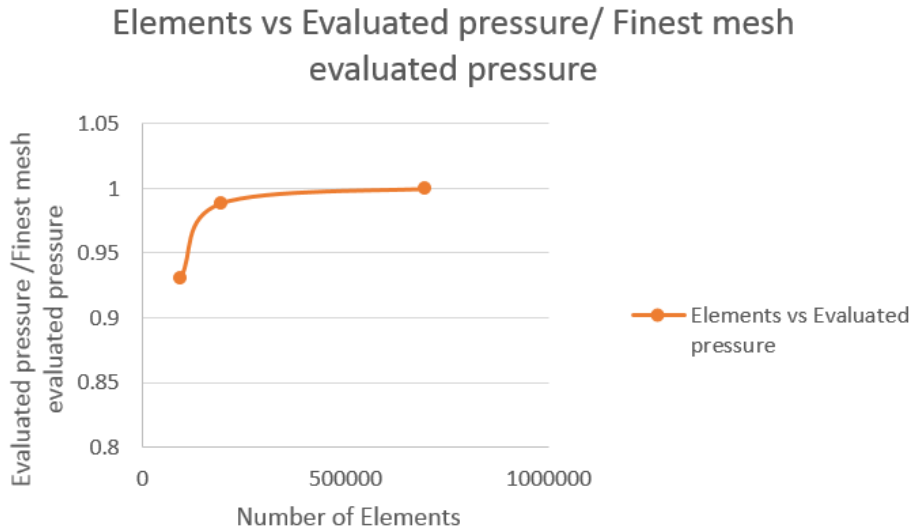


Figure 4.4: Plot of simulation solution vs number of elements used in the simulation.

It is worth noting that the necessary mesh quality depends on the particular problem. Some simulations required far greater than 250 000 elements to achieve a satisfactory mesh on fine elements.

The aim of the model is not only to predict the global motor performance such as C* performance but also to obtain a qualitative understanding of the internal flow structures formed. Hence, it is necessary to refine the mesh next to the combustion chamber walls to accurately resolve fine detail that a specific design may use. With the mesh quality selected, a single iteration would take approximately 1 min on an 4 core Intel I7 processor. A typical simulation would take 24 hours of processor time.

The criteria for convergence for a given simulation were:

- RMS residuals below 10^{-6}
- At least 1000 iterations
- Negligible fluctuation between iterations of key parameters such as nozzle inlet pressure (less than 0.1%)

4.3.2. RESULTS

In order to obtain a qualitative measure of the maximum performance the model could produce, a control model was made which used unlike impingement and a chamber with an L^* of 2.5, 5 times as large as the selected L^* of 0.5. This was sufficient to achieve a homogeneous fluid temperature approximately equal to the expected flame temperature of 3100 k at the nozzle entrance. The mass fraction of unburned N_2O and ethane was less than 0.5% and 0.1% respectively. This control was used to measure the relative combustion efficiency of the proposed injection methods.

The numerical model was first used to assess the effectiveness of various injection methods. To limit the computational cost, only the fluid and combustion models were used. Planes of symmetry were also used to reduce the fluid volume simulated. Limiting the required computational power required allowed the designer to maximise the number of injection methods that could be investigated.

Injection method concepts for gas/gas injectors were studied at length using commonly available literature [9] [25]. From the vast number of injection methods available, several were selected for their applicability to gas/gas injection, ease of manufacture and promise of efficient mixing in a single element. A single element was all that considered possible due to the low mass flows and hence small injection orifices. The methods of injection investigated were the following.

- Unlike impinging
- Vortex

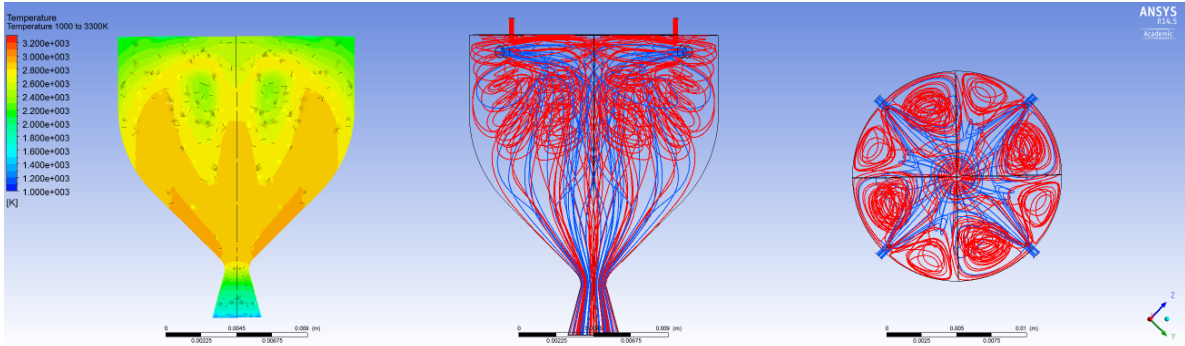


Figure 4.5: Unlike impinging injection temperature profile

Figure 4.6: Unlike impinging injection Streamline (side view)

Figure 4.7: Unlike impinging injection Streamline (top view)

- Swirl (like and unlike rotation)
- Coaxial
- Coaxial swirl

A typical simulation yielded several figures of combustion temperature and flow streamlines. Furthermore, the fraction of unburned N_2O and ethane in later simulations as well as $P_{Chamber}$ at the nozzle entrance was assessed. The results are presented in Table 4.1

Table 4.1: Results summary of injector modelling

Injection type	C* Efficiency [%]
CoAx Swirl ($L^*=2.5$) (control)	100
Like impinging	96
Unlike Swirl (45 deg)	91
CoAx swirl	94
Vortex	N/A (unstable solution)
Unlike impinging + Swirl (45 deg)	98

Although other injector designs such as unlike impinging were found to produce good efficiencies, they would also produce very inhomogeneous temperature profiles in the combustion chamber as only a few elements could be used. They are also known to be very sensitive to production imperfections and require high tolerances.

From these results, it was concluded that a coaxial swirl design would likely produce an efficient injector design. It is also known to work well with gaseous injection with specific design data available [25]. Furthermore, it only requires one injection element to obtain rotationally symmetric propellant distribution. This is not true for many other injection styles such as unlike impinging. Only requiring one injection element means that the injector port can be of larger diameter, reducing machining errors and hence errors in the measurement of C*. This effect is elaborated on in Section 6.9. The selected design can be seen if Figures 4.8 to 4.10. From these figures, it can be seen that there is a significant unused volume in the chamber in the upper corners. No mixing takes place here and hence this volume can be omitted from the design to reduce the chamber inner surface area to decrease the heat flux to the chamber wall. It is also known that an angled head at the top of the motor can reduce combustion instabilities by reflecting pressure waves in a more chaotic manner, avoiding nodes and antinodes developing in the chamber [25].

Seven geometry styles were analysed in an attempt to eliminate unnecessary chamber volume. The parameters varied were:

- Oxidizer injector port diameter (0.5 to 0.75mm)
- L^* (0.2 to 1m)
- Chamfer angle (0, 40 and 50 degrees)
- Chamfer length (4 to 6mm)

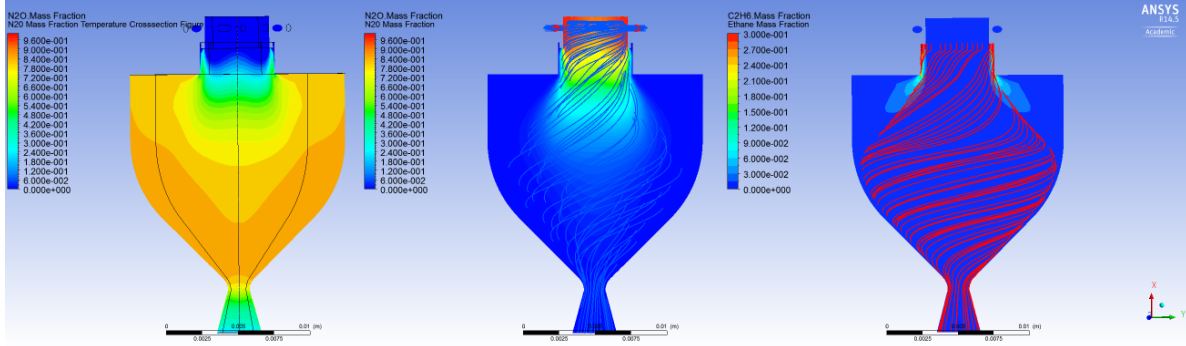


Figure 4.8: CoAx Swirl temperature profile distribution

Figure 4.9: CoAx Swirl oxidizer streamlines and profile

Figure 4.10: CoAx Swirl fuel streamlines and profile

The following combinations were modelled in the order given by Table 4.2. Changes were made to the chamber geometry based on the results of the previous simulation. It was attempted to obtain a design where the streamlines approximately followed the combustion chamber profile, thus making the most use out of the chamber volume available. This required numerous iterations as a change in geometry resulted in a change in the flow path and hence another change in geometry was required to suit the new streamlines.

Table 4.2: Summary of CoAx swirl injector geometry types analysed

Configuration number	$d_{inj\ ox}$ [mm]	L^* [m]	Chamfer angle [deg]	Chamfer length [mm]
CoAxS-0.75-1-0-0	0.75	1	0	0
CoAxS-0.5-1-0-0	0.5	1	0	0
CoAxS-0.5-0.9-4-40	0.5	0.9	4	40
CoAxS-0.5-0.5-4-40	0.5	0.5	4	40
CoAxS-0.5-0.4-6-50	0.5	0.4	6	50
CoAxS-0.5-0.3-5-50	0.5	0.3	5	50
CoAxS-0.5-0.18-4.5-50	0.5	0.18	4.5	50

The first configuration in Table 4.2, CoAxS-0.75-1-0-0, is the output of the injector selection previously discussed where co-axial swirl injection was selected. The first change to be simulated was a reduction in injector diameter from 0.75 to 0.5mm to increase the injection velocity. It was found that this decreased the N_2O fraction at the nozzle throat from 1.8 to 0.3% as shown in Figure 4.11. The injector diameter was not decreased further as it would be difficult to machine. The following five configurations experimented with L^* and the chamber head end chamfer geometry to find a combination of chamfer length and angle which minimised L^* while maintaining a low level of unburned N_2O mass fraction at the nozzle throat.

From Figure 4.11, it was determined that the configuration 'CoAxS-0.5-0.5-4-40' achieved N_2O levels lower than 1% for a relatively low L^* value of 0.5m. This was seen as a good compromise between performance while maintaining a small form factor. It has been found in literature that an L^* of 0.5 corresponds well with other known gas/gas injection motors such as oxygen/Methane [9].

The N_2O fraction at the throat was used as a performance parameter as it provides far greater resolution than $P_{Chamber}$, and hence can provide better insight into when the motor starts to lose performance.

The final selected geometry, CoAxS-0.5-0.5-4-40, is presented in Figures 4.12, 4.13, 4.14 and 4.15. From these figures it can be seen that the flow profile closely follows the chamber wall profile, and hence the chamber volume is used to the fullest. This analysis was the conclusion of the CFD study to determine the injector design.

The next step in design was to model a motor using manufacturable geometry, including the spark plug geometry. This was achieved by developing a computer aided design (CAD) model of the motor alongside the CFD model. In this way, particle designs could be assessed in a qualitative way. The model was also extended to a full 3D model, no longer using rotational symmetry which could not be practically machined. This was

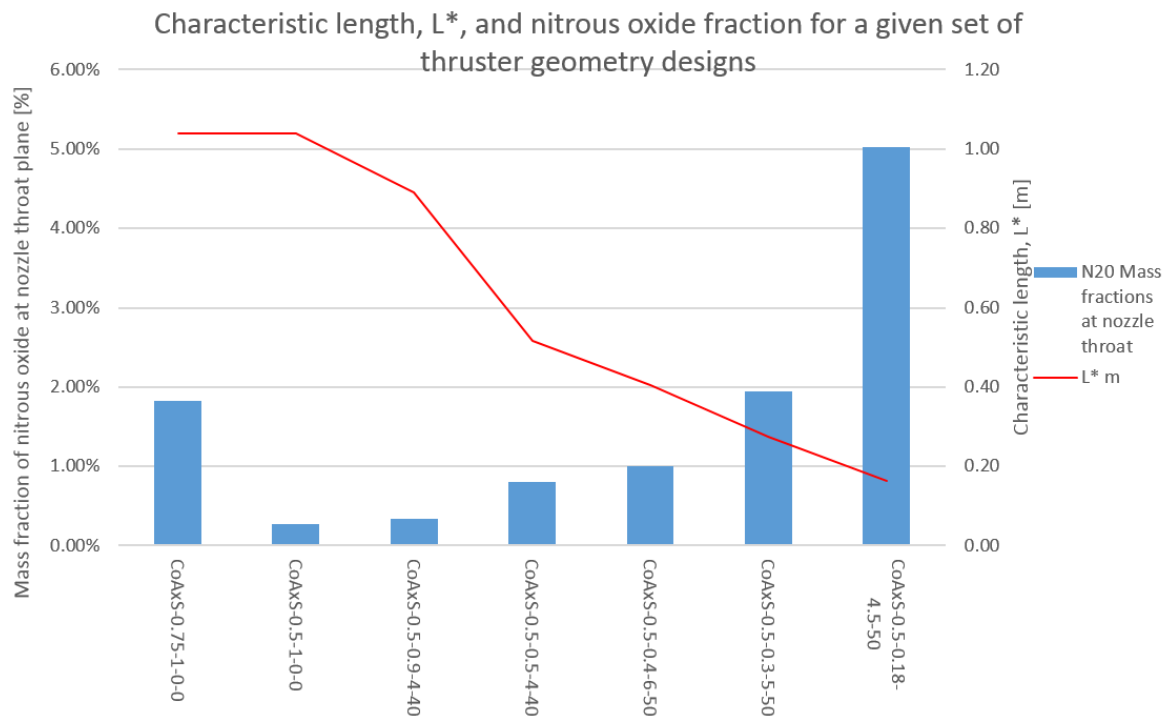
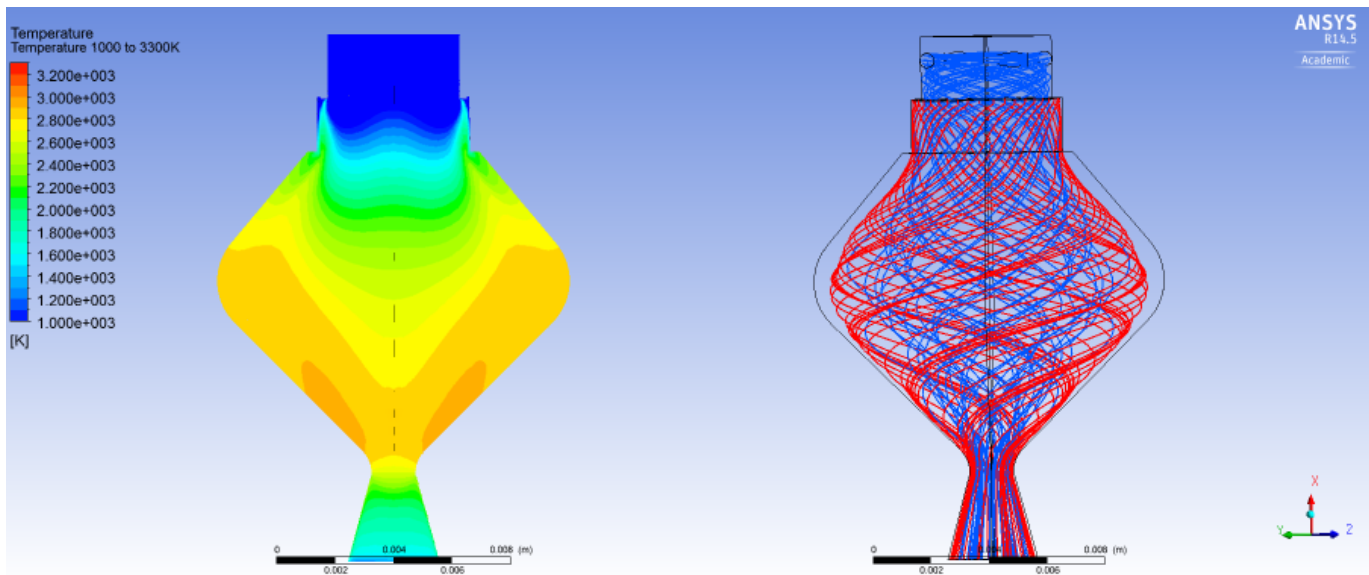
Figure 4.11: L* vs N₂O fraction for various thruster configurations

Figure 4.12: CoAxS-0.5-0.5-4-40 temperature profile distribution

Figure 4.13: CoAxS-0.5-0.5-4-40 streamlines

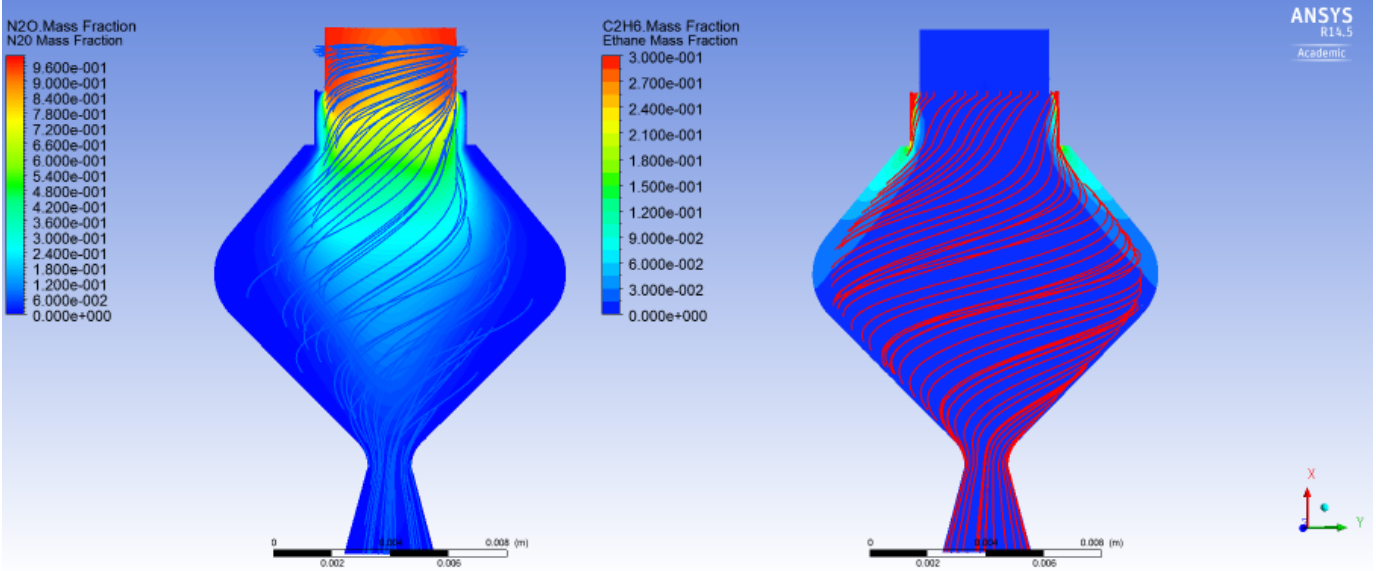


Figure 4.14: CoAxS-0.5-0.5-4-40
oxidizer streamlines and profile

Figure 4.15: CoAxS-0.5-0.5-4-40
fuel streamlines and profile

done to investigate the effects of inhomogeneous mixing caused by poor distribution of reactants within the chamber.

Motor 1 was manufactured and tested without having performed any full multi-physics simulations. This was done as it was considered unwise to invest more time into simulations when it was unknown if the simulations had produced a useful motor configuration or not. Motor 1 was tested and the results are presented in Section 6. The motor was found to have several inadequacies including severe combustion instabilities, an insufficient spark plug design and most of all was found to be very time consuming to construct and impossible to achieve the required tolerances on critical elements such as the fuel injectors. For these reasons, testing was used to verify the design of motor 2 and 3, rather than use the numerical model, until sufficient confidence in the design was obtained. Thus, motors 2 and 3 were not simulated numerically before manufacture. More details on motor 2 and 3 can be found in Section 5.3. After testing of motor 3, a CFD model, including the thermal model and regenerative cooling cycle, was made retroactively. This was done to assess the performance of the cooling cycle such that it could be improved upon. The results for the thermal aspects of the model were found to be accurate enough to yield useful engineering data. Specifically the combustion heating power figures were within $\pm 15\%$ of experimental data.

Motor 4 was designed through several iterations of CFD. It was first found that the regenerative cycle was not extracting heat in an efficient manner, and hence the motor failed. This was solved by decreasing the cooling channel area and changing the cooling channels from a series of parallel machined slots as is common on larger motors, to a screw slot. This had the effect of increasing the flow velocity of the cooling fluid, and hence also the pressure drop over the cycle. The CFD results for the final simulation which was then manufactured into Motor 4 and used in the HypT12 test series, is presented in Section 6. Further discussion of this particular simulation in comparison to the experimental test data can be found in Section 7.6.2.

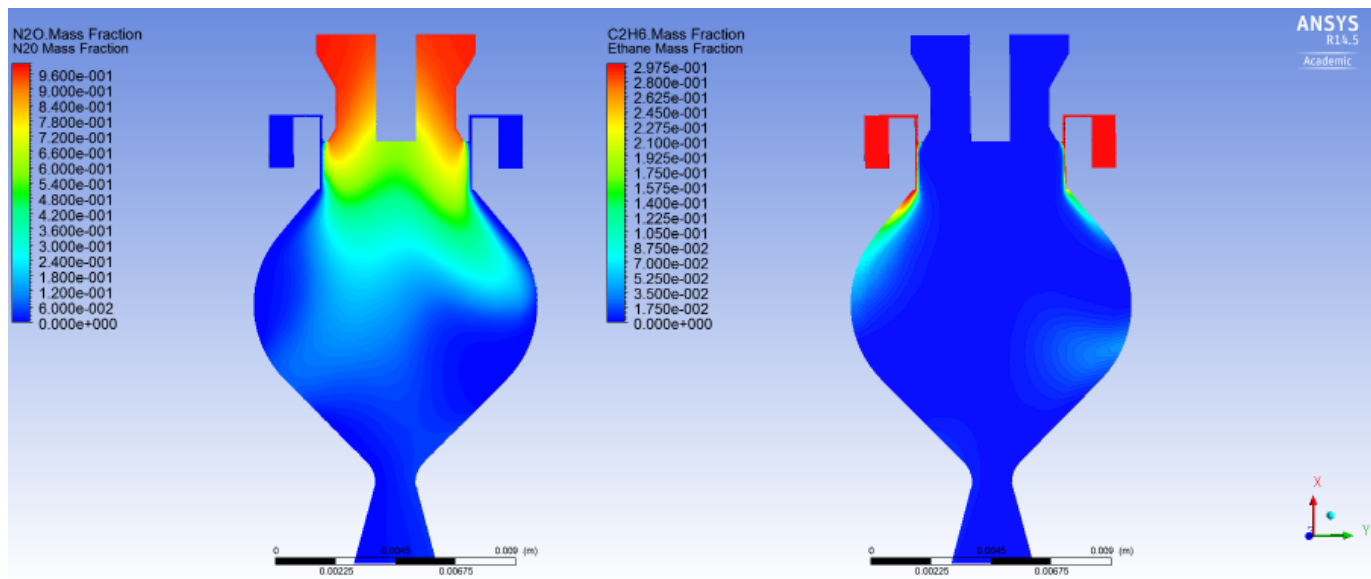
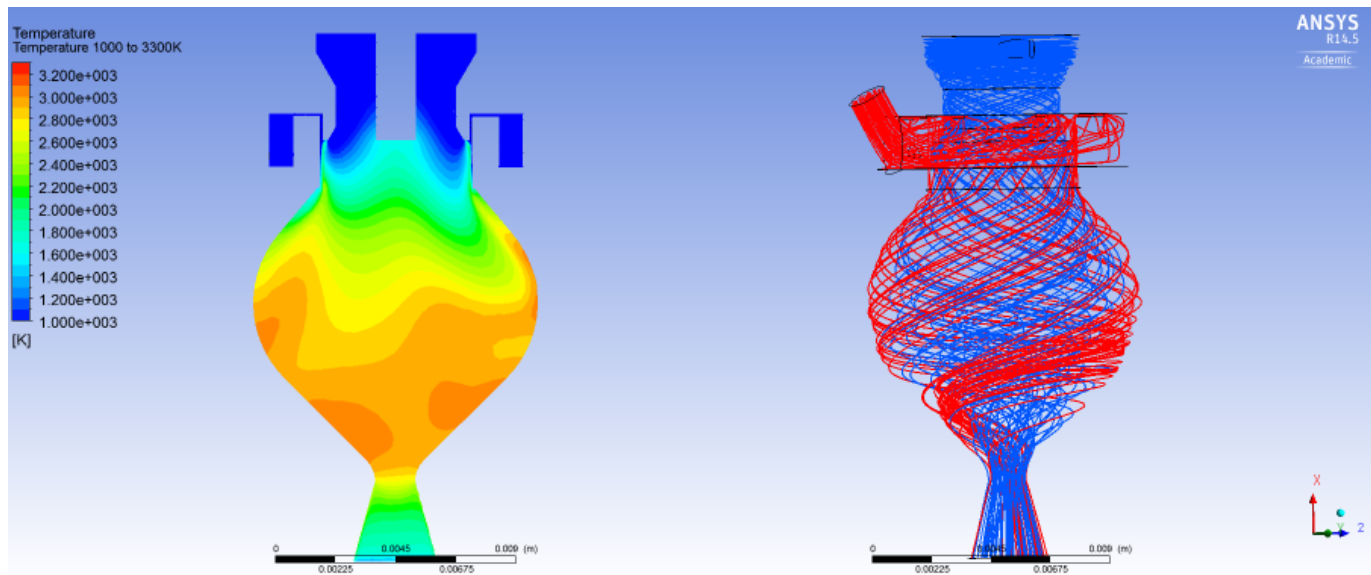


Figure 4.18: Motor 1 oxidizer profile

Figure 4.19: Motor 1 fuel profile

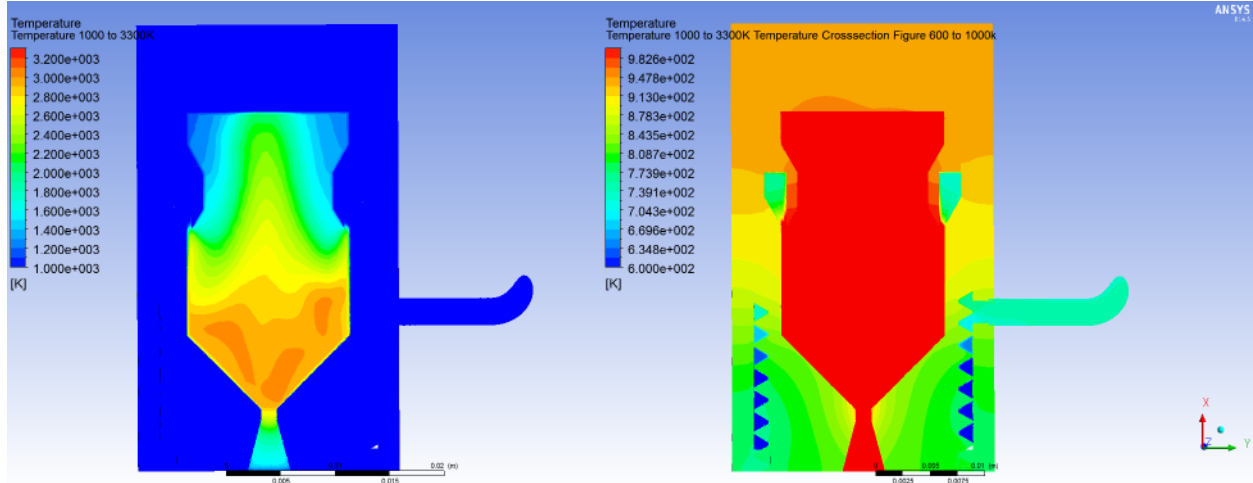


Figure 4.20: Motor 4 fluid temperature profile (1000-3300K)

Figure 4.21: Motor 4 fluid temperature profile (600-1000K)

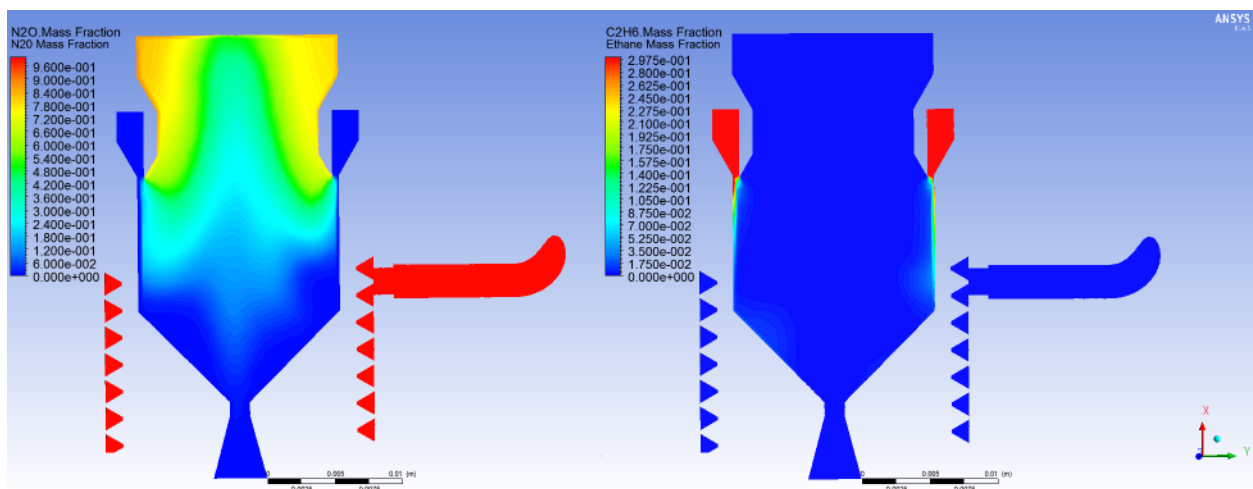


Figure 4.22: Motor 4 oxidizer profile

Figure 4.23: Motor 4 fuel profile

5

EXPERIMENTAL SETUP

This section will detail the experimental setup used to test motors 1-4 as well as the motor designs themselves.

5.1. TEST BENCH

The test bench used consisted of a feedsystem, sensor system, data acquisition system ([DAQ](#)), motor, spark generator, gas supply and a remote command post. These parts will be explained below along with the operational concept and other practicalities of testing.

5.1.1. FEEDSYSTEM LAYOUT

The feedsystem is the component which supplies the motor with both gaseous N_2O and C_2H_6 . A diagram of the system can be seen in Figure 5.2. The system is built specifically for the hot fire tests of this thesis. The feedsystem consists of two functionally identical branches for fuel and oxidizer are laid out side by side. Each branch features a fill valve (FV), which connects to an industrial gas cylinder of nitrous oxide or ethane. The fluid from the industrial gas cylinder enters a run tank, which can be filled by venting vapour from the top of the run tank via the bleed valve (BV). At the tank outlet, temperature and pressure of the fluid are logged.

During a hot fire test, fluid travels from the run tanks through a filter of $15\mu m$ size and through the main valve (MV), which is actuated by a solenoid.

Downstream of the main valve the pressure and temperature are sensed, after which an exchangeable orifice chokes the flow, resulting in a relatively constant mass flow. The pressure and temperature are once again measured downstream of the orifice. The oxidizer is then fed to the motor where it enters a regenerative cooling cycle. At the exit of this cycle, a pressure and temperature measurement is made once again before it is injected into the combustion chamber. Downstream of the choking orifice, the fuel is directly injected into the combustion chamber.

The location of all pressure and temperature sensors are denoted by the letter 'p' or 'T' located along the feedsystem in Figure 5.2. The diagram also shows the motor with a regenerative cooling cycle. Motor 2 did not feature a regenerative cooling cycle and hence these sensors were omitted for the associated tests.

As mentioned, the feedsystem consists of two flow chokes which are designed to provide the motor with a constant mass flow of gaseous propellants. Although the propellants are stored in the liquid phase, downstream of the orifice the liquids have been brought very far away from their saturated state and given significant time to evaporate any liquid, hence it can be assumed that all fluids at the motor are gaseous. Two gaseous injectors located on the motor (not depicted in Figure 5.2) provide sufficient pressure drop such that the motor combustion pressure is sufficiently isolated from the feedsystem processes.

The feedsystem was constructed largely of 6mm Hamlet process swage style fittings. The tanks were an in-house developed design, constructed of aluminium. The motor was connected to the feedsystem via nylon flex lines, to allow for some variation in motor design and position. Note that the volume between the main valves and the chamber is far larger than what would be the case on a flight system and is approximately equal for oxidizer and fuel. An attempt was made to reduce this volume significantly in HypT12 where the main valves and orifices were mounted directly onto the motor.

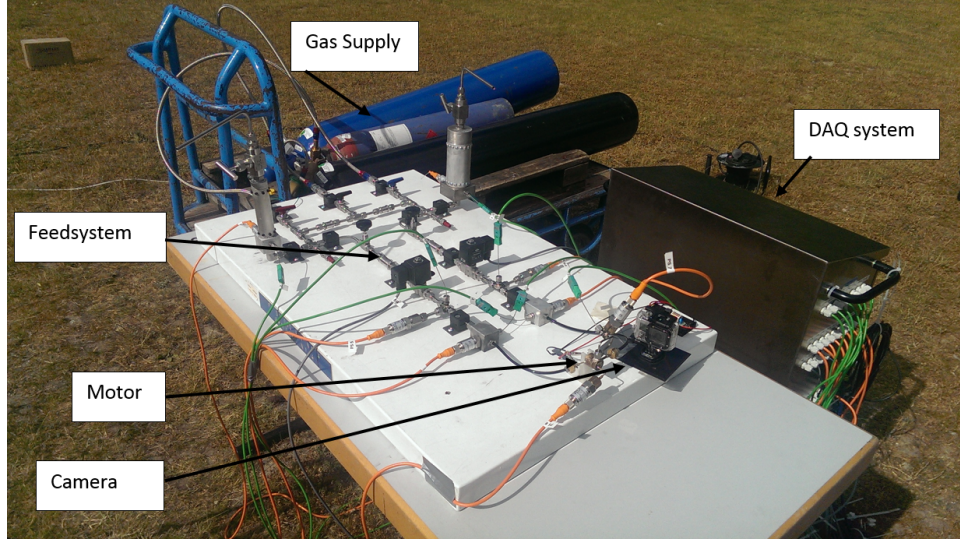


Figure 5.1: The test bench as setup for a hotfire test

The feedsystem was designed during the thesis of T. Knop. For more details on the feedsystem, please refer to T. Knop[26].

5.1.2. MEASUREMENT AND CONTROL SYSTEM

The measurement and control system was used to conduct tests with the goal of experimentally determining the following parameters:

- combustion efficiency (C^*)
- $P_{Chamber}$
- Startup and shutdown transients
- maximum achievable burn time
- restart-ability
- Combustion stability
- Total impulse
- Impulse repeatability
- Effectiveness of the regenerative cooling cycle

The measurement and control system used is based on a National Instruments Compact Rio. It is capable of providing the following services:

- digital output x16 channels
- 4-20 mA pressure sensor inputs sampled at 2kHz x8 channels
- 0-5v load cell inputs, sampled at 2kHz x4 channels
- K type thermocouple inputs, sampled at 20 Hz x16 channels

The test bench could be controlled via an Ethernet cable. This was typically done from 40m away in order to be a safe distance from the hotfire tests.

The DAQ system was controlled via a Labview GUI which featured all sensor outputs such that the motor performance could be monitored during a test. The GUI allowed for both manual and automated control of the motor in order for tests to be conducted consistently if desired. The GUI can be seen in Figure 5.4.

The measurement and control system was developed at DARE to serve as a general DAQ and control system for any testing DARE was required to conduct.

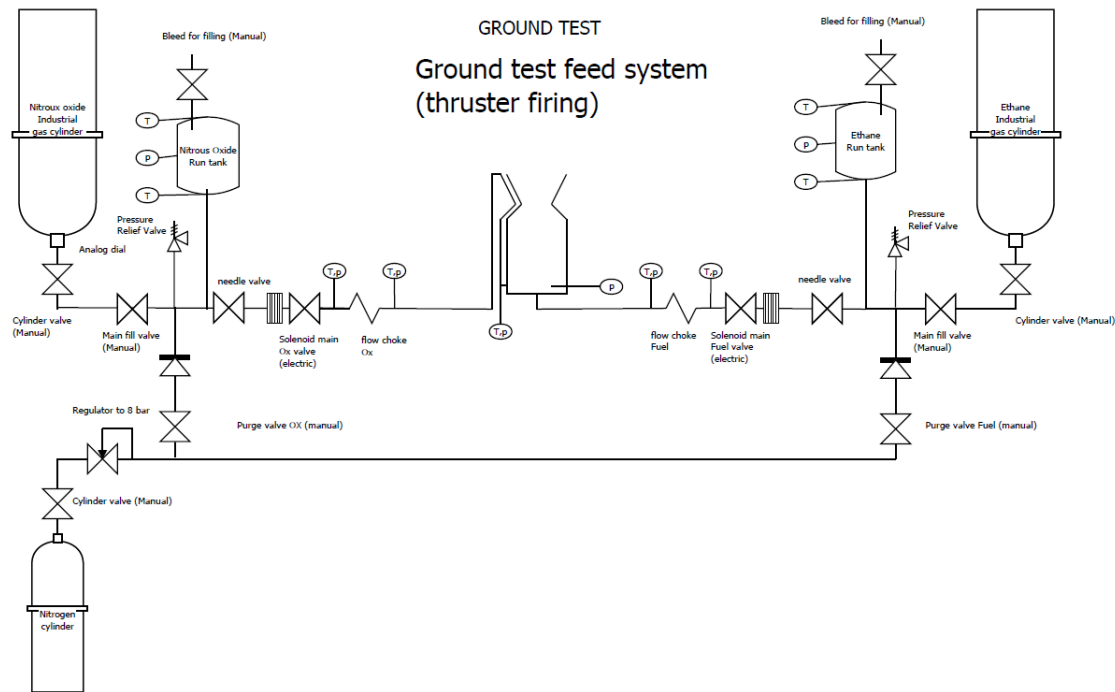


Figure 5.2: Feedsystem schematic layout



Figure 5.3: DAQ system used for control and data acquisition during testing

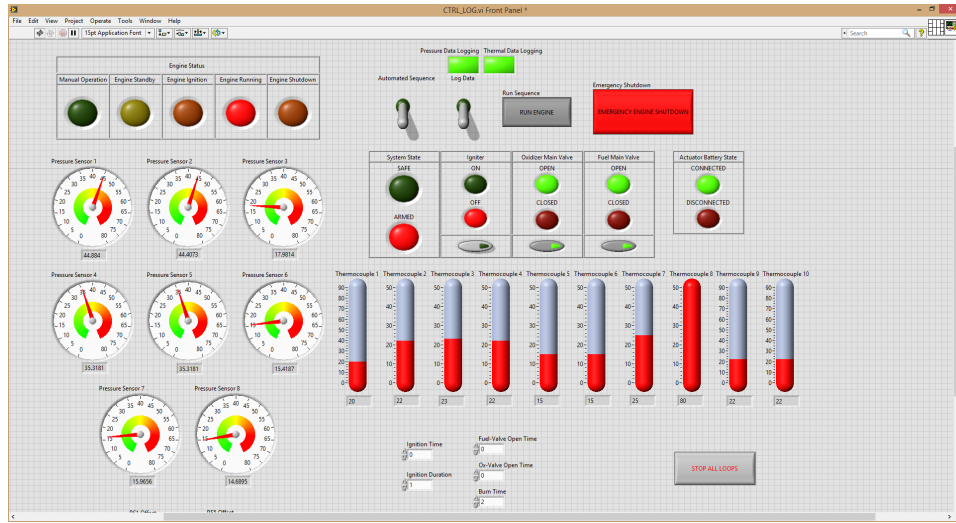


Figure 5.4: LabView GUI used to control the test bench

Number	Designation	Range	Min accuracy [bar]
1	Tank_ox	70 bar abs.	0.175
2	USori_ox	70 bar abs.	0.175
3	DSori_ox	35 bar abs.	0.0875
4	Tank_fuel	70 bar abs.	0.175
5	USori_fuel	70 bar abs.	0.175
6	DSori_fuel	35 bar abs.	0.0875
7	Regen line	20 bar abs.	0.05
8	Combustion chamber ¹	20 bar abs.	0.1

Table 5.1: The eight pressure transmitters of type 'Keller PAA-23SY/XXbar/81549.77' with 4-20 mA output along with their range and location in the test setup.

5.1.3. PRESSURE SENSORS

The system is equipped with eight piezoresistive pressure transmitters of type 'Keller PAA-23SY/XXbar/81549.77' with 4-20 mA output and a range from 0 to 20, 35 and 70 bar abs. See Appendix B for a full data sheet.

5.1.4. THERMOCOUPLES

The thermocouples used are 'K type' thermocouples. For fluid measurements, these are located in the tip of a probe. The probe can be inserted into a feedsystem part and secured using a compression fitting. For surface temperature measurements, bare thermocouples were secured to the test article using aluminium tape. This proved effective at low temperatures however very ineffective above 450°C when the aluminium tape caught fire and lost its adhesion. The thermocouples are quoted as having an accuracy of $\pm 1.5^\circ\text{C}$ for a temperature range of -40 to 375°C. From 375 to 1000°C, the accuracy is $\pm 0.4\%$ of the measured temperature in °C. See Appendix C for a full data sheet.

5.2. OPERATIONS

Tests were conducted on the 'architecture field', located at Van Den Broekweg, Delft in the months of June through to September 2015. Testing was conducted in mostly sunny weather. Ambient temperatures were typically between 20 and 30 degrees C with medium humidity. Testing could not be conducted in the rain due to the systems sensitivity to water, particularly in the feedsystem where water can lead to freezing of the choking orifice. On one occasion (HypT12-07) testing was conducted late in the evening when temperatures rose and humidity increased sharply, resulting in a short circuit of the spark plug. Testing was halted and continued the next day due to this effect.

Parameter	Motor 1	Motor 2	Motor 3	Motor 4
Diameter(internal) [mm]	10.6	15.7	15.7	15
Diameter(external) [mm]	22	24	24	24
length (internal) [mm]	17.5	54	54	27.2
length (external) [mm]	25	67.8	67.6	40.8
Characteristic length (L*) [m]	0.35	4.1	4.1	1.3
A _{ox} injector [mm ²]	.38	1.33	.79	.79
A _{fuel} injector [mm ²]	.14 ²	.13	0.07	0.07
A _{throat} [mm ²]	1.76	1.76	1.76	1.76
Regenerative Cooling	Yes	No	Yes	Yes
Igniter	Tungsten electrode	Rimfire Z3 plug	Rimfire Z3 plug	Rimfire Z3 plug

Table 5.2: Motor parameters for motors 1 to 4

A typical test day would involve wheeling out the test bench from the DARE workshop to the test field located 500m away. Setup and system checkout would take approximately 1 hour. Propellant filling could be completed manually within 10 minutes. Testing would then commence, with an individual test taking between 5 and 10 minutes. Depending on the occurrences of the test, a new test could be performed 10 minutes after the previous test, depending on whether the propellant tanks needed to be refilled or not. It was possible to conduct 20 burns in a single day with a team of two. Two people were required for testing; one to conduct operations and the other to perform a checklist and safety role. The operating procedures follow DARE standard practice for N_2O and have been approved by the DARE safety board.

5.3. MOTOR DESCRIPTIONS

The motors described in this section were manufactured and tested using the before-mentioned test setup. The motors were designed using the method and models described in Section 4. The system is intended for use in space, hence it would be appropriate for the motor to feature a high expansion ratio nozzle as is commonly used in space applications. These are however difficult to manufacture and can induce flow separation in the nozzle unless fired in a vacuum chamber which was not available for these tests. For these reasons, the motors tested use an expansion ratio of 7. In fact, as thrust was not measured, the expansion ratio was not closely controlled as it has no effect on the measured C* efficiency.

Each motor used in the experimental setup was significantly different to its predecessor, and hence also performed in a very different manner. Table 5.2 displays the motors and their major parameters. Note that the internal length is defined as the distance from the nozzle throat plane to the top of the injector fluid volume.

5.3.1. MOTOR 1

Motor 1 is the first and physically smallest motor of the group. It was designed largely using the numerical analysis methods presented in Section 4. The motor consists of four major components; the injector, the chamber upper and lower, and the jacket. The chamber upper and lower are silver soldered together to make a single component. The parts are turned from brass and fastened together with four M2 screws. The internal seals are formed using nitrile O-rings. The regenerative cooling cycle was connected to the oxidizer injector via 3mm compression fittings. Oxidizer and fuel inlets as well as pressure sensor ports were silver soldered to the individual parts as required. The motor could be disassembled and inspected between firings. It would be pressure tested before each test to ensure correct assembly and that the single o-ring seals were functioning correctly. A schematic of motor 1 can be seen in Figure 5.5 where it can be seen that the electrode is press fit in from the outside. The electrode insulation was originally intended to be ceramic however this was found to be too difficult to press fit so a plastic was used. As expected, this plastic would deform and had to be regularly replaced. The plastic insulation also had a tendency to allow the electrode to move as the press fit wore out.

Motor 1 presented several major machining challenges. The fuel injector ports in particular were difficult to machine as the only tools available were poorly suited to fine details where tolerances of 0.01mm or greater were required. It was later found that parts with such high tolerance requirements were poorly suited to silver

²The fuel injector ports were not able to be produced accurately, hence it is likely the actual area is significantly larger

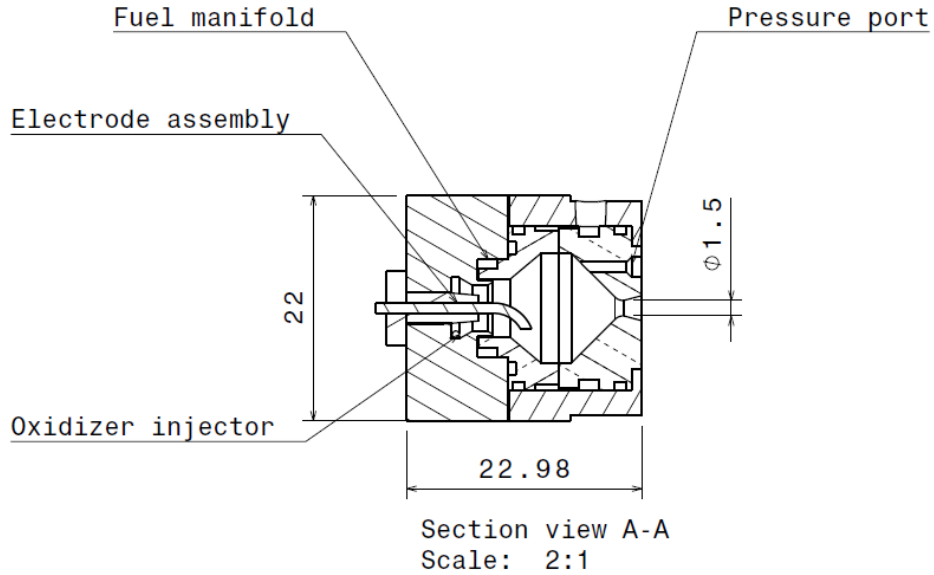


Figure 5.5: Motor 1 section view displaying major features

soldering as the parts would become soft and warp during production. Damage to the fuel injector of motor 1 can be seen under a microscope as shown in Figure 5.7.

5.3.2. MOTOR 2

Motor 2 was made to correct the design issues encountered in motor 1. Motor 1 was complex in design, making it time consuming to manufacture. This lead to a long iteration cycle. The spark plug design was also found to be very deficient. For these reasons, motor 2 was designed to be much simpler to manufacture. The electrode design of motor 1 was replaced with a commercially produced spark plug and the regenerative cooling cycle was omitted. As an additional measure to ensure good combustion, the design L^* was increased from 0.35 to 4.1. The chamber was made to have significant thickness at the nozzle in particular to provide capacitive cooling such that reasonable burn times could be achieved despite the lack of regenerative cooling. The oxidizer injector area was also increased, as it was feared that high injection velocities were leading to unstable combustion as suggested by literature [25]. The fuel injector area was kept constant as this was not effectively evaluated in the testing of motor 1.

Motor 2 was constructed of two major parts; the oxidizer injector and the chamber which included the fuel injector. These two parts were soldered together to form a single piece chamber. The propellant inlets and pressure port were then attached with silver solder. A cross-section of the motor can be seen in Figure 5.8.

The primary purpose of motor 2 was to show that the test setup functioned as intended and that all basic elements to fire a liquid engine were indeed present. Hence, it was not seen as important that the motor was optimized such that it would achieve the original design requirements.

5.3.3. MOTOR 3

Motor 3 was built according to similar design principles as motor 2. The internal geometry of motor 3 was identical to motor 2. A regenerative cooling cycle was added to provide additional cooling. The injector area was adjusted as per Table 5.2 to reduce the feedsystem-coupled instabilities observed in the HypT9 test series. No numerical analysis tools were used in the design of the regeneratively cooled cycle due to time constraints. Also, at this stage it was unknown if N_2O was suitable to use as a coolant due to its monopropellant and oxidizing properties. The L^* was also kept constant as to motor 2 although it was known that this value was far higher than required for good combustion. It was also known that this would lead to far higher heating than the coolant could cope with. Hence, the motor was a 'proof of concept' for a regenerative cooling cycle using N_2O and there was little reason to spend time designing the cycle to obtain maximum cooling performance.

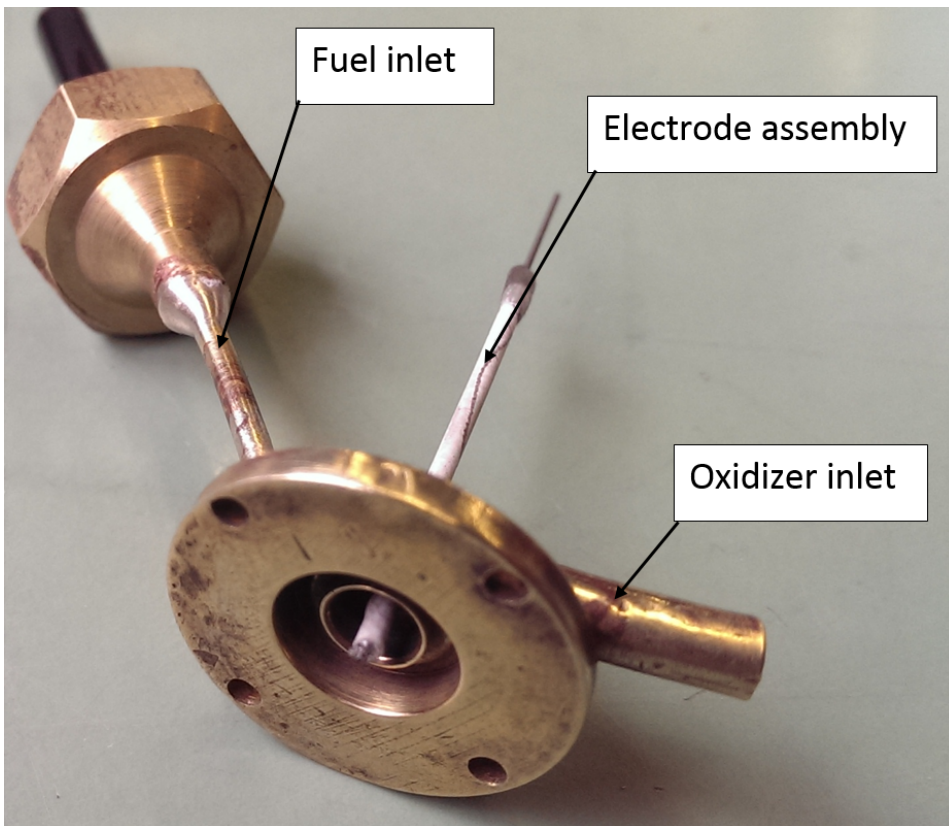


Figure 5.6: Motor 1 oxidizer injector and electrode assembly



Figure 5.7: Motor 1 fuel injector slots showing inconsistency in manufacture. Fuel slots are 0.13mm deep

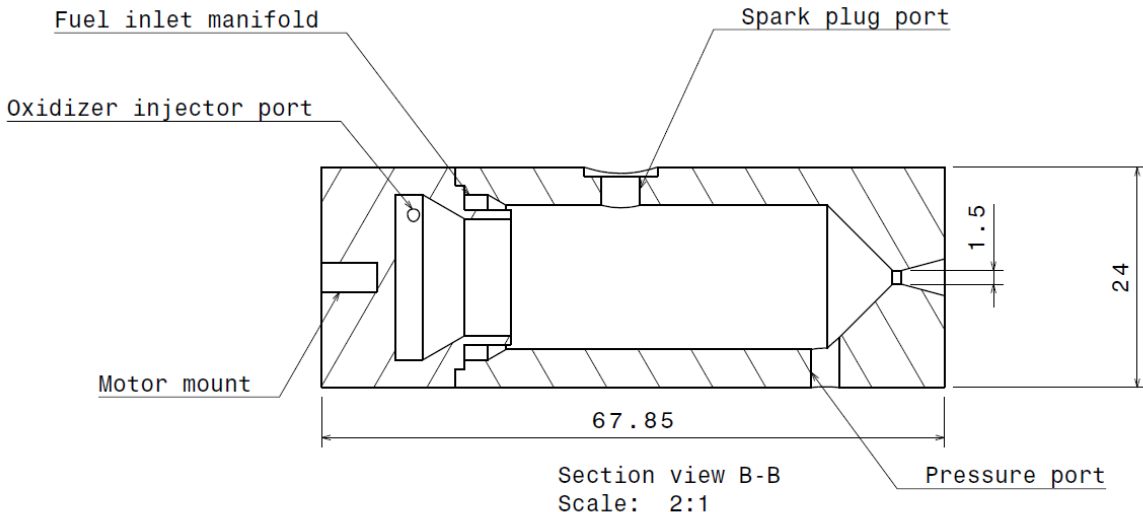


Figure 5.8: Motor 2 section view displaying major features

Motor 3 was constructed of three elements; the oxidizer injector, the chamber inner wall which included the fuel injector, and the cooling jacket. All pieces were turned and milled out of brass and silver soldered together to form a single piece. As with motors 1 and 2, the inlet ports were soldered on to complete the motor.

5.3.4. MOTOR 4

Motor 3 showed that a design using regenerative cooling would indeed achieve longer burn times than without. Hence, motor 4 was designed to use this technology. Motor 4 was designed using the full multiphysical simulation tool presented in Section 4.3. Motor 4 was intended to use the basic design of motor 3, but with a more optimized and well understood thermal design. To reduce the total heat flux into the coolant, L^* was reduced by more than a factor of 3 from 4.1 to 1.3. The injector parameters were kept constant with motor 3.

The motor was constructed from three major components; the oxidizer injector, the chamber which also included the fuel injector, and the cooling jacket. The regenerative cooling cycle used was formed by a screw thread cut into the outside of the chamber wall. The jacket was then heated and press fit over top of the chamber to form the cooling channels. All components, aside from the spark plug, were silver soldered together to form a single piece. The outlet of the regenerative cooling cycle was routed to the oxidizer inlet via a 3mm stainless pipe which was also soldered into place. The layout of motor 4 can be seen in Figure 5.10.

5.3.5. SPARK IGNITER

Motor 1 used an in-house designed 0.5mm tungsten electrode to create a spark igniter with ceramic and later polyoxymethylene (POM) insulation. This design was chosen as it has a significantly smaller form factor than what was possible with commercial off-the-shelf spark plugs. The electrode design can be seen in Figure 5.5 and 5.6 where it is mounted in motor 1.

Motors 2, 3 and 4 used a Rimfire Z3 commercial off the shelf (COTS) spark plug which is commonly used in model internal combustion engines. It was used primarily because of its small form factor. See Figure 5.11. It was first used in HypT9-2. In this test, it was found that the spark plug hook which defines the spark gap had melted off during testing, causing the spark plug to short circuit. This hook was deliberately removed from all subsequent spark plugs, resulting in a larger spark than the designer intended.

The spark was generated using a coil. For motor 1 and 2, the coil drew 6 watts of power. The frequency of the spark would depend on the spark gap distance and the dielectric strength of the fluid which changes as $P_{Chamber}$ changes, hence the energy per spark also varied. The power was reduced to 2 watts on motors 3 and 4 and a much slower oscillating circuit was used to reduce acemi with the measurement system but to maintain a high energy per spark.

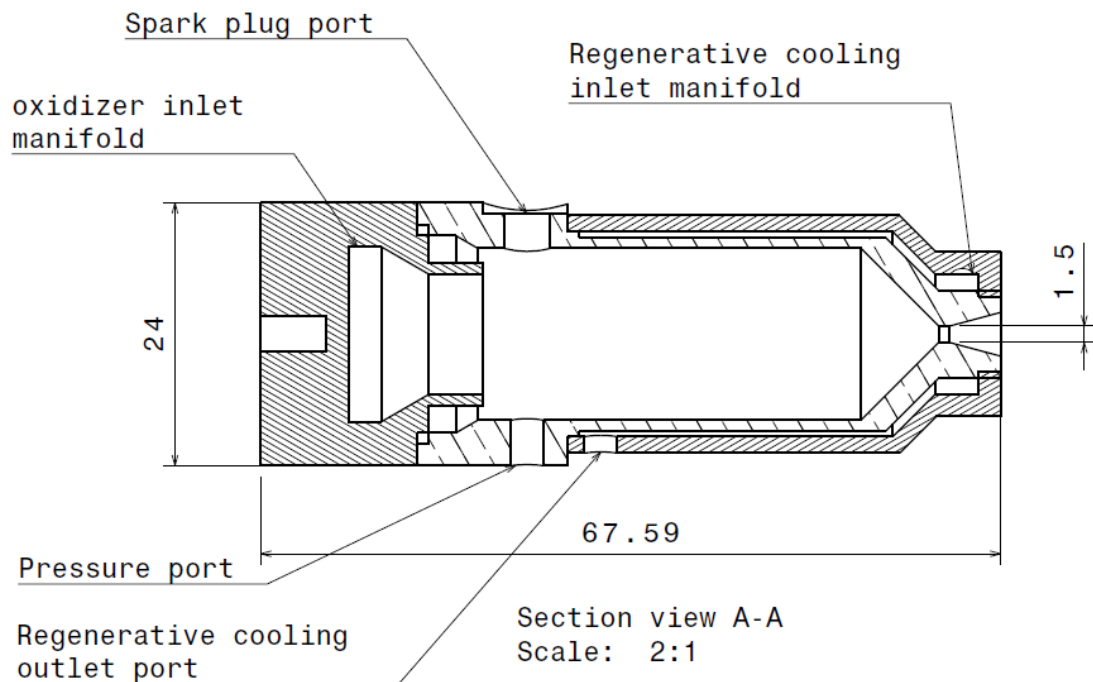


Figure 5.9: Motor 3 section view displaying major features

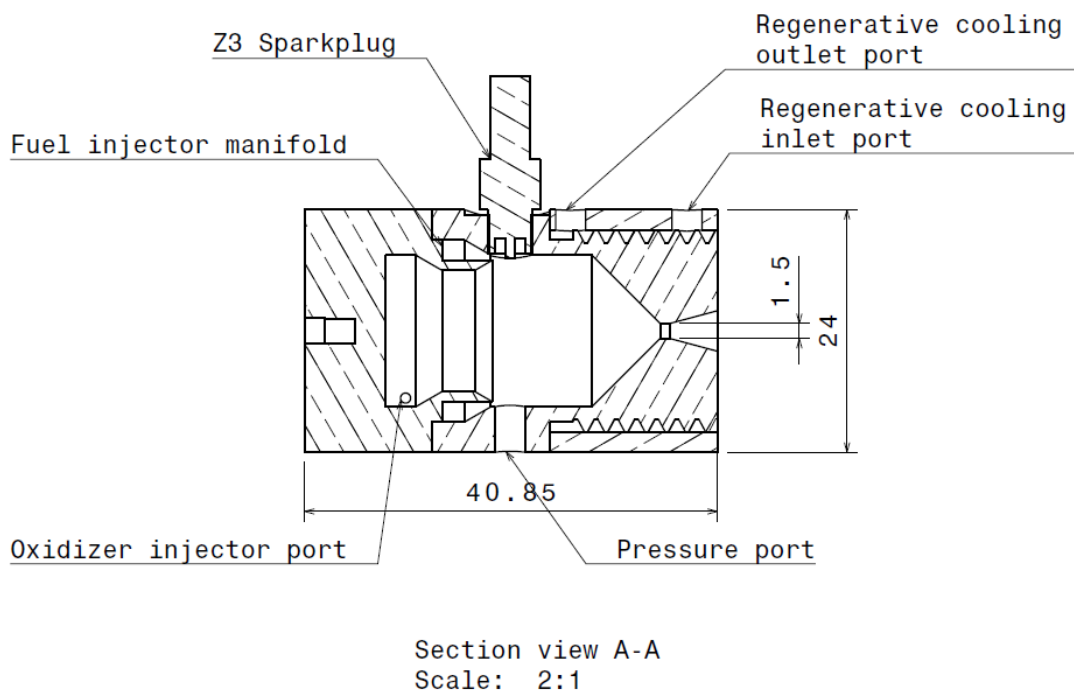


Figure 5.10: Motor 4 section view displaying major features



MICRO VIPER Z3
6MM HEX
10-40 THRD

Figure 5.11: Rimfire Z3 spark plug (dimensions in inches)[27]

6

EXPERIMENTAL RESULTS

One of the core goals of this thesis work was to increase the TRL of small satellite bi-propellant propulsion technology. To achieve this goal, experimentation was conducted to evaluate the performance of the thruster design as well as investigate other operational parameters often overlooked in theory, such as ease of operations and general user robustness in an unclean and variable environment. This section will present the results of the test series conducted.

The design phase of this thesis concluded with the design of Motor 1. See Section 5.3 for details of the motor design. Motor 1 was tested in a series of three tests; HypT 6, 7 and 8 during which 8, 10 and 10 burns were attempted respectively. Only on HypT 7-10 was combustion achieved. Hence these tests are largely omitted from this thesis discussion except where the failure of this motor is interesting in the analysis of combustion instabilities of later motors.

Motors 2, 3 and 4 were tested in test series HypT9, 10 and 12 with varying degrees of success. More than 40 burns were conducted with a total accumulated burn time of 3.5 min, resulting in a substantial data set. For this reason, only a subset of data will be presented here and discussed in Section 7.

Motor burns are specified by a code. An example is HypT12-17-5. HypT stands for Hyperion Test. The first number stands for the test series. The second number stands for the test number of the series. Some tests include multiple burns. For these tests, a third number is specified to refer to a particular burn of that test. HypT12-17-5 thus specifies the 5th burn of the 17th test during the 12th test series.

Tables 6.1 and 6.2 display all hot fire tests conducted.

Table 6.1: Test summary

Test Series and motor configuration	Test Number	Burn Time (s)	Notes
HypT6, Motor 1	10	1	
	8	No ignition	3 attempts
	9	No ignition	2s fuel lead, electrode failure. Testing discontinued
HypT7, Motor 1	1	No ignition	
	2	No ignition	
	3	No ignition	
	4	No ignition	
	5	No ignition	
	6	No ignition	Ignition external to combustion chamber
	7	No ignition	
	8	No ignition	
	9	No ignition	
	10	1	Melted chamber mount
HypT8, Motor 1	1	Popping ignition	
	2	3	DAQ error, run repeated but no ignition
	3	No ignition	Deeper electrode position
	4	No ignition	Shallower electrode position
	5	No ignition	Shallower electrode position. Popping ignition
	6	No ignition	Popping ignition at start of burn
	7	No ignition	Repaired electrode insulation with epoxy
	8	No ignition	C_2H_6 orifice found to be blocked. Replaced with new orifice.
	9	No ignition	Ignition external to motor.
	10	No ignition	N_2O and C_2H_6 pulsed alternatively. Lots of popping. No stable combustion
HypT9, Motor 2	1	Cold flow	
	2	3, no ignition	2 attempts, first with igniter at 2.2V (success), second at 3.2V (no ignition)
	3	3	Refurbished spark plug. Repeat of test 2 at 2.2V. Success
	4	6	N_2O and C_2H_6 refill. Performed after engine cool down
	5	4	Igniter off at T+1s
	6	15	N_2O and C_2H_6 refill
HypT10, Motor 3	1	Cold flow	
	2	3	
	3	3	Refurbished spark plug
	4	3	Repeat of test 3
	5	3	Small igniter coil used
	6	6	N_2O and C_2H_6 refill. Suspected blockage during burn
	7	6	Repeat of test 6. testing for C_2H_6 blockage
	8	6	Repeat of test 7
	9	6x2s	2s burn x 15 (15s pause in between burns) abort at burn 6 due to suspected motor failure. "Motor looks fine"
	10	5x2s	Continuation of test 9. Definite failure of the motor. Suspected at chamber wall

Table 6.2: Test summary (continued)

Test Series and motor configuration	Test Number	Burn Time (s)	Notes
HypT12, Motor 4	1	Cold flow	
	2	No ignition	10s purge
	3	3	Fuel lead 0.2s
	4	No ignition	Pressure sensor P7 replaced with P5 (20 bar vs 70 bar). N_2O and C_2H_6 refill
	5	No ignition	Fuel purged
	6	No ignition	1s fuel lead. Igniter seen short circuiting outside motor
	7	3	Replaced fuel orifice 114 with 122. Testing discontinued due to low light and high humidity
	8	No ignition	New test Day. 2 attempts. Fuel lead 0.5s and 1s
	9	6	3s purge of propellants
	10	No ignition	Repetition of test 9
	11	8	Refill N_2O and C_2H_6 . Repetition of test 9 (No ignition), Manual control achieves ignition
	12	12	C_2H_6 and N_2O purged. Manual control achieves ignition
	13	3	Return to automated control
	14	13s, 4x3s	Manual control mode to preheat motor followed by automated control
	15	3x5s	Manual control mode to preheat motor. Lost data. Test repeated
	16	30	Manual control
	17	3x6s	Fuel line reversed

6.1. HYPT6, 7 AND 8

HypT6, 7 and 8 were conducted with motor 1. A total of 28 burns were attempted during these three test series. All tests in HypT6 resulted in only cold flow. It was suspected that the ignition energy was too low and hence was increased from 2 to 8 watts in HypT7. This resulted in a much more substantial spark. The higher power spark generator resulted in the electrode insulation breaking down in ambient operation. The insulation had to be replaced with thicker insulation to prevent this from occurring.

It was found in HypT7-5 that a faulty check valve in the common N_2 purge line of the feedsystem was allowing oxidizer to flow in the fuel lines, hence no fuel was fed to the motor up until that point. The check valves were omitted from the feedsystem and the oxidizer and fuel lines were re-assembled to omit the common N_2 purge line. Several tests after HypT7-5 resulted in a distinct 'popping' sound but no stable ignition. Only in HypT7-10 was it found that sustained but unstable combustion was achieved. Figures 6.1 and 6.2 display the pressure and temperature measurements of test HypT7-10. The major observations are listed below.

- 37s: Spark igniter starts
- 39s: Oxidizer flow starts
- 40s: Fuel flow starts
- 42s: Temperature in regen starts to increase. 'Popping' sound audible
- 45s: Chamber pressure rises significantly above cold flow levels and temperature sensor system fails
- 46s: Chamber pressure drops significantly. Igniter housing and electrode is ejected from chamber assembly
- 50s: all valves closed
- 52s: Spark igniter stopped. End of test.

The setup was visually inspected after the test. It was found that the plastic motor mount was distorted due to heat. The igniter electrode which was previously mounted inside the motor was found on the table of the test bench, outside the motor. Unfortunately, no video of the test was made due to a failure of the camera battery. No damage, other than to the spark electrode, was observed.

From Figure 6.3 it can be observed that a strong instability develops between 100 and 150Hz from 43 to 45s. This corresponds to the time where heating was observed in the regenerative cooling cycle as observed in Figure 6.2.

The pressure differential between the fuel inlet and chamber was found to be lower than what was measurable. The electrode design was found to not provide adequate sealing and was prone to slipping inside the motor. This led to inconsistent electrode tip position.

In HypT8, the electrode insulation was made thicker and of a more resistant polymer material. The designer was aware that this material would not withstand combustion temperatures however it would serve the purpose of verifying that the electrode insulation was indeed the reason the motor was not igniting. Many tests in this series resulted in ignition, however no sustainable combustion was achieved.

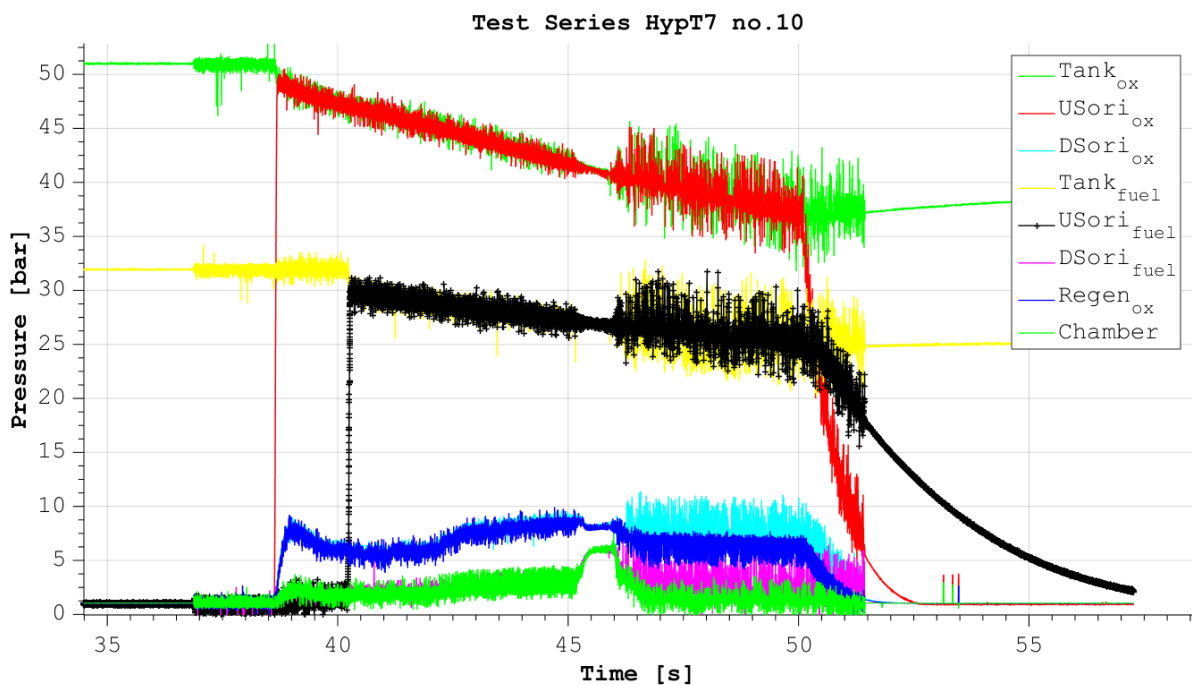


Figure 6.1: Pressure data of HypT7-10

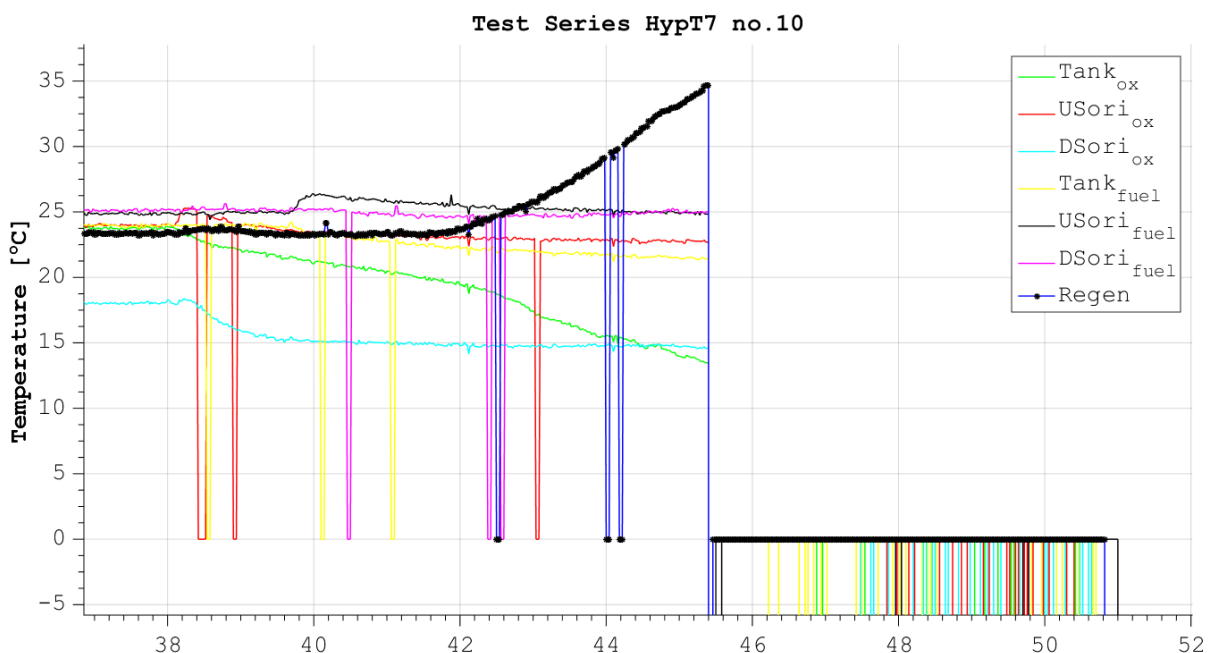


Figure 6.2: Temperature data of HypT7-10

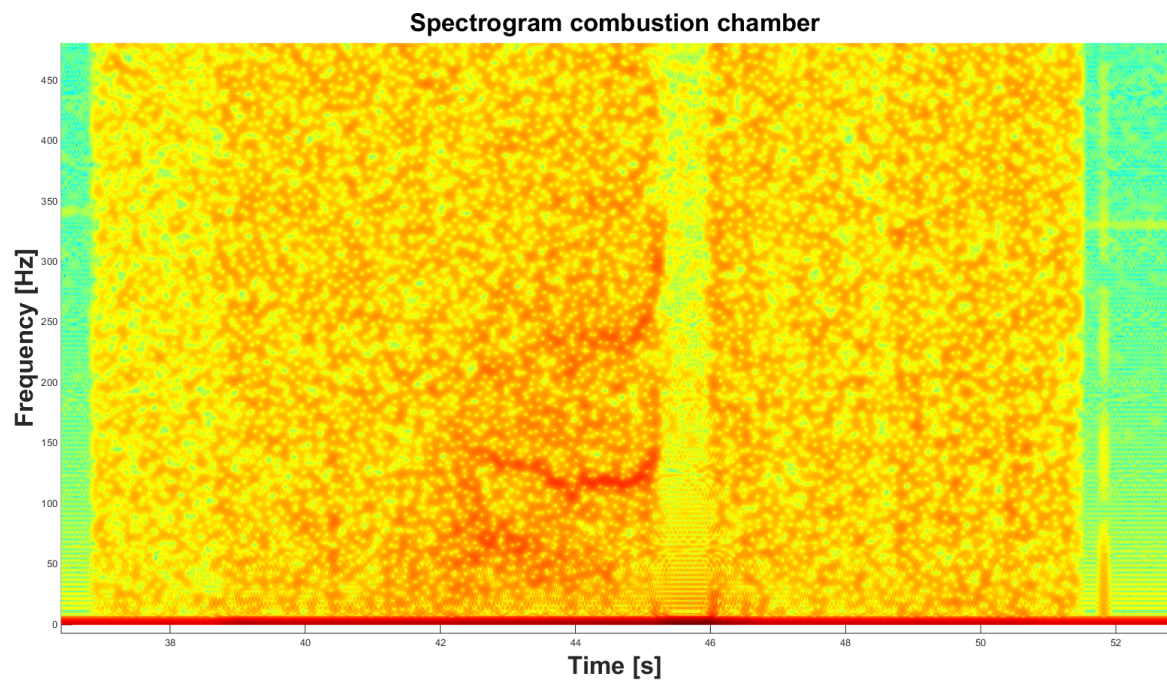


Figure 6.3: Spectrogram of chamber pressure of HypT7-10

6.2. HypT9

HypT9 was conducted using motor 2 which was fired a total of 5 times for a total burn time of approximately 31s. Testing was halted at test 6 due to structural failure of the P_C port at the silver solder connection.

HypT9-6 was the longest of the tests at 15s and also displays many of the characteristics of other burns, hence it will be the only test of this series presented.

Figure 6.4 displays the pressure traces for HypT9-6. It shows a total engine burn of 15s duration. During the burn, the motor shows two distinct phases; firstly, a startup of 4s duration (0 to 4s) followed by a stable burn of 11s duration (4 to 15s).

Figure 6.5 shows a close-up of the chamber pressure and both oxidizer and fuel feed pressures during the motor startup phase, at 1.3s. It can be seen that there is a periodic fluctuation in both the combustion chamber pressure and the oxidizer feed pressure. The peak-to-peak amplitude of the fluctuations are approximately 0.8 and 0.25bar respectively. It is notable that the combustion chamber pressure often exceeds the oxidizer feed pressure although the degree of overlap is less than the measurement error of the sensors. Figures 6.7 and 6.8 show that the instability observed during the startup period occurs at a frequency of 140 Hz and is strongly present in both the combustion chamber pressure and oxidizer feed line at similar frequencies. This instability does not appear in the fuel feed line spectrogram. See Figure 6.9. The combustion chamber also displays another significant instability at 550 Hz which does not appear in either the fuel or oxidizer feed spectrograms.

During the second phase of the burn (4 to 15s), Figure 6.7 shows that the 140Hz instability has decreased in intensity significantly. Figure 6.6 shows the pressure traces at 11s where it can be seen that chamber pressure peak-to-peak amplitude has decreased to 0.2 bar and no longer exceeds the oxidizer feed pressure at any point.

Figure 6.10 shows that the oxidizer mass flow rose from 1 to 1.6g/s at 1s. This corresponds with the transition from unstable to stable combustion as well as an increase in the average $\Delta P_{Ox\ injector}$ from 0.27 to 0.4 bar. The fuel flow stays relatively constant between .18 and .2 g/s throughout the startup phase and burn. $\Delta P_{Fuel\ injector}$ stayed constant at 0.5 bar throughout the majority of the burn. It can be seen that the O/F ratio is approximately 5 during the startup phase of the burn but increases to between 9 and 11 for the majority of the burn.

Figure 6.11 shows that the C* performance of the motor fluctuates somewhat during the startup phase however stabilizes at to between 91 and 93% until 12.5s where it begins to deteriorate to a value of 86% before the motor is shutdown.

At motor shutdown the pressure port, located at the start of the convergent section, was found to be damaged. The silver solder used to seal the port which melts at 876K was seen in video to be ejected from the motor. The pressure port stayed in place however the motor was no longer in an operable state and testing was halted. The spark plug showed heat damage and cracking in the porcelain insulation. Pressure testing revealed that it had developed a leak at pressures above 2 bar. The spark plug suffered damage to the tip after it was first used in that the tip was completely melted away, short circuiting the electrode to the outside of the spark plug, resulting in no ignition in the following test. This was resolved by grinding away the obstructing material with a file. Further tests with the same spark plug ignited successfully.

No temperature data on the motor itself was collected. Video footage shows the nozzle end of the motor becomes visibly discoloured due to heating as can be seen in Figure 6.12.

From Figure 6.4 it can be seen that the motor has a shutdown period of approximately 2.5s before chamber pressure reaches close to zero. This roughly corresponds to the decay in oxidizer flow however fuel flow continues for more than 5s after motor shutdown.

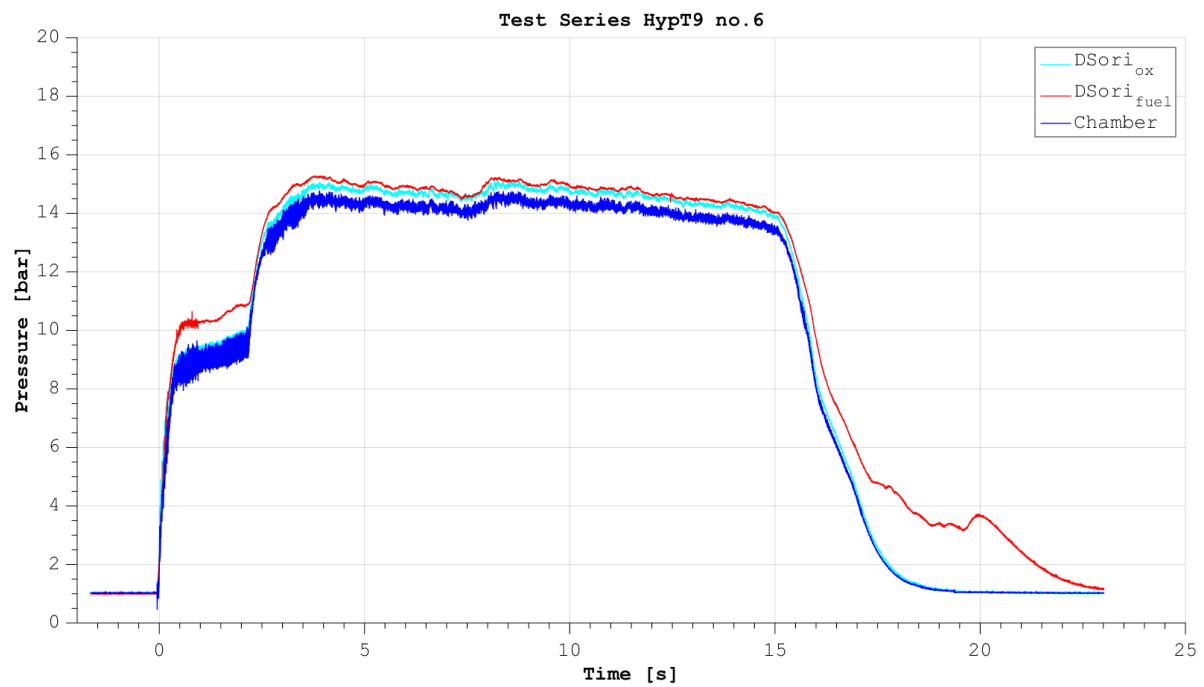


Figure 6.4: Pressure data of HypT9-6

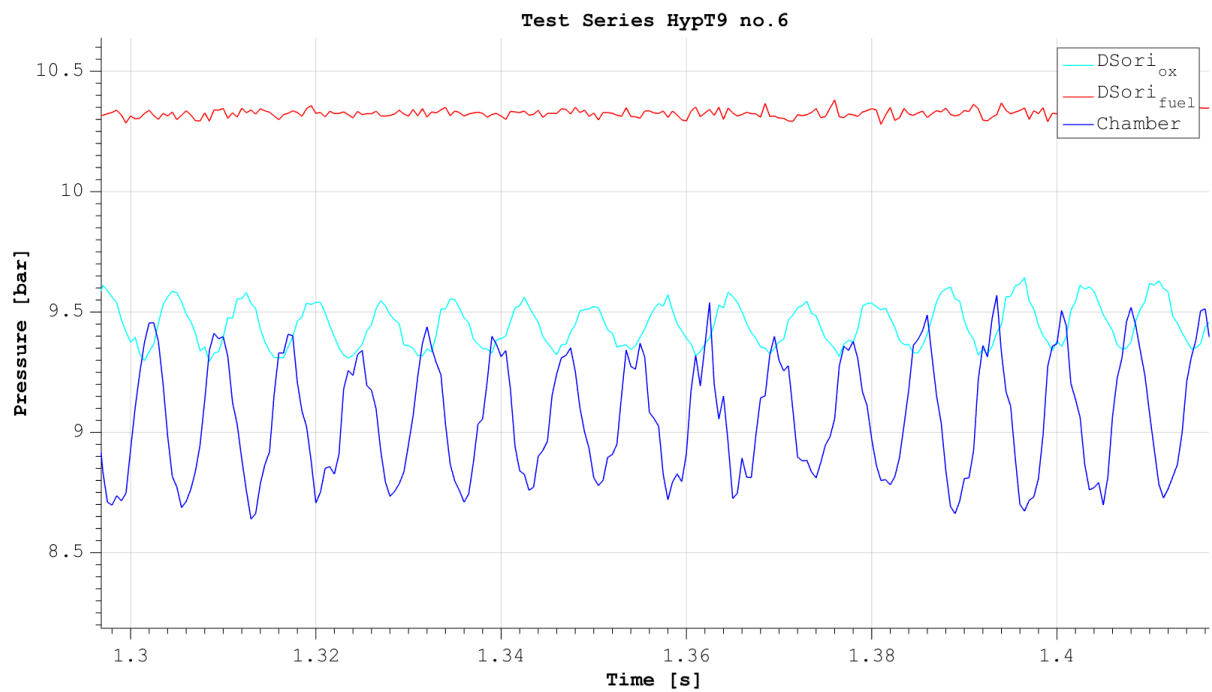


Figure 6.5: Pressure data of HypT9-6, close-up at 1.3s

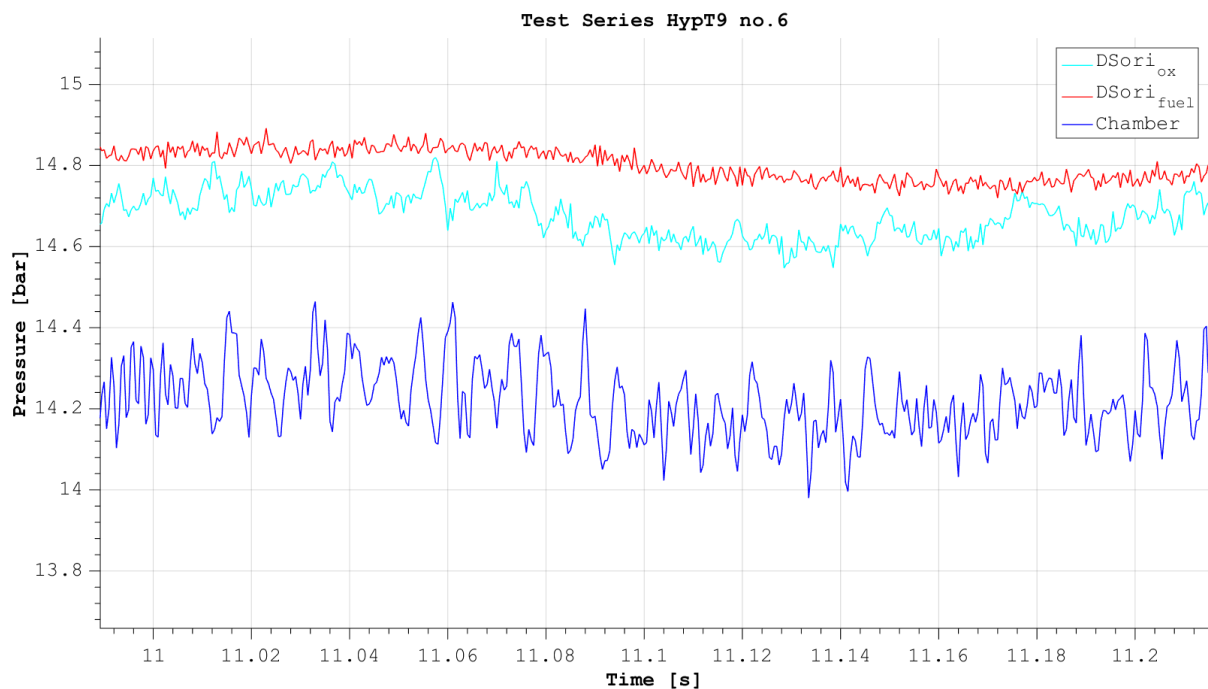


Figure 6.6: Pressure data of HypT9-6, close-up at 11s

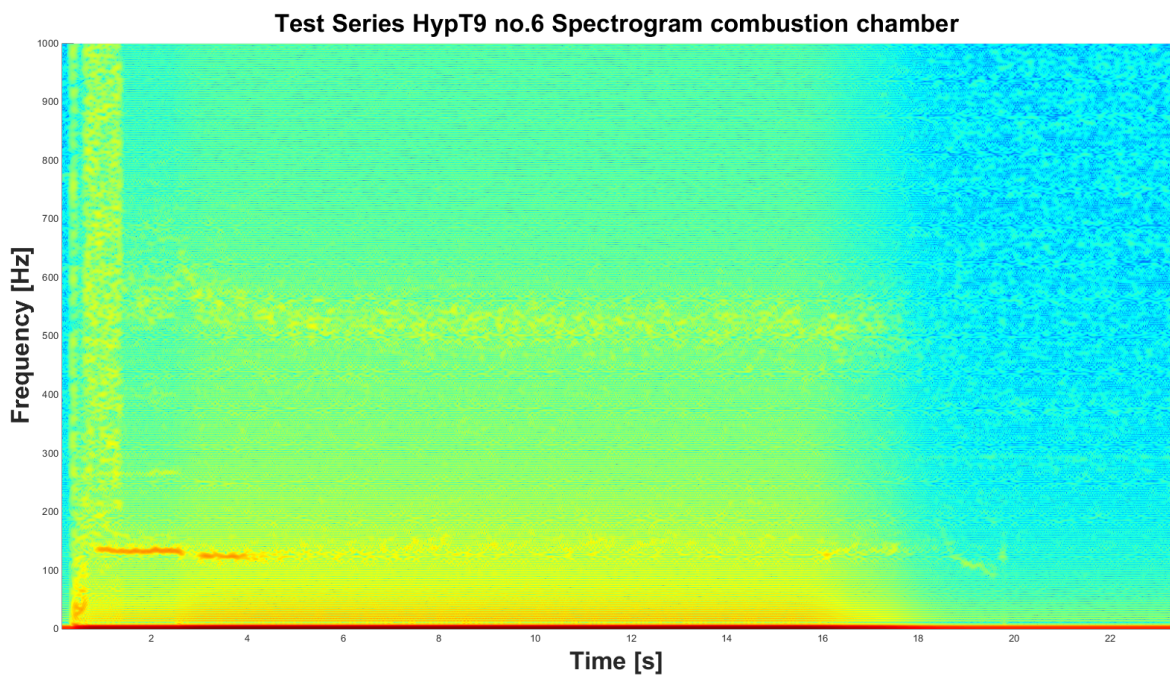


Figure 6.7: Spectrogram of combustion pressure of HypT9-6

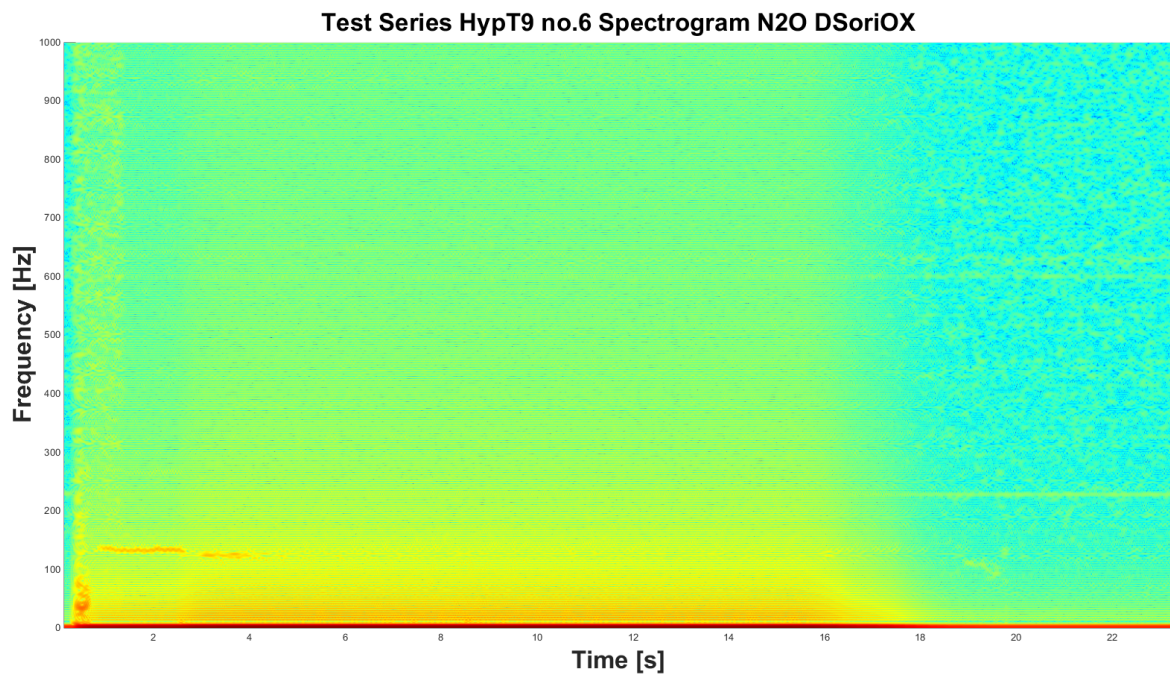


Figure 6.8: Spectrogram of oxidizer injector pressure of HypT9-6

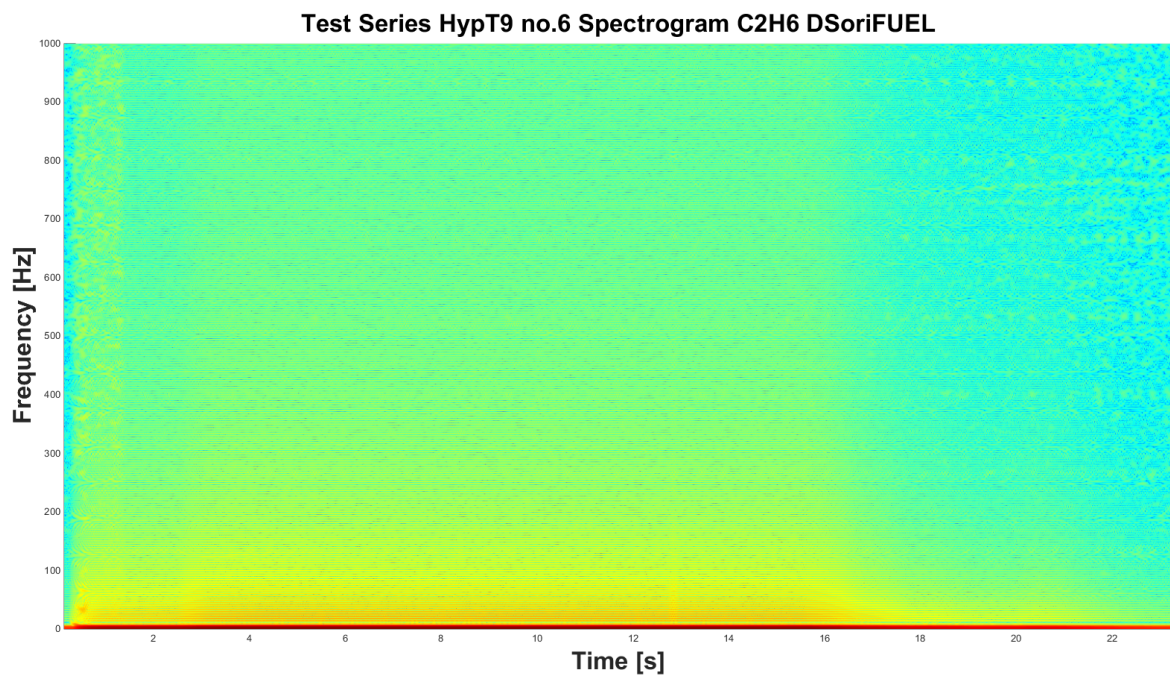


Figure 6.9: Spectrogram of fuel injector pressure of HypT9-6

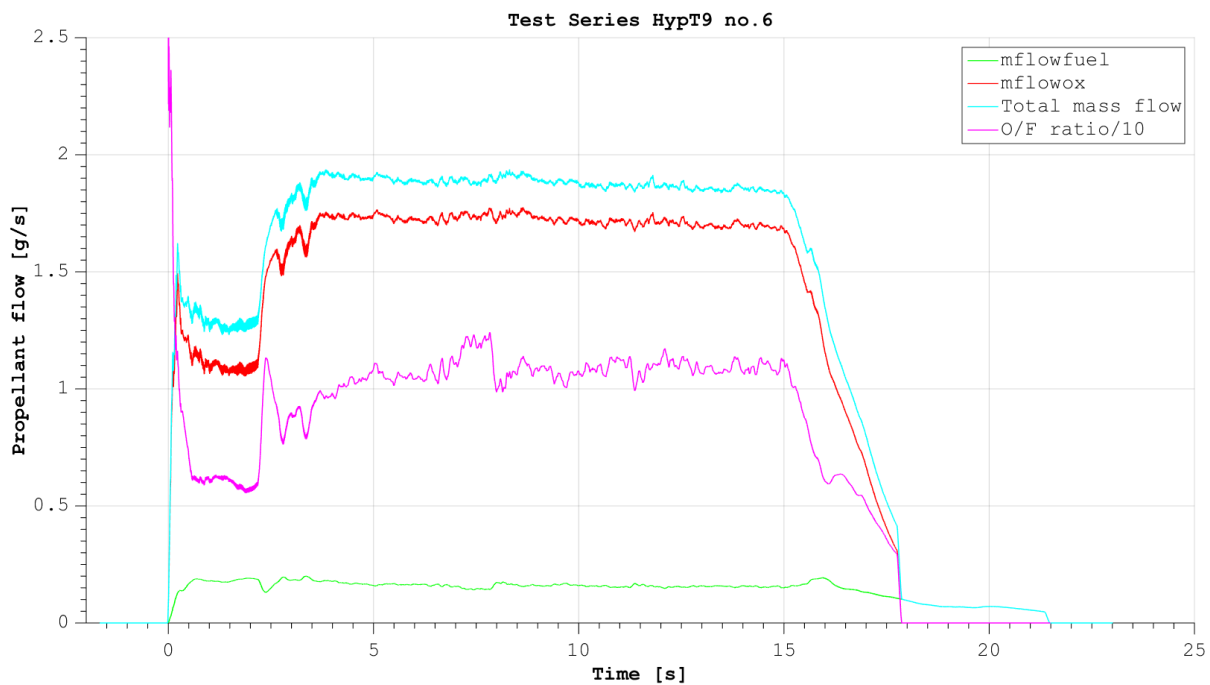


Figure 6.10: Mass flow data of HypT9-6

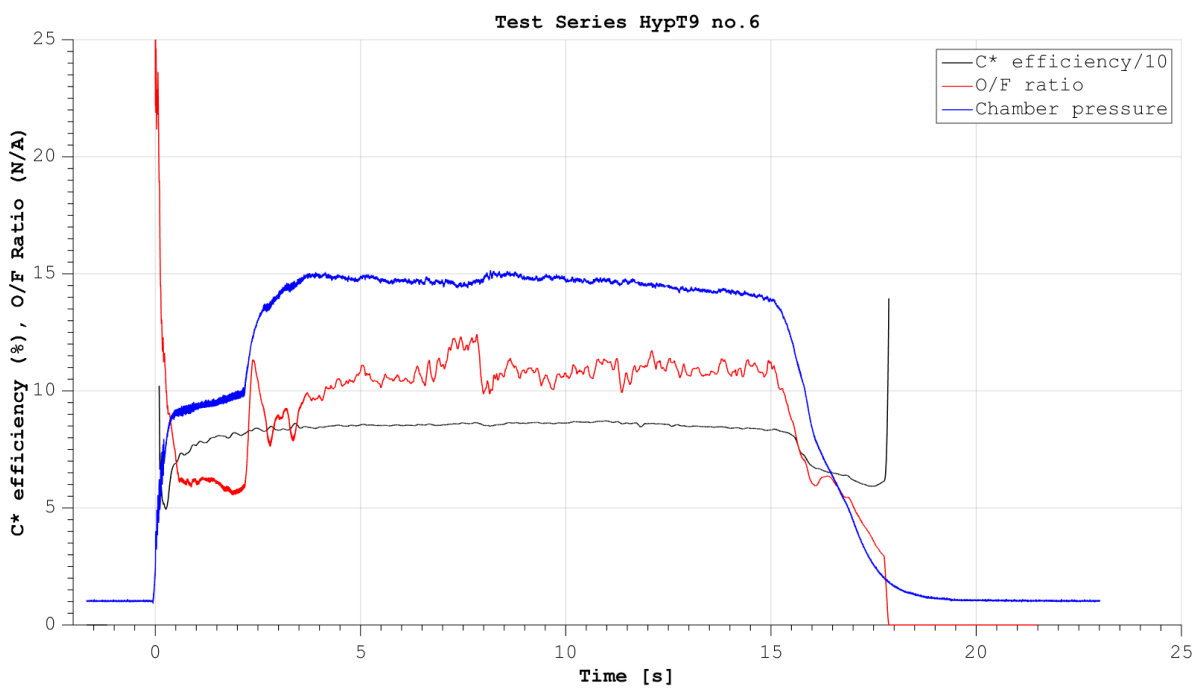


Figure 6.11: C Star performance data of HypT9-6

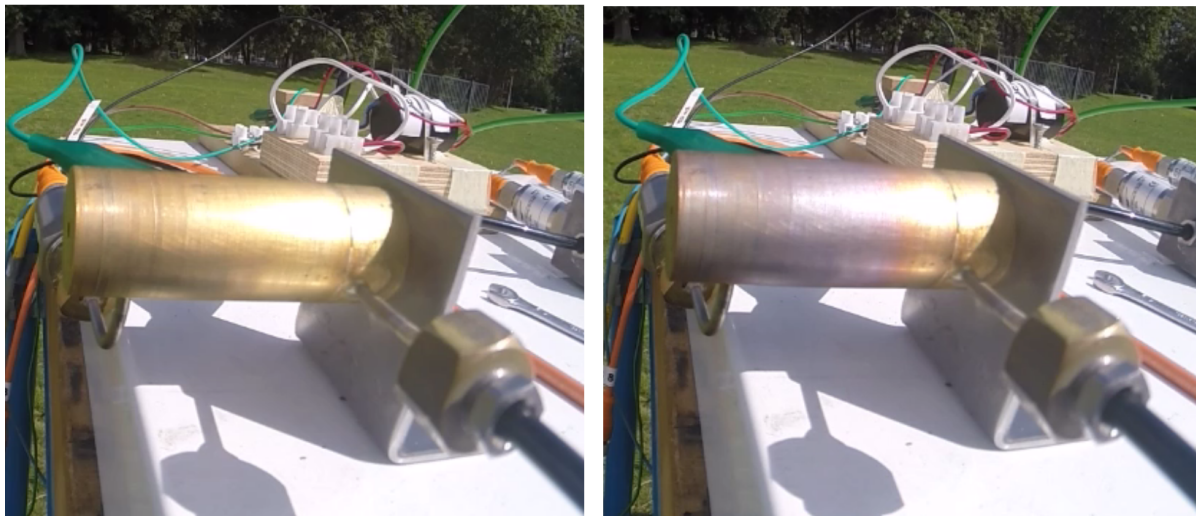


Figure 6.12: Motor 2 before and after HypT9-6

6.3. HypT10

The HypT10 test series was conducted using motor 3. Motor 3 is largely similar to motor 2 except that a regenerative cooling cycle utilizing oxidizer as coolant was added and the oxidizer injector port was decreased in size from 1.3 to 1mm diameter. The internal chamber geometry was identical to motor 2.

A total of 18 starts were conducted in 9 hot fire tests. Test 8 will be discussed in this section as it exhibits most interesting phenomenon encountered during this test series.

HypT10-8 was a 6s burn with the igniter being fired for 1s at the start of the burn. As with HypT9-6, the motor displays two distinct phases in the burn where the motor operates with reduced thrust for the first 2.5s. This can be clearly seen in Figure 6.13. The increase in thrust corresponds with an increase in oxidizer mass flow seen in Figure 6.15. The O/F ratio shifted from 6 to 10 during the first 2.5s of the burn and then stabilised between 9 and 10.

Figure 6.3 shows that unlike HypT9-6, there is no instability present at 140Hz. The instability amplitude at 600Hz has however increased significantly in strength and appears to worsen slightly throughout the burn duration. No instabilities were observed on either the fuel or oxidizer feed and hence these graphs are not presented.

Figure 6.2 shows that the temperature in the regenerative cooling cycle increased until motor shutdown by which time the temperature was 590K. It can also be observed that the regenerative cooling inlet temperature decreases slightly throughout the burn however the fuel inlet temperature does not. From Figure 6.16 the heating power of the regenerative fluid has been calculated and is presented in Figure 6.17. This figure shows that the heating power steadily increases throughout the motor burn until a peak of 240 watts when the motor is shut down.

Figure 6.18 displays the C* efficiency of the motor during the burn. Excluding the startup period, a C* of 85 - 86% was measured. It is to be noted that the nozzle had suffered damage during production whereby the throat was likely to have been compromised to an unknown extent. The divergent section of the nozzle was visibly asymmetric. Unfortunately, it was not possible to replace the motor or repair the nozzle in the time available, hence testing continued. It is likely that the C* values obtained in this testing are not representative of the actual motor performance.

Start up and shutdown transients are very similar to that of HypT9 and 10, whereby full oxidizer flow lags approximately 2.5s and where the fuel feed pressure is maintained for many seconds after motor shutdown. The startup transient could however be reduced to around 1s if the propellant feedlines were previously primed, for example by repeating firings in quick succession. This was performed in HypT10-9 where the motor was fired in successive 3s burns, 5s apart. After the third burn, the startup transient had been reduced to approximately 1s.

During the 5th burn of HypT10-9, the motor suffered a breach in the inner cooling jacket. Two of the chamber wall breaches are visible in Figure 6.19 and a third was found on the section removed from the motor. The chamber breach caused oxidizer to bypass the regenerative cycle and be dumped directly into the motor, hence very little flow went through the regenerative cycle and further through the oxidizer injector as intended. This led to other sections of the inner wall also overheating, further exacerbating the problem. The fault was not originally recognised and testing was continued for a further six restarts where the motor acted erratically due to nozzle clogging, low oxidizer injector pressure drop and poor mixing. Nonetheless, the motor did successfully start on all six further firing attempts before testing was halted.

Figure 6.19 shows that in the last tests where the inner wall was already breached, very fuel rich combustion occurred in the top section of the motor. This is indicated by the thick black soot coating. Downstream of the chamber failure where oxidizer was still being injected into the motor, the chamber wall has little or no soot buildup.

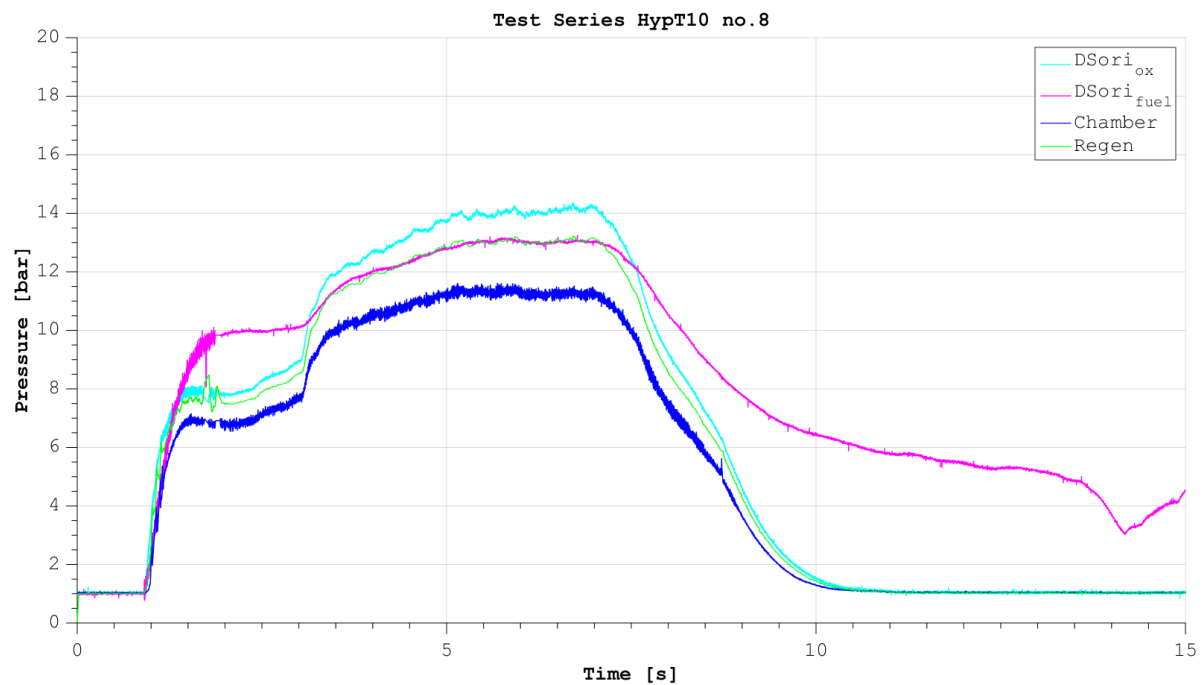


Figure 6.13: Pressure data of HypT10-8

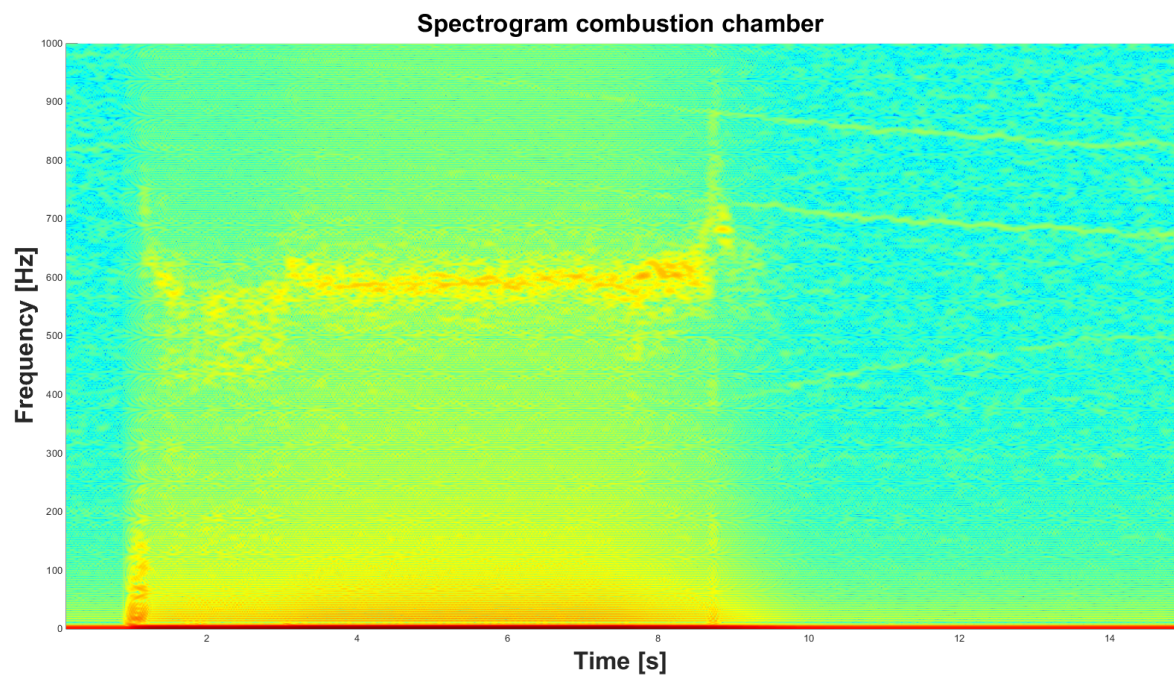


Figure 6.14: Spectrogram of combustion pressure of HypT10-8

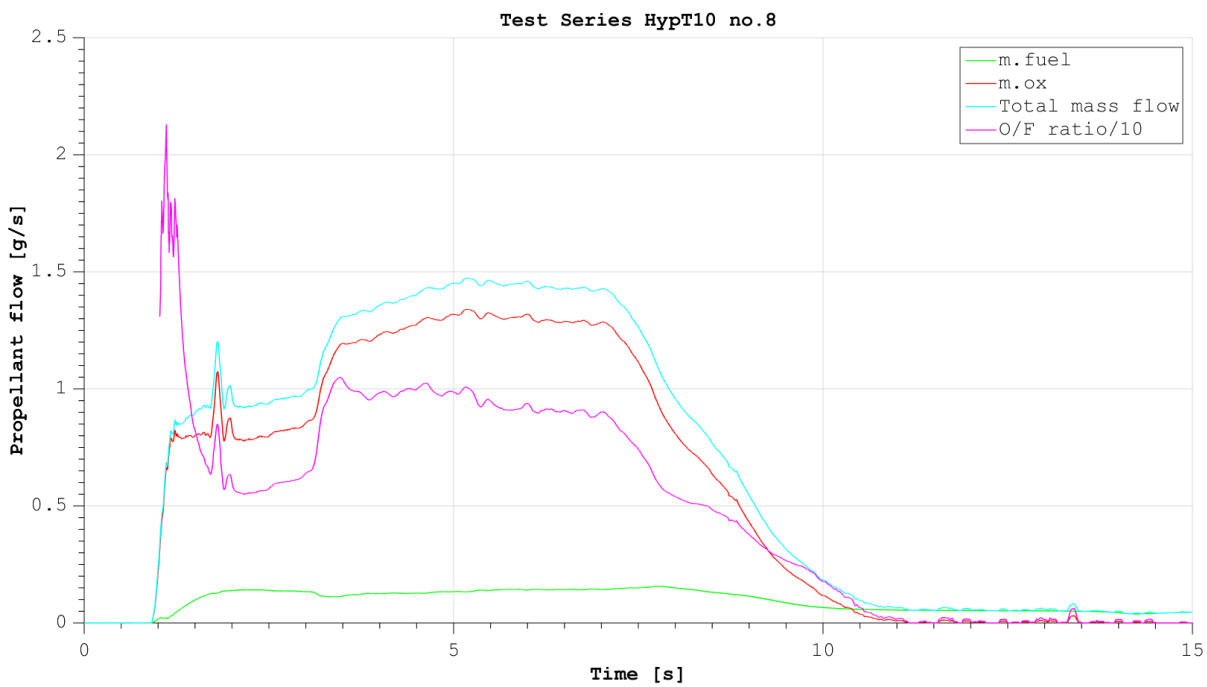


Figure 6.15: Mass flow data of HypT10-8

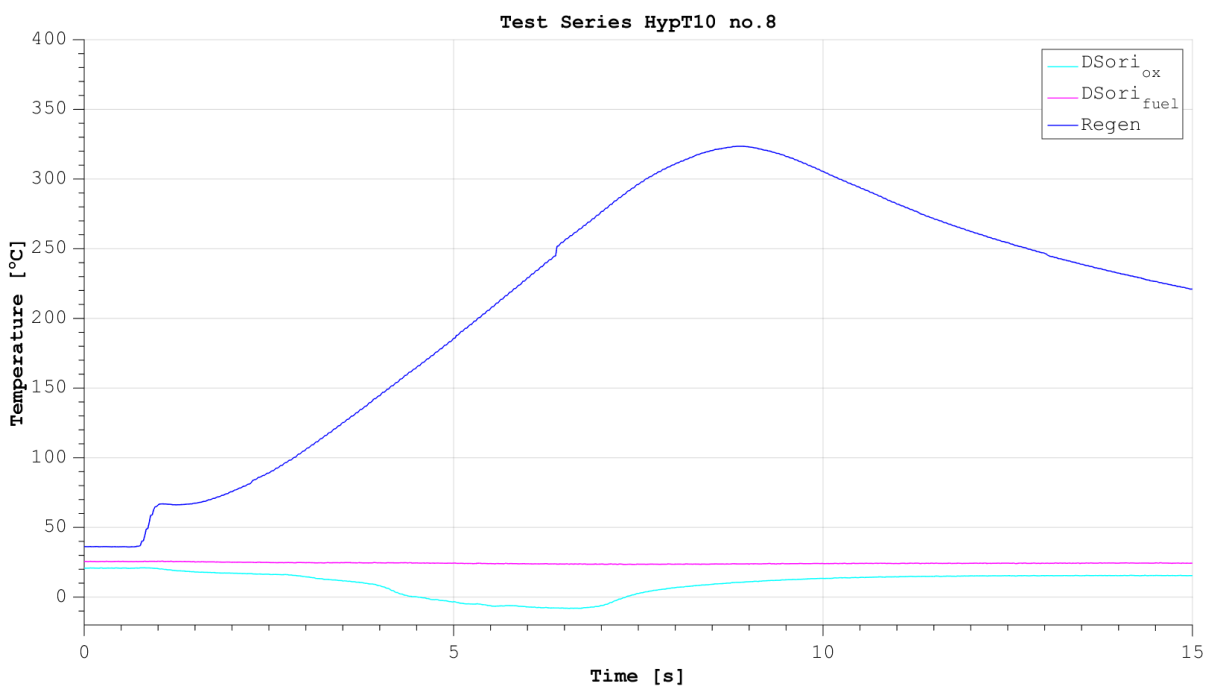


Figure 6.16: Temperature data of HypT10-8

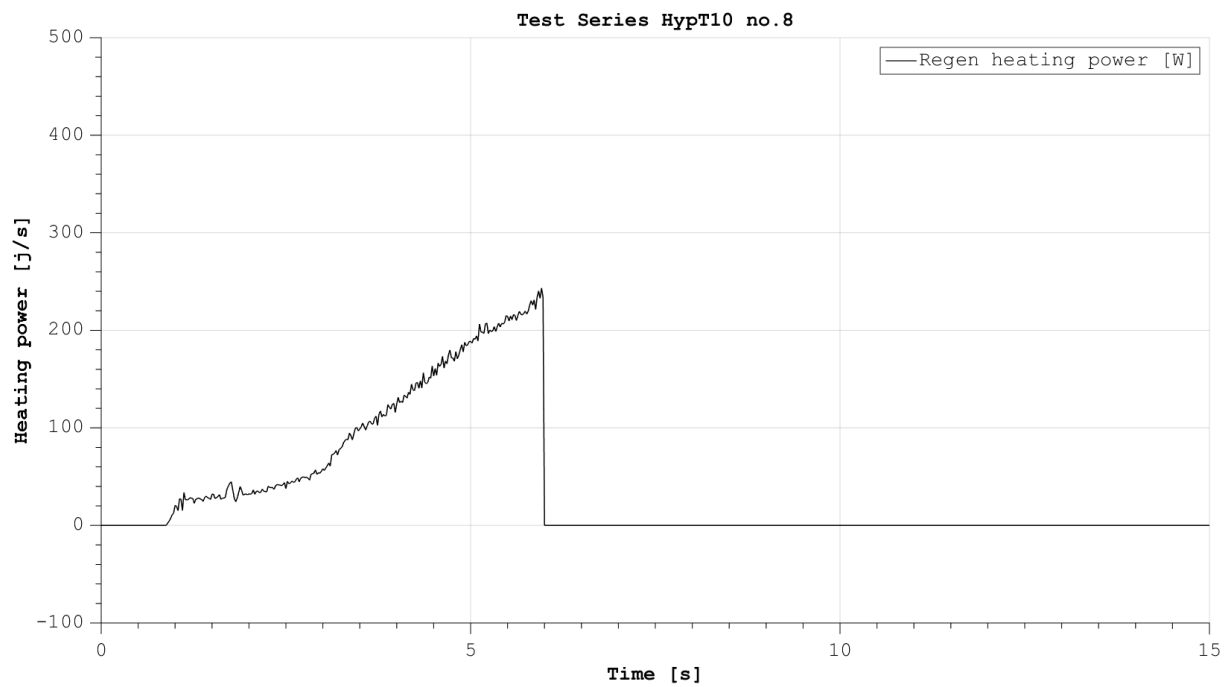


Figure 6.17: Calculated cooling power in regenerative cycle of HypT10-8

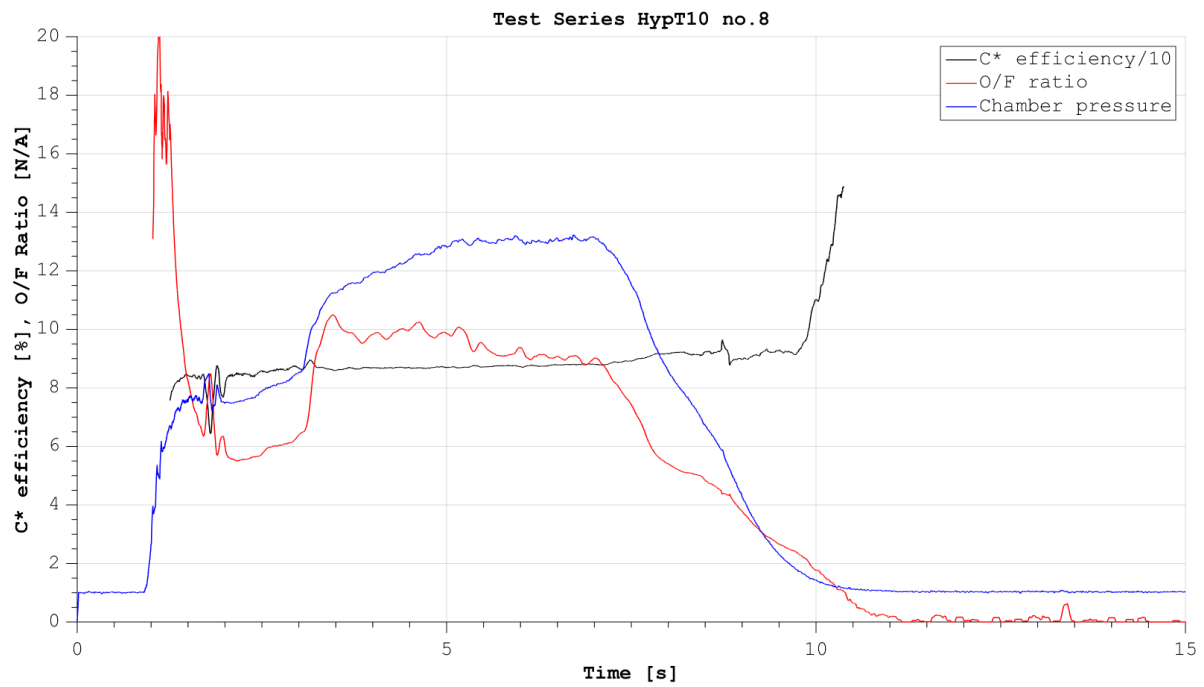


Figure 6.18: C Star performance data of HypT10-8

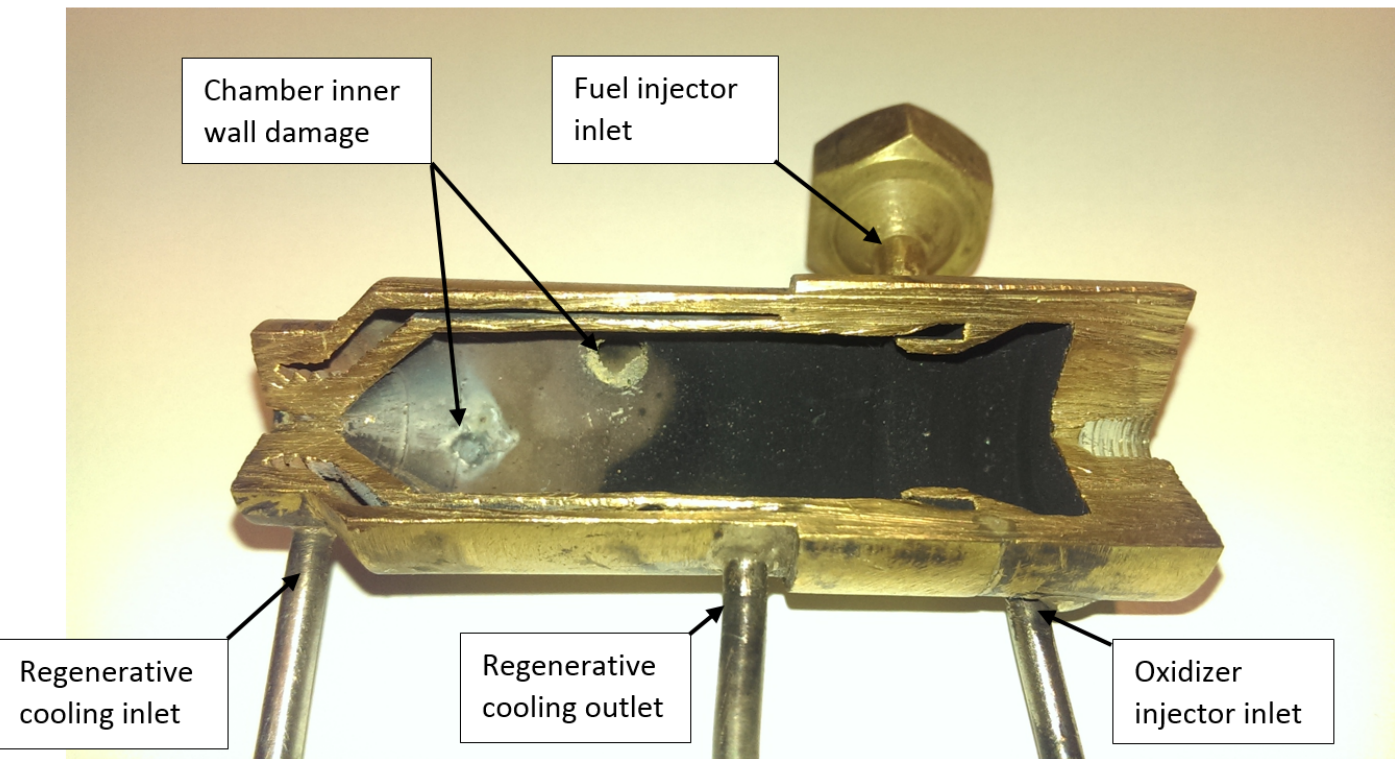


Figure 6.19: Motor 3 cross-section after the HypT10 test series.

6.4. HYPT12

HypT12 was the final test series performed. Motor 4 was used for these tests. Motor 4 featured the same injector configuration as motor 3 but the L* of the motor had been reduced from 3.1 to 1.1. Also, a more effective regenerative cooling cycle was implemented to increase the possible burn time of the motor.

HypT12 included 20 successful restarts on a single motor configuration. No components, including the sparkplug, were exchanged or cleaned between tests. The longest burn during this test series, test 16, ran for a total of 30s. The accumulated burn time on the motor was 125s.

Testing was discontinued after test 17, burn #5, when the fuel injector inlet was damaged due to high temperature. This occurred after successive short duration restart tests where the motor was not allowed to cool down between burns. This resulted in the surface temperature exceeding 450 °C, causing the silver solder connection of the fuel inlet to fail in much the same manner to that which had occurred to the pressure port in HypT9-6.

Test 16 will be examined closely as it encompasses the most interesting phenomenon encountered, in addition to test 17, burn #5, as it is the test that best represents how the motor was intended to operate.

6.4.1. HYPT12-16

Figure 6.20 shows that the motor ran for a total of 30s through two distinct phases. The startup phase of 3s followed by the nominal burn phase of 27s. During startup, the motor displays a strong instability at 18Hz. This can be seen in Figure 6.21. The instability can also be clearly observed in both propellant feed pressures. After the startup phase, the pressure stabilises at 14 bar and slowly decays over the course of the burn. Motor shutdown occurs within 1s of the valves being closed.

Figure 6.22 shows the mass flow measured during the burn. It can be seen that the oxidizer mass flow during the startup phase is somewhat elevated above the design value of 1.6g/s, peaking at 2g/s, however it decreases throughout the burn. The O/F ratio also shifts from 15 to 10 by the end of the burn.

Figure 6.23 shows that all surface temperatures on the engine increased at a decreasing rate during the burn. This can be observed in the curve of the temperature profile of the 'nozzle surface', 'Ox injector surface'. Only the 'Regen exit surface' measurement does not show this effect. It was observed post-test that this thermocouple was poorly attached due to excessive heating of the aluminium tape connection. At approximately 25s into the test, smoke can be seen coming off the motor, likely from the adhesive on the aluminium tape used to secure the surface thermocouples. By the end of the burn, the thermocouples catch fire for several seconds before self-extinguishing. Post-test inspection found that the surface mounted thermocouples were charred on the sheathing although all still functioned nominally. Notable is that the fluid temperature of both the fuel and oxidizer at the injector inlets increased sharply at the start of the burn by 70 k before reducing. After the initial spike, the fuel temperature stays low while the oxidizer fluid temperature begins to rise as the motor surface temperatures also rise. This is expected as the oxidizer is part of a regenerative cooling cycle while the fuel is not.

Using temperature input of the surface measurements as well as temperature and mass flow of the regenerative cooling fluid, the total heating of the motor could be calculated. This is displayed in 6.24 where it can be seen that the energy dissipated by heating the chamber body, displayed as 'Capacitive heating power', drops throughout the burn while the regenerative heating power constantly increases as the regenerative fluid temperature increases. The sum of both these two effects yields the total heating power of the motor, disregarding any radiation and convective heat transfer to ambient air. The total heating power can be seen to fluctuate between 780 and 880 watts for the majority of the burn, excluding the startup and shutdown where transients effects are prominent. By the end of the burn, the contribution of both regenerative fluid heating and capacitive heating is approximately equal at 400 watts each. At motor shutdown, the capacitive heating power increases sharply as the flow of cooling fluid is stopped.

Figure 6.25 displays the C* efficiency of the motor. During the startup phase, the efficiency is less than 50% however once this phase is over, the efficiency increases to between 92 and 93% and holds stable for the remainder of the burn despite a shift in O/F ratio.

The calculated thrust for HypT12-16 can be seen in Figure 6.26. An expansion ratio of 100 was assumed with a nozzle efficiency factor of 0.96. This burn was integrated and a total impulse of 162 Ns was found.

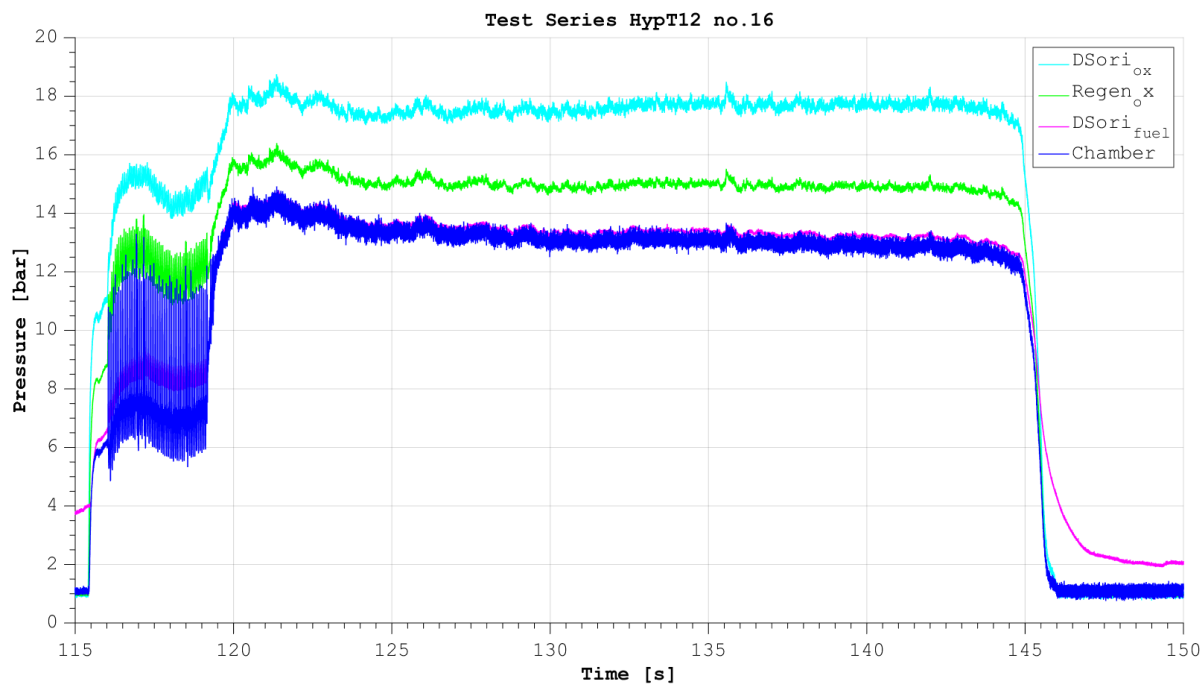


Figure 6.20: Pressure data of HypT12-16

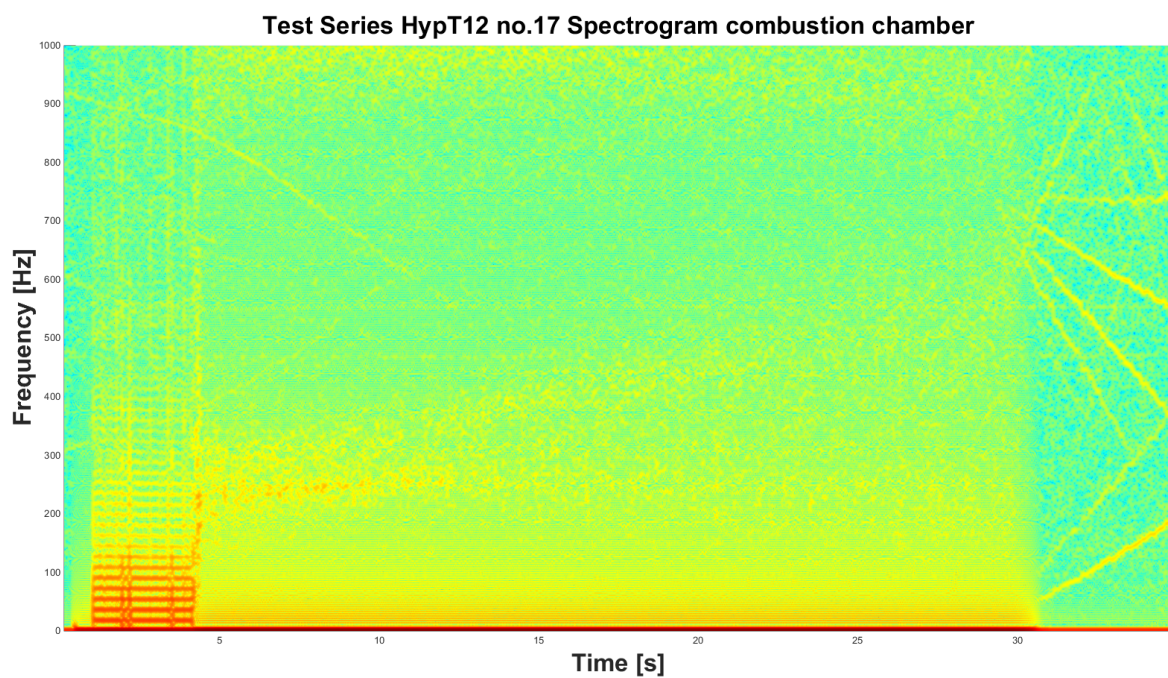


Figure 6.21: Spectrogram of combustion pressure of HypT12-16



Figure 6.22: Mass flow data of HypT12-16

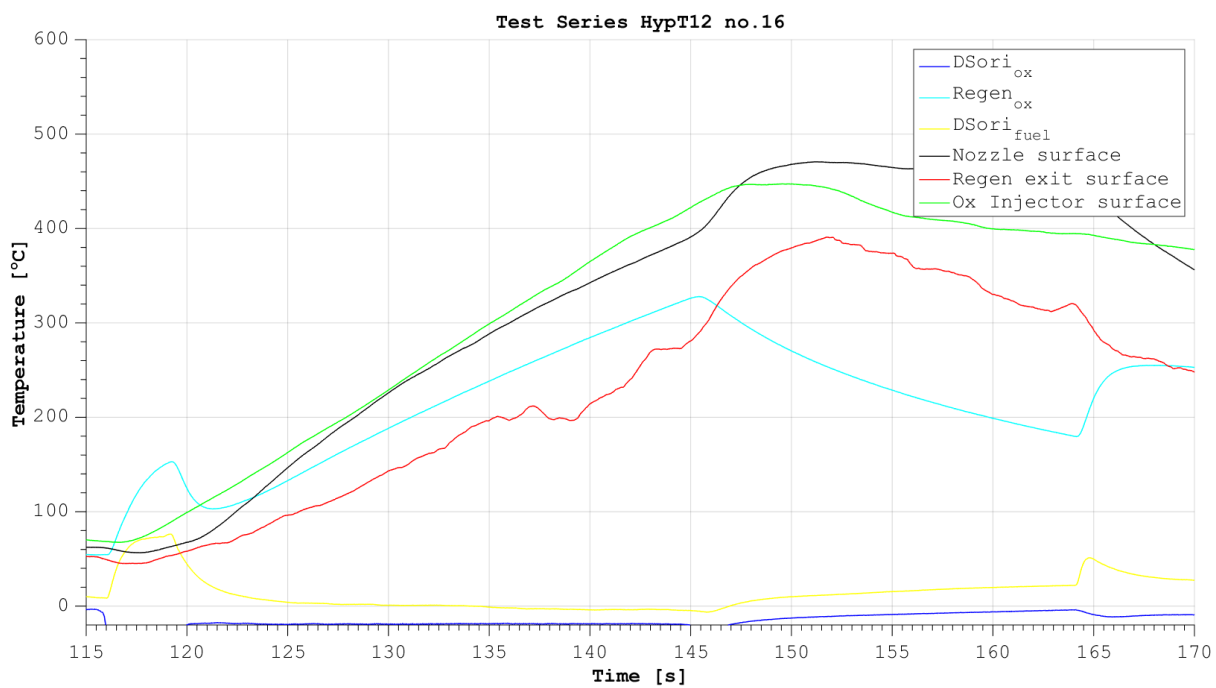


Figure 6.23: Temperature data of HypT12-16

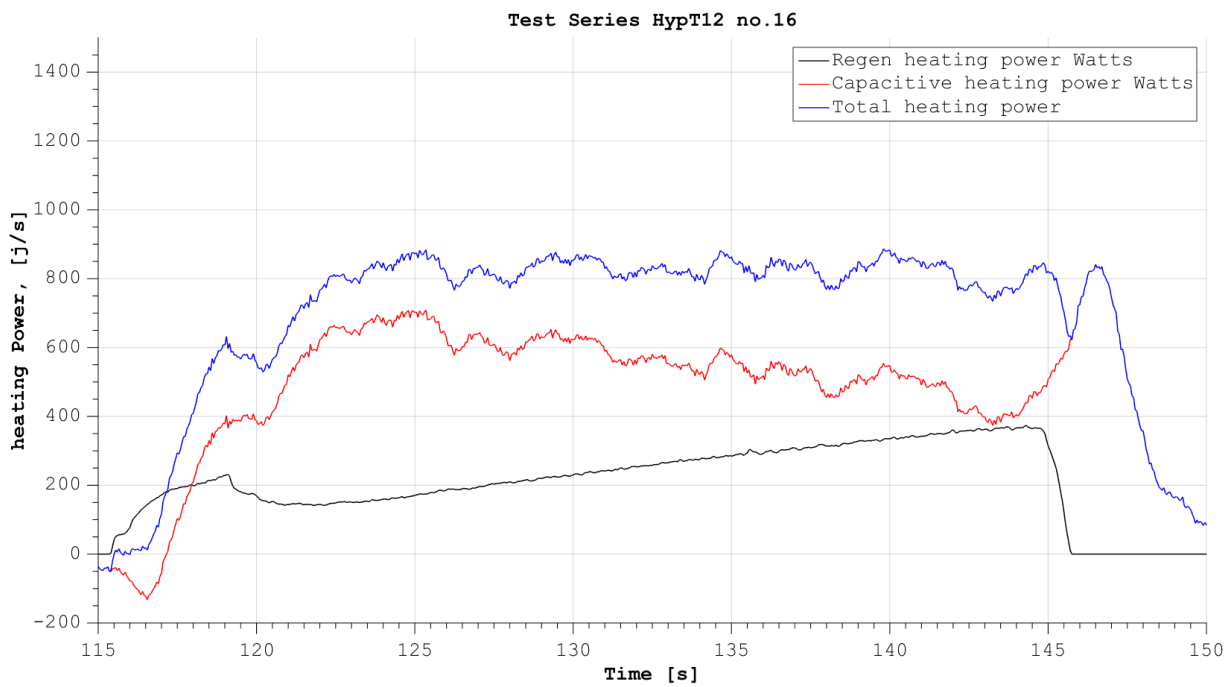


Figure 6.24: Calculated total heating power during HypT12-16

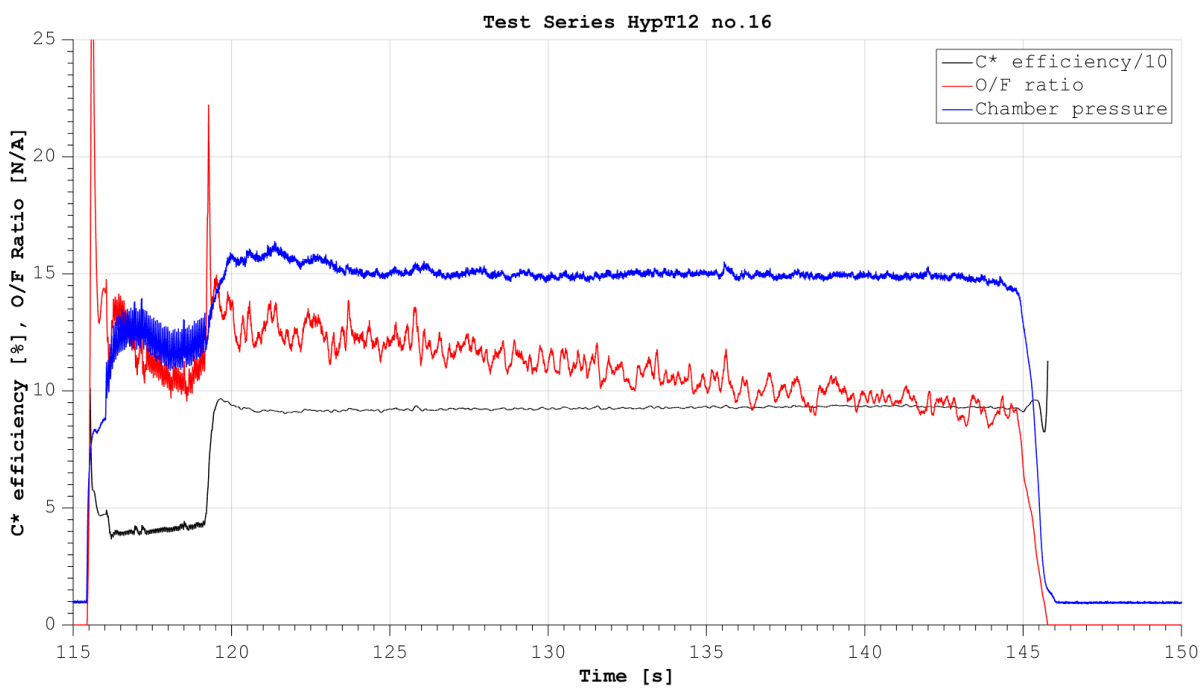


Figure 6.25: C Star performance data of HypT12-16

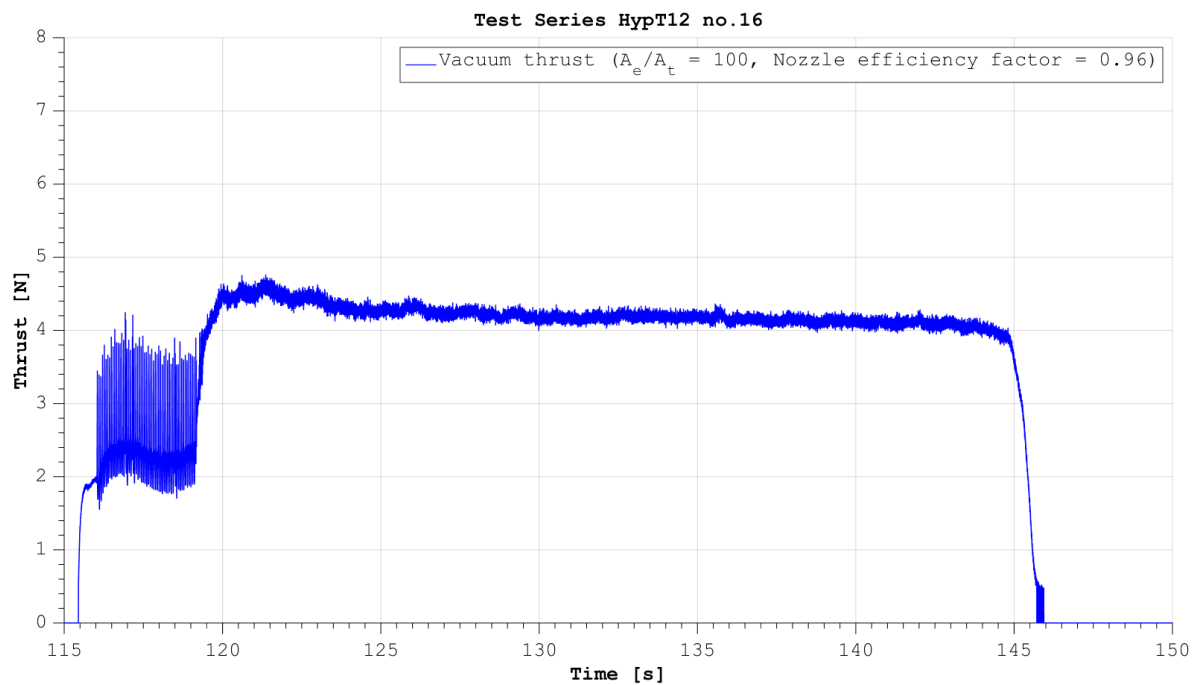


Figure 6.26: Calculated vacuum thrust performance of HypT12-16. $\frac{A_e}{A_t} = 150$, nozzle efficiency factor = 0.96.

6.4.2. HypT12-17, BURN #5

HypT12-17, burn #5 demonstrates a motor burn where the propellant feed system was thoroughly primed and the motor prewarmed to 415 °C on the nozzle surface by 4 previous burns. In this state, it can be seen in Figure 6.27 that startup instabilities are minimal.

The O/F ratio of the burn varies from 25 at the start of the burn to a minimum of 7 before a rise back to approximately 10 before motor shutdown. Despite these rather extreme shifts in O/F ratio, the motor maintains a C* efficiency of between 92 and 96%.

The start of the burn displays a strong instability although from Figure 6.28 the exact frequency at which this instability occurs appears to be undefined. In the last 2s of the burn, an instability at between 200 and 250 Hz develops. This coincides with a increase in O/F ratio from 7.5 to 10.

From Figure 6.30, the motor surface peaked at 470°C. Shortly after this test, the motor failed at the soldered connection between the fuel injection and the inlet port.

The mass flow of oxidizer was found to vary by approximately 10% throughout the majority of the burn, neglecting the startup and shutdown transients.

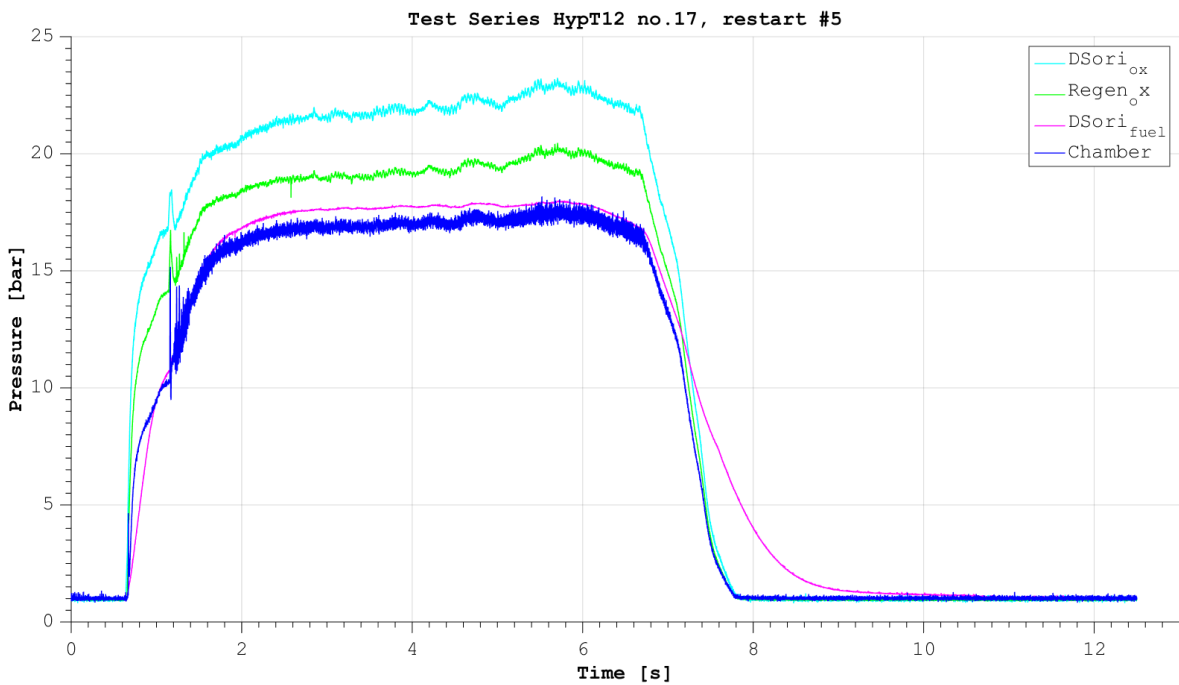


Figure 6.27: Pressure data of HypT12-17, Burn #5

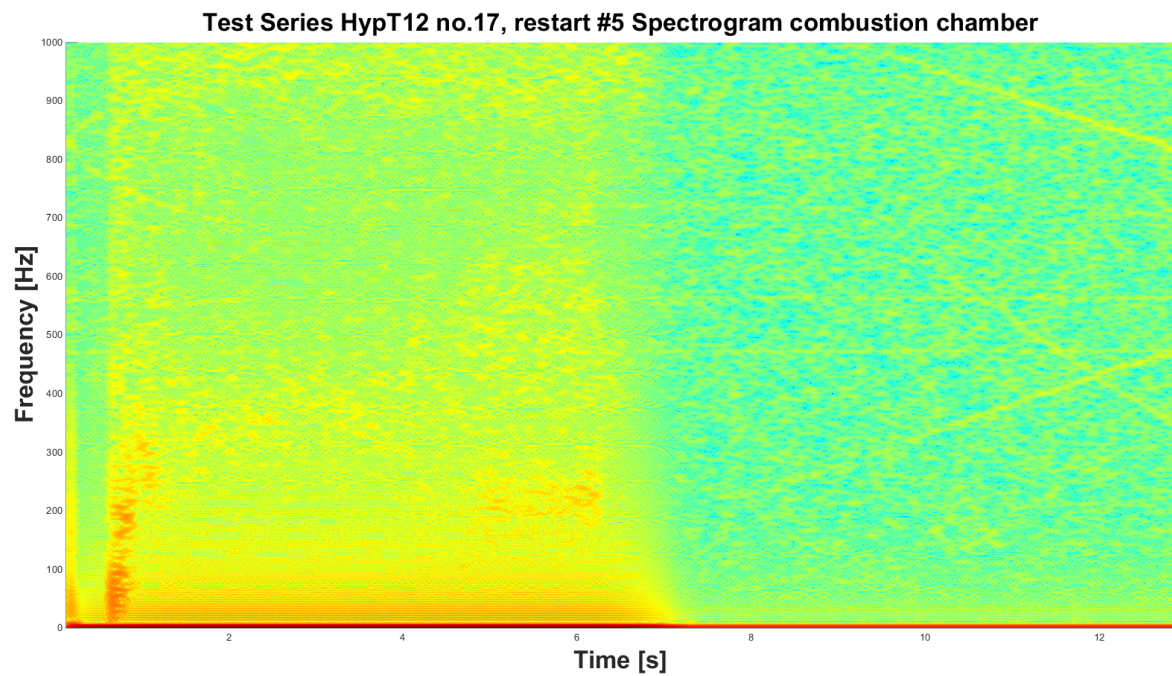


Figure 6.28: Spectrogram of combustion pressure of HypT12-17, Burn #5

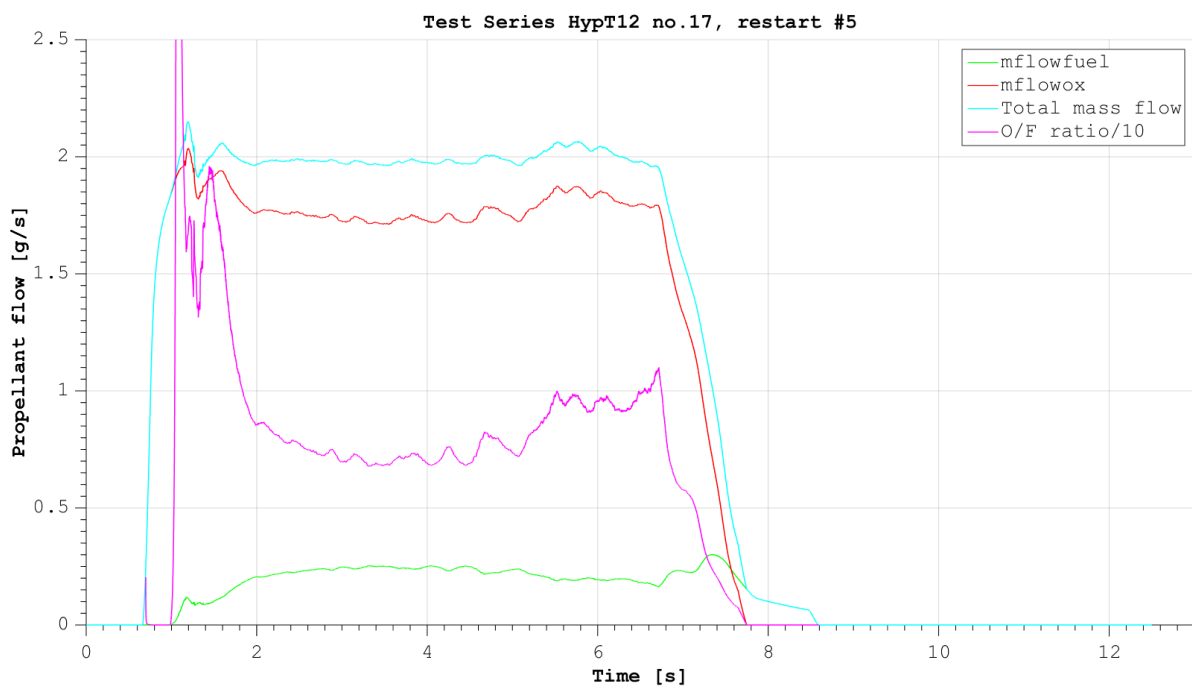


Figure 6.29: Mass flow data of HypT12-17, Burn #5

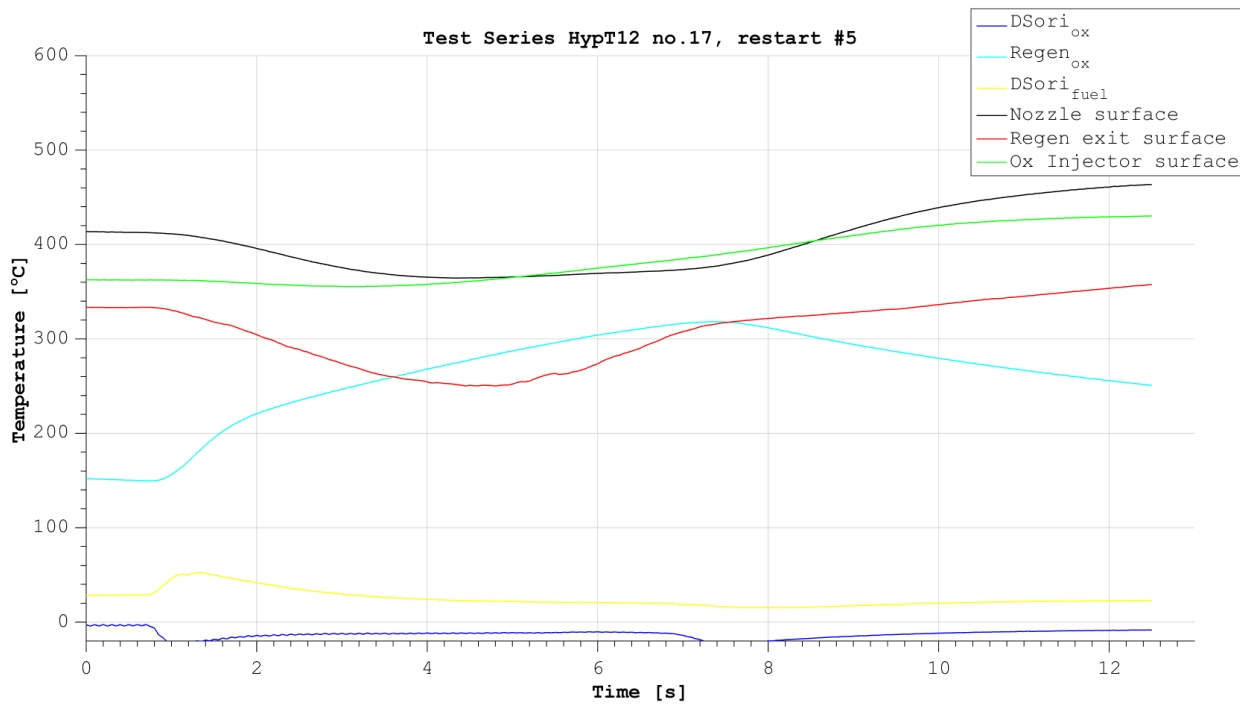


Figure 6.30: Temperature data of HypT12-17, Burn #5

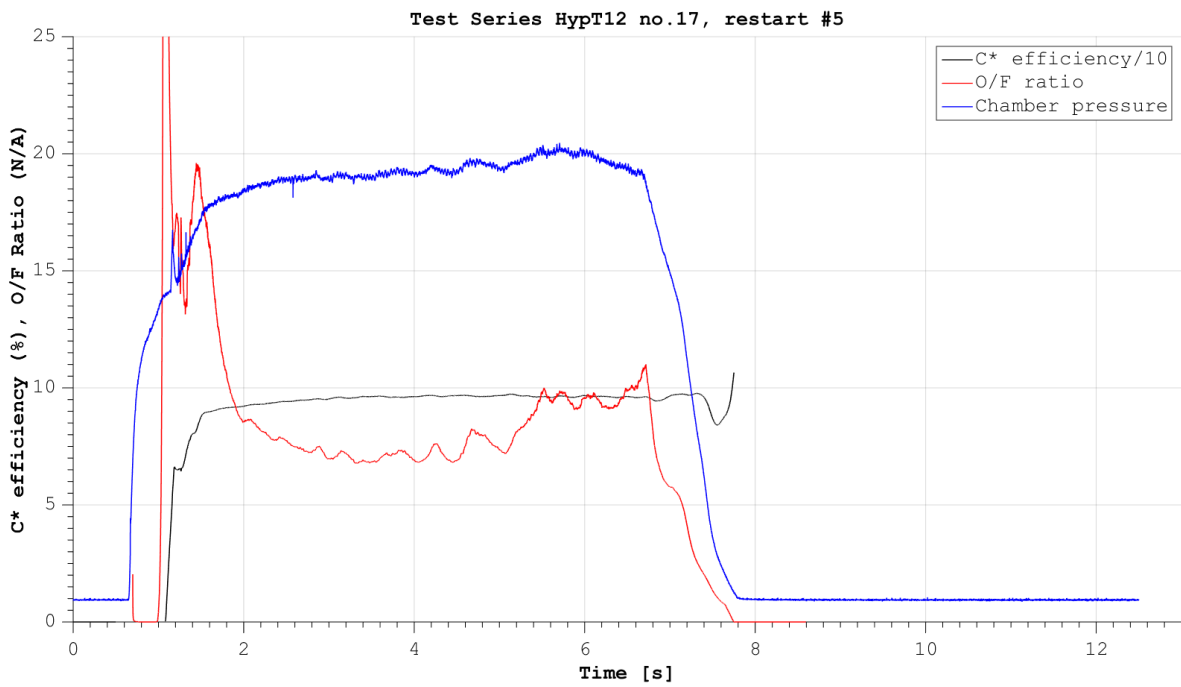


Figure 6.31: C Star performance data of HypT12-17, Burn #5

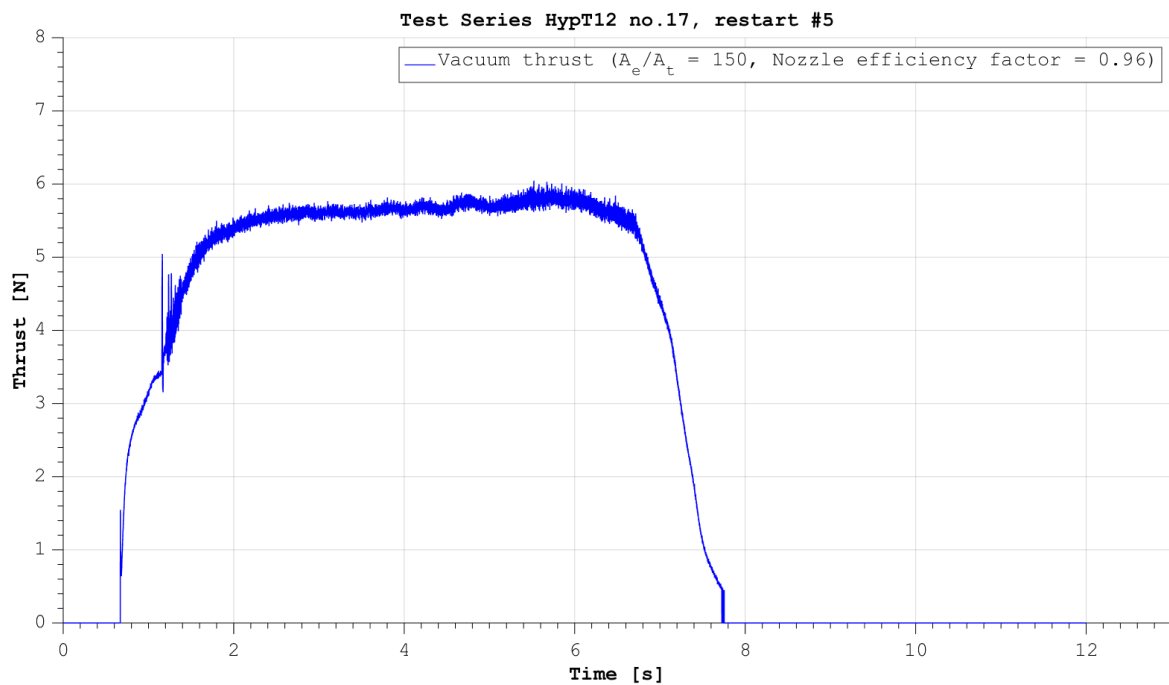


Figure 6.32: Calculated vacuum thrust performance of HypT12-17, Burn #5. $\frac{A_e}{A_t} = 100$, nozzle efficiency factor = 0.96.

6.5. MOTOR BURN REPEATABILITY

Motor 4 was run three times in quick succession for 6s each during HypT12-17. This was done after a series of preheating and feedsystem priming burns. In Figure 6.33 three burns are presented where it can be seen that burn 3 started with a series of pressure spikes for a period of 1s before $P_{Chamber}$ rose in a stable manner. All burns operated at a peak pressure of between 17.9 and 18.9 bar. The main parameters of each burn are summarized in Table 6.3. Figure 6.36 shows that the motor became warmer with each successive burn. Each burn was performed with approximately 15s separation.

The total variation in impulse was found to be 1.9 Ns. The average impulse per burn was 35.3 Ns. Therefore the variation from the mean between burns was found to be +3.1 -2.4%.

Table 6.3: HypT12-17 burns 3,4 and 5 performance summary

Burn number	HypT12-17-3	HypT12-17-4	HypT12-17-5
Burn time [s]	6	6	6
Motor start temperature [deg C]	180	325	415
Motor end temperature [deg C]	340	430	460
Total impulse [Ns]	34.5	36.4	35.1
peak pressure [Bar]	18.8	18.9	17.9
C* efficiency [%]	89-91%	90-97%	90-96%

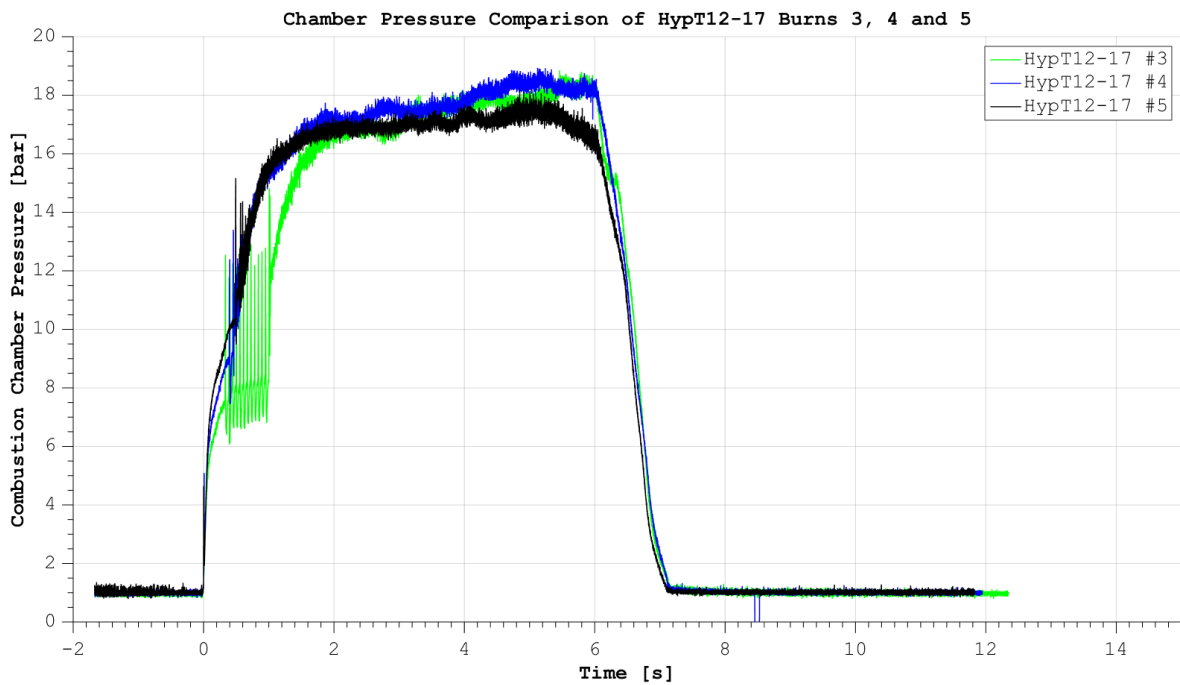


Figure 6.33: Chamber Pressure Comparison of HypT12-17 Burns 3, 4 and 5

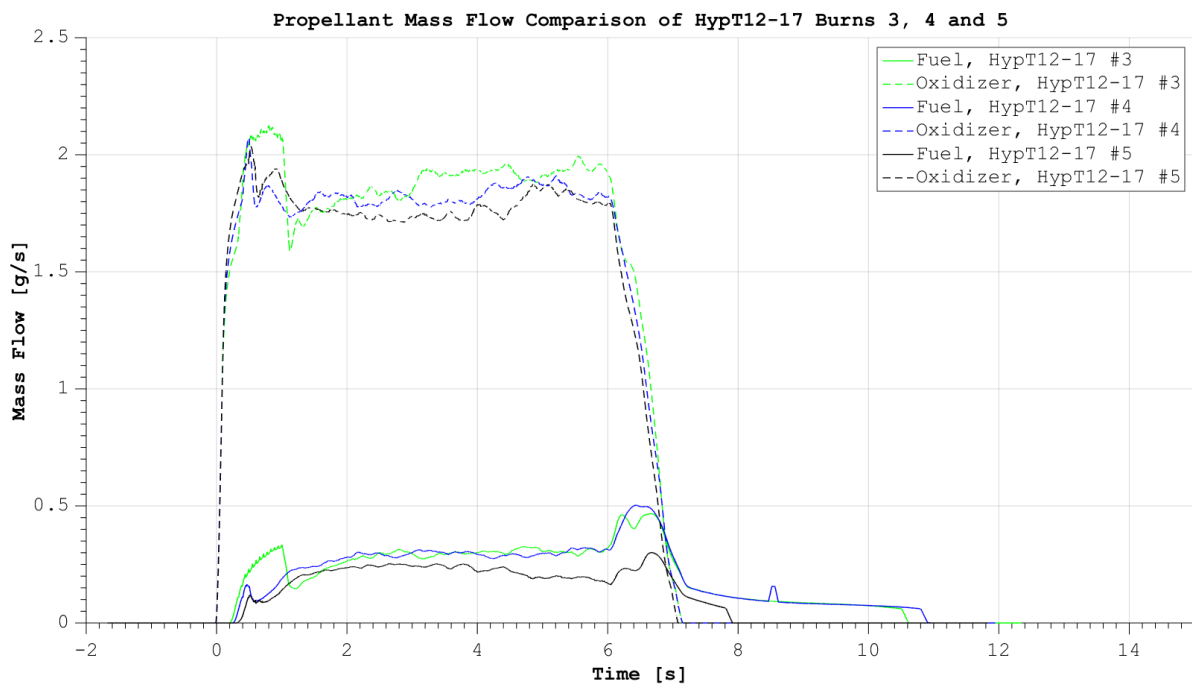


Figure 6.34: Propellant Mass Flow Comparison of HypT12-17 Burns 3, 4 and 5

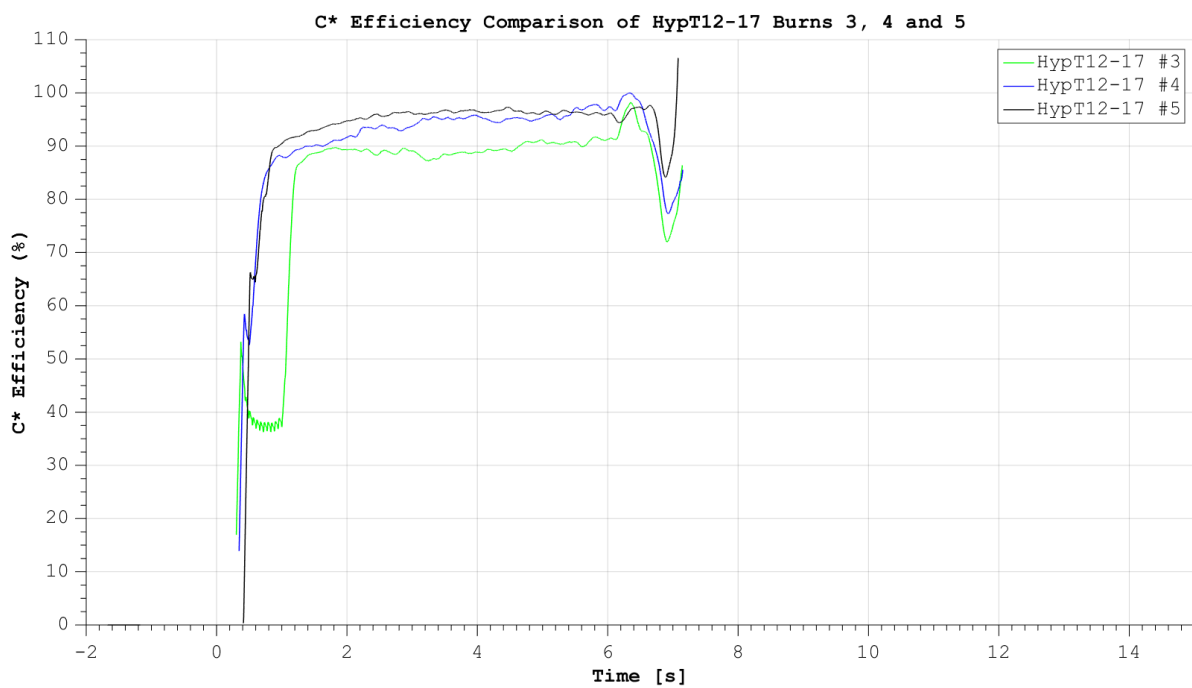


Figure 6.35: C* Efficiency Comparison of HypT12-17 Burns 3, 4 and 5

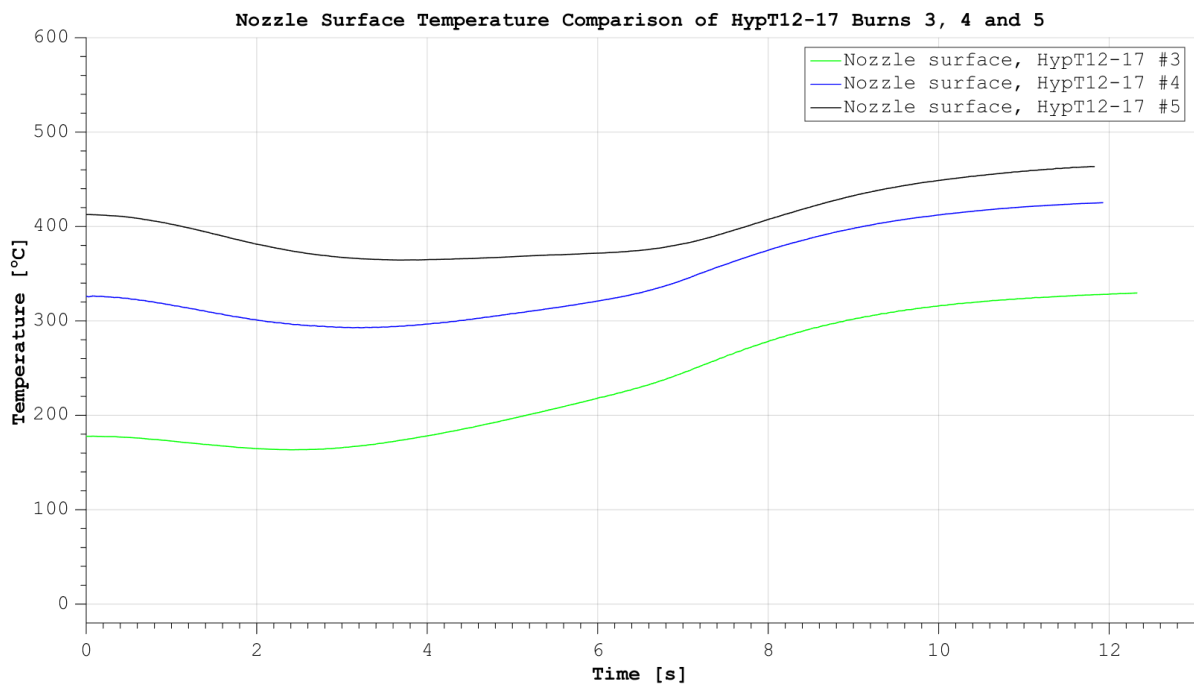


Figure 6.36: Nozzle Surface Temperature Comparison of HypT12-17 Burns 3, 4 and 5

6.6. MOTOR COMPARISON

In Figure 6.37, 6s tests of Motors 2, 3 and 4 can be seen. In these tests, all motors were fired for precisely 6s using automated control. It is apparent that Motor 2 and 4 performed in a relatively similar way while motor 3 appears to be somewhat different. The differences and similarities will be outlined in this section.

6.6.1. STARTUP AND SHUTDOWN TRANSIENT

Motors 2 and 4 showed fast startup behaviour while motor 3 showed the same '2 stage' startup as previously observed in motor 2 during HypT9-6.

Both motors 2 and 3 have a similar shutdown transient while motor 4 has a far steeper shutdown transient. Motor 4 shuts down within 1s of the main valve being closed while motors 2 and 3 take 4 and 3s respectively.

It can be seen that the startup and shutdown phenomenon of each motor closely mimic in shape the respective oxidizer mass flows found in Figure 6.39. The fuel mass flow seems to have only a minor effect on the combustion pressure.

6.6.2. $P_{Chamber}$

The chamber pressure of both motor 2 and 4 closely mimic each other, both reaching a peak of 17 bar. Motor 3 has a peak pressure far lower than the other two motors, at 11.5 bar. Motor 2 has a peak-to-peak noise of 0.5 bar which stays consistent throughout the burn. Motor 3 has a peak noise of 0.4 bar while motor 4 showed a peak-to-peak noise of 0.5 bar which increased to 0.9 bar by the end of the burn. All motors showed some instabilities with motor 4 showing the largest peak-to-peak values.

Motors 2 and 3 show a staggered start in the startup of the motor, starting from $P_{Chamber} = 2$ bar. After 0.2s and five oscillations, while the pressure continues to rise in a stable manner. Motor 4 shows one strong pressure spike at T-0 followed by a set of large pressure spikes at T+0.5s with a peak-to-peak value of 5 bar. The motor then continues to build pressure in a stable manner. This startup behaviour can be seen in Figure 6.38.

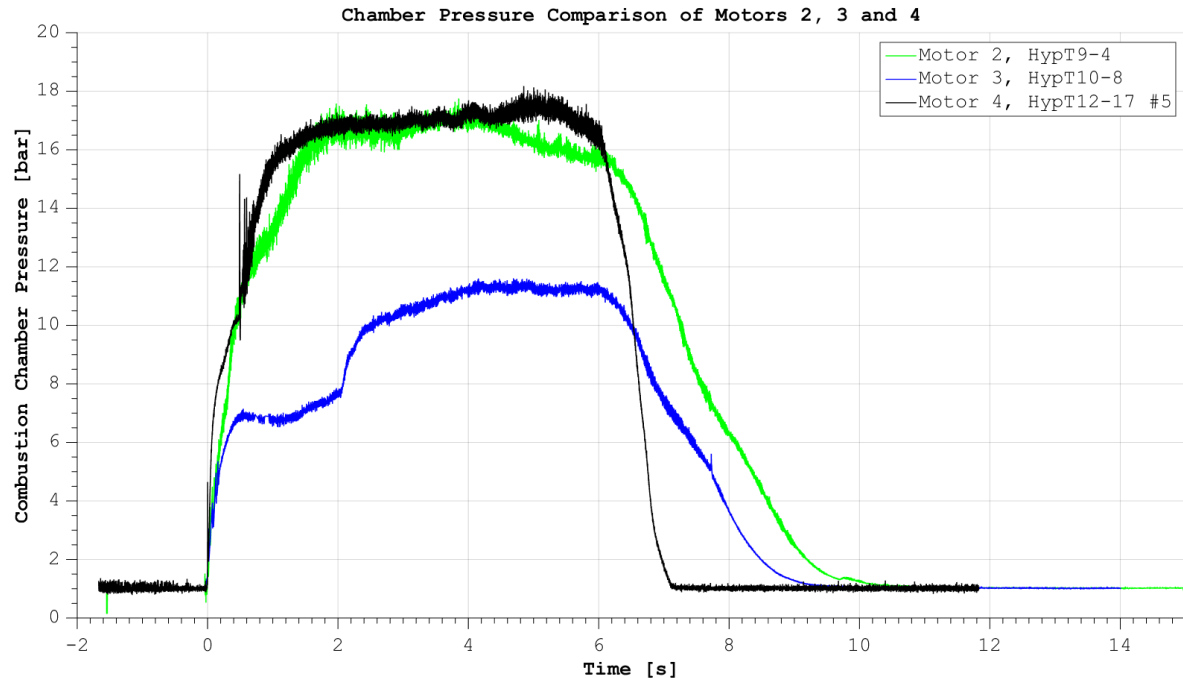


Figure 6.37: Chamber Pressure Comparison of Motors 2, 3 and 4 (HypT9-4, HypT10-8, HypT12-17-5)

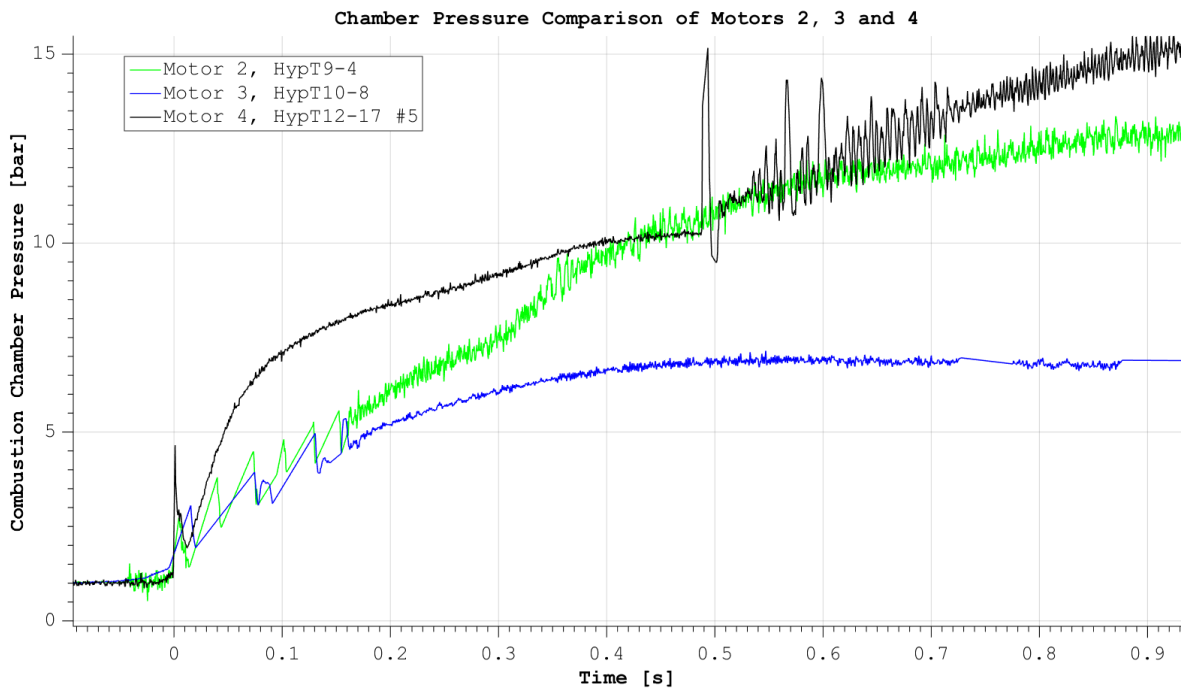


Figure 6.38: Chamber Pressure Comparison of Motors 2, 3 and 4 at Startup (HypT9-4, HypT10-8, HypT12-17-5)

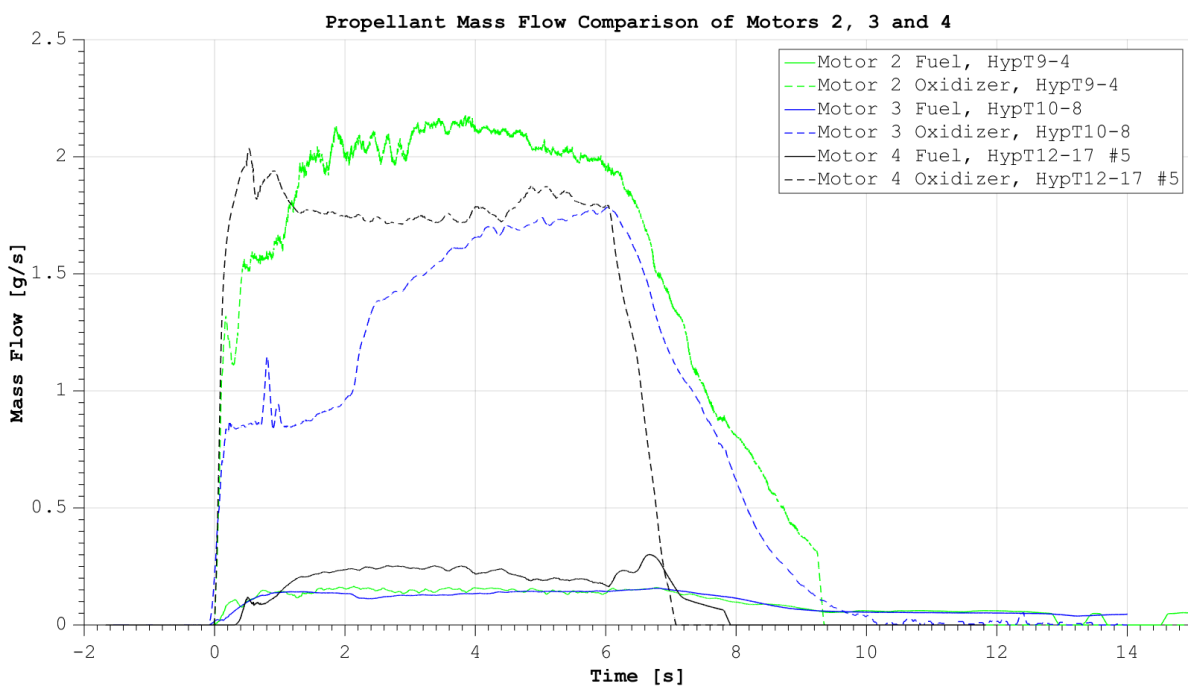


Figure 6.39: Propellant Mass Flow Comparison of Motors 2, 3 and 4 (HypT9-4, HypT10-8, HypT12-17-5)

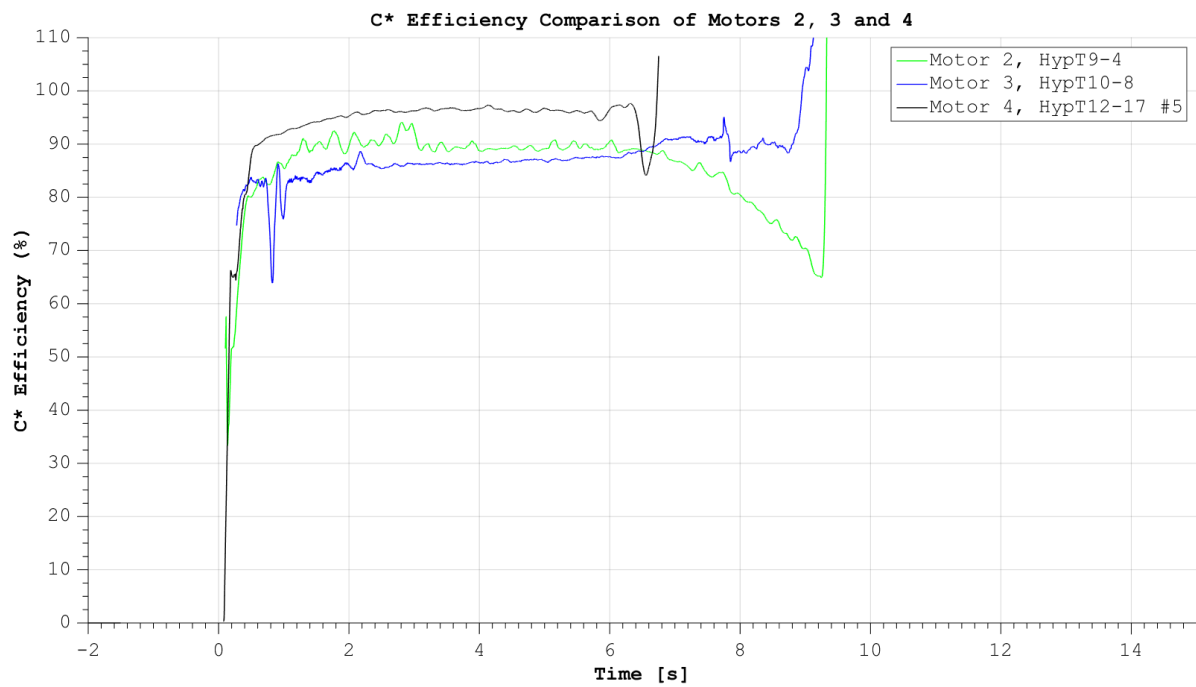


Figure 6.40: C* Efficiency Comparison of Motors 2, 3 and 4 (HypT9-4, HypT10-8, HypT12-17-5)

6.7. MINIMUM IMPULSE BIT ACHIEVED

The minimum impulse bit achieved has been calculated by truncating the stable section of the burn. This leaves only the startup and shutdown transients of the burn from which the total impulse is then determined. This was done for HypT12-17, burn #5 and is presented in Figure 6.41. It was found that the minimum impulse bit achieved was 6.4 Ns. The validity of the way the minimum impulse bit has been calculated is discussed in Section .

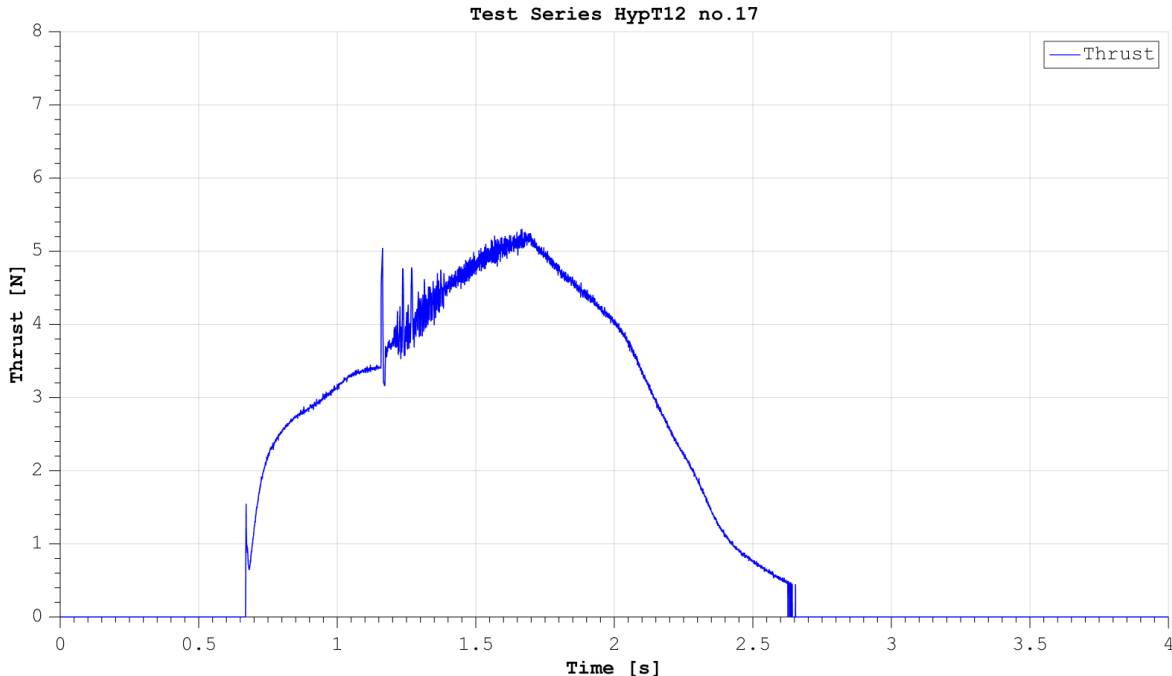


Figure 6.41: Minimum impulse bit achievable with Motor 4, as demonstrated in HypT12-17, burn 5.

6.8. SUMMARY

Table 6.4 contains data from motors 1 to 4 during tests HypT9-6, HypT10-8, HypT12-16 and HypT12-17-5. The combustion performance of motors 2 and 4 was found to be above 90% while motor 3 was measured to have lower performance, likely due to a manufacturing defect in the nozzle throat. None of the motors tested were able to operate at thermal equilibrium as intended, thus the maximum single burn time was limited to 30s. This was achieved with motor 4 which demonstrated the most effective regenerative cooling cycle of all motors. It was able to recover 380 out of 800 W of waste heat before the motor was shutdown to avoid overheating.

Motors 1 and 2 showed feedsystem coupled combustion instabilities at 140Hz while motor 4 , either during motor startup or during non-nominal operation but typically at 140 Hz except. Motors 2, 3 and 4 also displayed a higher frequency combustion oscillations.

The main conclusion of each motor are summarised in bullet pints below.

Motor 1

- Combustion inabilities at 140 Hz hindered motor startup due to low fuel injector pressure drop.
- The construction methods were inappropriate to achieve the tolerances required.
- The spark plug design was inadequate to provide consistent ignition.
- More performance parameters could not be evaluated as the motor could not be reliably started.

Motor 2

- Acceptable combustion performance (93%).
- The feedsystem coupled instability due to low oxidizer injector pressure drop.

- Inadequate burn times due to lack of cooling mechanism besides capacitive cooling.
- COTS spark plug verified to provide restart capability.
- Eventual motor failure due to overheating.

Motor 3

- Acceptable combustion performance (85%) although this value is suspected to be incorrect due to damage at the nozzle throat due to a manufacturing defect.
- Feedsystem coupled instability of motor 2 was solved by decreasing injector area, thus increasing the pressure drop across injector element.
- Combustion instability at 600 Hz, not feedsystem coupled. Exact source is unknown.
- N_2O could be used in a regenerative cooling cycle.
- Cooling cycle performance was inadequate to allow for long burn times. Maximum heat extracted was 240 W. Total heating not determined.
- Motor failed at the chamber wall of the cooling jacket due to overheating.

Motor 4

- Acceptable combustion performance (90-97%), despite a reduction in L^* from 4.1 to 1.3.
- Combustion instability at 220 Hz, not feedsystem coupled. Exact source is unknown.
- Cooling cycle redesign yielded much improved cooling performance over motor 3; 380 out of 800 W of heat was recovered at a peak motor operating temperature of 450 K at the nozzle surface.
- Cooling cycle performance was inadequate to allow for burn times longer than 30s.
- Motor failed at the fuel injector inlet due to overheating.

Table 6.4: Motors 2, 3 and 4 test summary. All data taken from tests HypT9-6, HypT10-8, HypT12-16 and HypT12-17-5

Configuration	Motor 1	Motor 2	Motor 3	Motor 4 (s)
Minimum impulse bit [Ns]	UD ¹	7.6	7.6	6.4
Impulse reproduce ability [%]	UD	UD	UD	+3.1 – 2.4%
Combustion instability frequency [Hz]	140 Hz	140 Hz & 600 Hz	600 Hz	16 Hz ² & 220 Hz
Combustion instability amplitude [bar, peak-to-peak]	2.5	0.5	0.4	0.5 - 0.9
Total number of starts [N/A]	1	5	18	20
Longest burn time achieved [s]	2	15	6	30
Total accumulated burn time [s]	2	31	52	125
C^* efficiency [%]	UD	93%	85% ³	90 - 96%
$Isp_{vac, \frac{A_e}{A_t}=100}^4$ [s]	Undetermined	288	262	285

6.9. ERRORS

C^* is determined indirectly by measuring the components that define it, as given in equation 6.1.

$$C^* = (P_c * m_{Total}) / A_{throat} \quad (6.1)$$

The error of C^* is therefore characterized by the sum the measurement error of each of the contributing components. The error associated with each of these components will be discussed here and where possible, quantified.

¹UD = Undetermined

²16 Hz combustion instability only occurred during cold starts. See Figure 6.28

³Unreliable data. See 6.3

⁴nozzle efficiency factor = 0.96

6.9.1. P_c MEASUREMENT ERROR

The pressure transducers used are quoted as having a linearity of 0.25% of full scale. For all tests a 20 bar sensor was used to measure P_c , with the exception of tests HYP12 4-17 where a 70 bar sensor was used. Each sensor is factor calibrated and comes with an individual calibration sheet. The maximum error associated with each sensor is in Table 6.5.

Table 6.5: Pressure measurement error summary

Transducer Full Scale [bar]	Full Scale Error	Absolute error [bar]	error when $P_C = 15$ bar
20	0.25%	0.05	0.33%
35	0.25%	0.0875	N/A
70	0.25%	0.175	1.17%

P_c is measured at 2mm downstream of the fuel injector, approximately 15mm from the nozzle convergent section. The internal ballistics model predicts a pressure difference of 0.00002 bar across these two positions, hence the error due to pressure drop in the chamber is considered minor.

The total error attributed to P_c measurement error is therefore taken to be $\pm 1.17\%$.

6.9.2. THROAT AREA

The throat area has physical effects contributing to errors, particularly machining tolerance, thermal expansion and boundary layer effects are identified as the predominant effects and will be discussed shortly.

The nozzle throat was drilled using a 1.5mm drill. From the book 'Metric Standards for Worldwide Manufacturing' [28] it is known that drilling generally falls into the tolerance grade IT10. IT10 specifies a tolerance of +0.04mm, -0.025mm. Hence, a 1.50mm drill may drill a hole up to 1.54mm in diameter. It is known that HSS drills can be up to 0.025mm undersize. These two effects result in an error in area and hence also C* of +5.4, -3.3 %.

Brass is known to expand by $18.7 * 10^{-6} \text{ m/mK}$, resulting in an increase in throat area as the motor heats. This effect is accounted for in tests HypT12 where surface mounted thermocouples are used at the nozzle exit plane. From this data, the heat adjusted throat area can be computed. See Equation 6.2. Note that it is assumed that the throat was manufactured at room temperature (298 K) and that the nozzle throat is the same temperature as the nozzle surface during motor operation.

$$A_{Throatadjusted} = A_t * (1 + 18.7 * 10^{-6} * (T_{NozzleSurface} - 298))^2 \quad (6.2)$$

The nozzle reached a peak temperature of 730K during HypT12-16. This would result in an increase in nozzle area of 1.6%. This increase in area is accounted in test series Hyp12 where surface temperature data is available hence no error is attributed to this effect. However, all other test series do not have surface temperature data and therefore an error of +1.6% is used.

The nozzle throat typically has a non-uniform velocity profile due to viscous effects at the wall, resulting in a slower local velocity. These effects are often grouped into a nozzle discharge coefficient [12]. This is taken from literature to be 0.995, resulting in a C* offset of -0.5%. This is accounted for in the calculation of C* and hence is not summed toward the total error.

The total error attributed to nozzle effects is therefore taken to be +5.4, -3.3 %.

6.9.3. MASS FLOW MEASUREMENT

The mass flow going into the motor is made up of oxidizer and fuel. These quantities are measured using subsonic isentropic flow relations as shown in Equation 3.5 and is repeated below for convenience.

$$\dot{m}_{fuel} = A_{Fuel\ Injector} * C_{djinj\ fuel} * \sqrt{\frac{2\gamma}{\gamma-1} * \rho_{fuel} * P_{Fuel\ Injector} * \left(\frac{P_{Chamber}}{P_{Fuel\ Injector}} \right)^{2/\gamma} - \left(\frac{P_{Chamber}}{P_{Fuel\ Injector}} \right)^{\frac{\gamma+1}{\gamma}}} \quad (6.3)$$

Table 6.6: C* error summary

Error source	C* efficiency error [%]
P_C Measurement	± 1.17
Throat area	+5.4, -3.3
Mass Flow measurement	+4.99, -6.09
Total	+11.56, -10.56

Each parameter in Equation 6.3 contributes to error which is discussed here. Two pressure transducers are used to determine the pressure differential between the upstream injector pressure and the combustion chamber. It has been shown that all sensor class types (20, 35 and 70 bar) show a relative accuracy of 0.1 bar or less up to 15 bar. The typical pressure drop is taken to be 1 bar for both fuel and oxidizer, yielding a error in pressure differential of 10%. According to 6.3, the mass flow is related to the square root of the pressure differential. Hence a 10% error in pressure differential results in an error of 4.9% in mass flow ($\pm \sqrt{1.1} = 1.049$).

For an error then of 0.2 bar on a pressure differential measurement about 15 bar, the maximum error can be found as in Equation 6.4.

$$\text{error}_{\dot{m}, \text{pressure errors}} = \sqrt{1 + 0.2/15} - 1 * 100 = 0.66\% \quad (6.4)$$

Additionally, an incorrect pressure measurement can occur due to an incorrect position of the pressure tap. Fluid models of the system show that flow velocities in both feed lines and combustion chamber are low, or the pressure tap so close to the ideal position that these effects can be neglected.

Fluid density is also required to determine the mass flow. The density is determined using pressure and temperature measurements along with isentropic relations. The temperature is measured using a thermocouple. The thermocouple has a finite thermal mass and hence has some response delay, especially when the thermal mass of the fluid flow is small as is the case with the fuel flow. Although it is recognized that this effect is present, it cannot be sufficiently quantified. It is also noted that system transients appear relatively slow, hence it can be assumed the thermocouple lag effect is minor and hence can be ignored.

The injector ports are manufactured in much the same way as the nozzle throat is and therefore also possess similar error values of +5.4, -3.3 % for both fuel and oxidizer mass flow. As C* is inversely proportional to mass flow, the error on C* attribute to orifice area error is +3.3, -5.4 %.

The error in fuel and oxidizer mass flow results in a possible O/F error of ± 17.8 % although it is likely that both oxidizer and fuel both have an error in the same direction since they are both produced in a similar manner, resulting in a far lower error in O/F ratio. An uncertainty in the operating O/F does lead to a miscalculation of C* however the extent of this effect is highly dependent on the operating point. For this reason, this effect is not considered.

The total error on C* attributed to mass flow errors is therefore +4.99, -6.09%.

6.9.4. ERRORS SUMMARY

The errors of measuring C* are summed in this section. It would appear that the largest contributors are errors in measuring mass flow into the motor and evaluation of the nozzle throat area.

7

DISCUSSION

Many interesting phenomenon were encountered in testing of the 4 motors. A number of these tests have been presented in detail in Section 6. This section will discuss these phenomenon in detail and discuss possible causes. Furthermore, this section will discuss the agreement of the numerical models presented in Section 4. Lastly, the motor test results and how well they satisfied the design requirements will be discussed.

7.1. FEEDSYSTEM RELATED EFFECTS

The feedsystem used in this setup was the design subject of an MSc thesis by T. Knop, also of Hyperion Technologies. Hence, its design and motivation has not been presented in this thesis. For further information on the exact design of the feedsystem refer to the work of T. Knop [26]. Nonetheless, the feedsystem has a profound influence on the performance of the motor. In all test series, with the exception of HypT12, the feedsystem displayed an oxidizer flow lag of approximately 2.5s whereby the flow rate would only be approximately 60% of the design mass flow. In motor 2 it can be seen that the low oxidizer mass flow has lead to a lower than expected pressure drop over the injector and hence an instability has developed which can also be seen in the oxidizer feedsystem. According to literature [9], feedsystem coupled instabilities often occur at frequencies between 10 and 400 which can be observed in chamber pressure data as well as in feedsystem pressure. A common method to alleviate such instabilities is to increase the pressure drop over the injector element. This was done in motor 3, whereby the injector area was reduced by 40%, leading to an injector pressure drop increase of 1.1 bar from 0.4 to 1.5 bar, as shown in HypT9-6 vs HypT10-8 as presented in Section 6. Note that motor 3 also included a regenerative cooling cycle, resulting in the oxidizer being injected at a much higher temperature compared to that of motor 2, further contributing to the increase pressure drop over the oxidizer injector element.

While the increase oxidizer pressure drop seems to have completely eliminated all instability at 140 Hz, it has served to significantly increase the instability at 600 Hz. It is possible that the 600 Hz instability is related to this increase in injector pressure drop and hence injection velocity. Sutton[9] cites frequency oscillation between 400-1000 Hz as possibly due to flow eddies, or resonance in the propellant feedsystem as possible causes for such oscillations. The exact mechanism which causes the observed high frequency instability is yet unknown. It is interesting to note an instability of 220Hz appears on motor 4 although it is much weaker than that seen in motor 3.

Motors 3 has a chamber volume three times larger than motor 4 and also displays a instability at approximately three times that of motor 4, suggesting a geometric relation. While there is no causality link, it should be investigated if this is due to a known phenomenon.

The feedsystem used for HypT10-6 suffered from long shutdown transients, especially on the fuel feed line where liquid fuel would become trapped between the valve and mass flow limiting orifice which would take up to 10s to exit the system. While this was not an issue for motor operation as it occurs at the end of the test, it does make any analysis of the minimum impulse bit of the motor somewhat useless, at least until a more flight-like feedsystem is implemented. Nonetheless, an attempt to quantify the minimum impulse bit was made to allow the level of performance to be determined. The result shows that the current feed system

is completely unsuited to providing small impulse bits.

An attempt to reduce the feedsystem volume was made in HypT12, where the valves and mass flow limiting orifices were mounted as close to the motor as possible. It was expected that this would reduce the startup and shutdown transients significantly. Instead, as observed in HypT12, (see Figure 6.22) the massflow during the startup phase exceeded the design value by 25% before stabilizing. The increase in the oxidizer mass flow would lead to an unexpectedly low pressure drop over the fuel injector due to the higher operating pressure of the motor, possibly leading to a low frequency fuel feedsystem coupled instability observed in the startup phase of burn HypT12-16. This instability does not appear to be present when the motor temperature is above 500 K. Hence a 'warm up period' was required to achieve startup behaviour with a minimum of instabilities. In HypT12-17 this was achieved with relative success. It is likely that the elevated motor temperature at startup preheats the propellants, increasing the pressure drop over the injector element enough such that instabilities do not occur. This is particularly true for the fuel injector where low pressure drop has lead to combustion products going backwards up the fuel injector at motor startup as is visible in 6.30. This phenomenon is explained in detail below.

At the beginning of HypT12-16, in Figure 6.23, the temperatures in both fluid inlets can be seen to increase by 70 k. The rise in fuel inlet temperature can be explained by hot combustion gasses flowing backwards up the feedsystem due to instabilities. Figure 6.20 shows that the chamber pressure does exceed the feed pressure of the fuel but not the oxidizer. The oxidizer feed pressure is somewhat higher than the fuel pressure, however it is likely that the chamber pressure also exceeds the oxidizer feed pressure but the peak of the pressure spikes cannot reliably be measured with a sampling rate of 2000 Hz as used due to the fast decay rate of the pressure spike.

In HypT9-4, motor 2 shows fast startup characteristics. However, in later tests such as HypT9-6, a '2 phase' startup was observed. In both cases, the chamber pressure closely follows the shape of the oxidizer mass flow rate. Similar observations have been made for motor 3 in HypT10-8. It is likely that the startup transient of any motor is heavily dictated by the performance of the feedsystem. The system did not allow for the operator to assess whether the system was effectively primed or not, and hence it is possible that there was no liquid flow through the choaking orifice in the feedsystem, leading to lower than designed mass flow. This effect would be alleviated once all vapour had been bled out of the system up to the main valve, hence minimising the amount of vapour in the downstream feedsystem.

In HypT12-17 it can still be seen that the fuel temperature upstream of the injector increases beyond levels consistent with expanding ethane, as seen in cold flow testing. This suggests that gasses from the still hot combustion chamber, although uncombusted, are travelling upstream. This theory is likely, as it is apparent at startup in this test, that the pressure in the chamber is higher than in the fuel feedline. This effect would result in no fuel reaching the chamber until such time that the fuel feed pressure exceeds $P_{Chamber}$. From Figure 6.27 it can be seen that this occurs at 0.5s after motor startup and induces a large pressure spike. This pressure spike occurs because the propellants in the combustion chamber are not able to combust due to the presence of fuel, resulting in a sort of hard start.

It appears that all issues with startup transients are related directly to the massflow and volumes of the feedsystem in that the mass flow provided is insufficient to fill the downstream feedsystem at a sufficient rate such that the motor receives both oxidizer and fuel at the correct ratio and at the same time. It is likely that because the feedsystem volumes downstream of the valves are of equal volume for both fuel and oxidizer, the oxidizer fills up much faster than the fuel does due to the unequal O/F ratio. This results in the motor inadvertently leading with oxidizer and hence not having any fuel to ignite. This results in non-ignition until fuel has filled the feedsystem and begins to flow into the motor. In all cases, this has only occurred when the motor was already at significant pressure due to the coldflow of oxidizer. Once the fuel does ignite, the chamber experiences a strong increase in pressure, similar to a hard start in liquid motor, except much less severe due to the limited mass of propellant which can be stored in the chamber as a gas. If there is insufficient pressure drop over either the fuel and oxidizer injector, the motor enters a feedsystem coupled instability, typically at 140 Hz as observed in HypT7-10, HypT9-6 or 16 Hz in HypT12-16. These tests all displayed oscillations in both the combustion chamber and at least one of the injector feeds due to this effect. This phenomenon occurs regardless of the feedsystem volume however it appears the feedsystem upstream volume alters the frequency of the oscillation.

7.2. IGNITION CHARACTERISTICS

As presented in Section 6, motor 1 experienced troubles with ignition, particularly in HypT6 and 7. It was later discovered that a faulty check valve allowed oxidizer to flow in place of fuel, resulting in fuel starvation and hence no ignition. It was also found that the more powerful spark generator used in HypT7 caused electrical breakdown of the insulator material and hence no spark in the chamber. It is likely that this also occurred during motor operation when chamber pressures increase due to cold flow, hence increasing the dielectric strength of the chamber gasses and causing the spark voltage to increase and the electrode insulation to break down. HypT8 showed that a more effective spark insulation would also result in more consistent ignition characteristics. However, combustion instabilities stopped the motor achieving sustained combustion. It was concluded that the construction method selected for the motor required machining tolerances in excess of what was achievable in a non-specialized machine shop. This resulted in poorly defined fuel injector ports and hence very little pressure drop over the fuel injector, measured to be in the order of 0.03 bar. Note that this is less than the quoted accuracy of the pressure sensors and hence it this measurement cannot be relied on. In HypT8, the chamber pressure sensor failed in burn 1, so no chamber pressure was obtained. This however could be estimated as the fuel feed pressure due to the known very low pressure drop over the fuel injector.

From HypT9 and onward, a COTS spark plug was used to great effect. In HypT9-2, the spark plug suffered damage to the tip was subsequently repaired. All spark plugs installed hereafter had the tip removed before installation. A single new spark plug was used in each of the test series HypT10 and 12 with no damage to the spark plug. There were no further issues with the spark plug performance. It is anticipated that these spark plugs may encounter issues if too much soot builds up on them. A great deal of soot has been observed on the current spark plugs after multiple burns have been performed, however it does not seem to effect the ignition characteristics. One COTS spark plug was damaged due to over temperature in HypT9-6. This spark plug was located near the nozzle of the motor where it was observed to discolour due to heating. While no direct temperature measurement was taken, it is known that brass changes colour as was observed at around the melting temperature of silver solder, around 900 K.

7.3. NOISE DUE TO SPARK IGNITER

It could also be observed that the spark plug generated very significant noise. In Figure 6.1 it can be seen that the spark igniter is started at 37s, where significant noise begins to occur. The noise becomes more prominent as the chamber pressure begins to rise due to an increase in the spark voltage. The noise then suddenly decreases when the chamber pressure rises above 4 bar due to the spark voltage increasing high enough such that the electrode insulation breaks down and a short spark is formed, resulting in little noise. The large spark returns once the chamber pressure pressure lowers below 4 bar.

In tests HypT10 and 12, a smaller spark generator was once again used as in HypT6, however with a commercial spark plug. This reduced the noise from 0.5 bar peak-to-peak to a level which was no longer measurable.

7.4. MOTOR EFFICIENCY

The motor efficiency could be evaluated for motors 2, 3 and 4. Motors 2 and 3 were effectively identical except that motor 3 included a regenerative cooling cycle. Although this change should increase the combustion efficiency of the motor as heat is recovered, the measured efficiency of motor 3 was much lower than that of motor 2. This is likely due to the throat damage motor 3 incurred during production, making this efficiency measurement void. Motor 4 measured a very similar efficiency to motor 2 (92-93%), despite featuring a L^* of one third of that of motor 2. This could in part be attributed to the regenerative cooling cycle. Although it was measured that even at peak heat recovery only 380 watts of heat was recovered. This would amount to an increase in C^* efficiency of less than 0.7%. Consequently it can be concluded that the direct energy contribution of the regenerative cooling cycle to the motor efficiency is very small. The increased efficiency of motor 4 could however be explained by the higher oxidizer injection velocity and with it increase injector performance. Alternatively, the regenerative cycle substantially heated the oxidizer and thus brought it closer to its decomposition temperature, promoting combustion in the chamber and thereby increasing combustion efficiency. These effects however must be small as there is no great increase in motor efficiency as the

cooling fluid increases in temperature from 300K at the start of a burn to over 700K by the end. See Figure 6.23. An increase in temperature to this extent would correspond to an increase in oxidizer injection velocity of more than a factor of 2.

It can be concluded that the design L^* of motor 4 is likely still significantly higher than required to achieve good combustion performance with the given injector design. Literature [25] specifies a design L^* value of 0.5 to 0.8, a reduction by 40 to 60% for similar injection styles. This would also substantially reduce the total heat flux to the motor, reducing its equilibrium temperature.

The motor efficiency measurement has a large error associated with it, as shown in Table 6.6. These errors were predominantly due to the inaccuracy in determining the areas of both the throat and injector orifices. An error in the injector area as well as the pressure differential measured across the injector results in a mass flow measurement error. The majority of these can both be traced back to machining errors. This shows that the evaluation in the motor performance is significantly hindered by the small size of the test article.

The mass flow measurement was made based on single phase gaseous flow only. While pressure and temperature measurements close to the injector elements suggest that the fluid was sufficiently far away from their saturated vapour state and hence all liquid droplets should have evaporated, it was not possible to experimentally determine if this assumption was valid. It was however observed that increasing the length of feedsystem between the orifice and the injector, and hence increasing the vaporization time, did not yield different injector performance, suggesting that the original assumption is indeed valid.

Subsonic flow relations (equation 3.5) were used to calculate the mass flow. It was observed that the pressure ratio across the injector did exceed 2 during motor startup and shutdown, indicating that supersonic flow in the injector may have occurred and hence the relation become invalid for a limited period of time. These effects may have contributed to inaccurate mass flow measurements at the startup and shutdown transients when the injector inlet pressure far exceeds the chamber pressure. While this error was known, it was not corrected because the motor efficiency was not of interest during these transients.

7.5. REGENERATIVE CYCLE

Regenerative cooling was used to limited effect on motors 3 and 4. The intent was to achieve a motor which would be able to operate at thermal equilibrium.

Figure 6.24 shows the heating of the motor. It can be observed that the heating power is at first negative, indicating that the outside of the motor actually begins to cool. This is likely because cooling fluid starts to flow at the moment of motor startup, cooling the chamber. Combustion and hence heating of the chamber occurs very soon after, within a few tenths of a second. This transient appears significantly faster than the slow transient observed in Figure 6.24 and hence cannot fully account for the early cooling. It is likely that because chamber surface temperatures are measured on the outside of the motor, the heat which originates at the centre of the motor takes some time to propagate through the chamber wall where it reaches the thermocouple, resulting in a lag in the measurement of several seconds. This effect also exists however less so, for the regenerative cooling as it is located much closer to the motor outer surface. The transient error arises as the method for calculating heat flux assumes that the motor temperature is homogeneous and infinity conductive.

7.6. COMPARISON TO MODELS

7.6.1. ANALYTICAL MODEL

The analytical model used was very simple in design and hence was subject to many deficiencies. The designer was aware of this and chose not to improve the model due to time constraints. The deficiencies will be discussed here.

The inner wall temperatures, particularly at throat, appear to not be well modelled. It is likely the main contributor to this effect is the fact that the model uses 1D heat transfer in the wall. This results in under predicting the material's ability to sink heat away from the wall and hence the wall temperature is over predicted. The analytical model predicted that brass would not have sufficient conductivity to resist melting at the throat. It was however found that it successfully used without any damage in tests of up to 30s. This could

also be in part due to inaccuracies in the predicted heat transfer rate.

Total heating was over predicted by roughly 20% in the analytical model despite radiation, conduction and locally high velocities due to swirl injection being neglected. These inaccuracies show that this style of model, based on standard convective heat transfer equations, does not yield a result sufficient to do detailed design of a motor however it is useful for obtaining a first order answer which can be useful early in the design process, at little cost. Now that more complex tools are available such as numerical models, it may be worth revisiting the design decisions made based on the analytical model, such as the selected contraction ratio of 100.

7.6.2. NUMERICAL MODEL

As described in Section 4, the numerical model was developed in two stages. Firstly, the injector model and combustion was evaluated. While this first stage was very useful for visualising the flow pattern, it is impossible to verify experimentally with the available setup and hence no conclusions can be drawn as to the accuracy of the model. The combustion efficiency can be used as a gauge of model accuracy, however the experimental error of combustion efficiency was found to be in the order of $\pm 11\%$, so high that any correlation between the model and test data could be merely coincidental. Furthermore, too few data points exist to do any useful statistical analysis.

Secondly, the regenerative cooling cycles and heat transfer model was added to the injector and combustion model. The operating temperatures of the motor have been evaluated both numerically and experimentally for motor 4 and a comparison can be made. An important note however is that all modelling is done at thermal equilibrium while this was never achieved in testing, hence all experimental results are of a system still within a thermal transient.

As shown in Section 4 the numerical model predicted that the total heat flux to the combustion chamber walls due to combustion would be 800 watts. This was measured to be between 750 and 900 watts. Some discrepancy in this measurement may be due to the experimental motor being wrapped in aluminium foil to attach the surface mounted thermocouples which would have served to insulate the motor, inhibiting its ability to radiate to ambient, although it is unknown to what extent this would have had an effect. Furthermore, the surface mounted thermocouples are only attached through pressure applied by the aluminium tape. This lead to erratic measurements, particularly on the 'regen exit' surface measurement. For this reason, the regen exit surface measurement was not used in the calculation of total heat flux.

A simulation was performed to mimic the motor input conditions of HypT12-16 as closely as possible. Actual propellant flow rates, temperatures and mixture ratios were used in the numerical model. The output of the model and experimental data can then be compared to assess the model accuracy. This is done in Table 7.1. From this table, it can be seen that there are some differences between the predicted model values and the experimentally determined values. While the total heat flux is well predicted by the model, it seems other temperature data, in particular the cooling effectiveness of the regenerative cycle was over predicted. The pressure drops over particular parts of the feedsystem show some degree of inaccuracy. Interesting to note is that components with larger general geometry, such as the regenerative cooling cycle and oxidizer inlet also display much better accuracy in the pressure drop prediction. Smaller geometry, such as the fuel inlet, which is only 30% of the diameter of the oxidizer port (0.3 vs 1mm), also displays an inaccuracy twice as large. This is likely due to production inaccuracies leading to imprecise geometry and hence inlet areas, or in poor evaluation of boundary layers in the numerical model, or both. Note that from 6.9 it was stated that machining holes are typically oversized. The model uses exact hole geometry. This would lead to an inaccuracy whereby the pressure drop over a given element is over-predicted by the model, as is observed here.

From the results presented and the comments made, it should be clear to the reader that the numerical model developed was primarily used as an engineering tool. There was not sufficient time available to conduct a rigorous scientific study in order to find a global optimum nor to investigate all interesting parameters. The direction studied and changes made to models were based largely on studies of systems which have similar components or design features. Consequently the solutions and optimizations performed were local optimizations. More time and rigour is needed to use this numerical tool to its fullest extent. The limited accuracy found between the numerical model and experimental results are indicative of this conclusion.

Table 7.1: A comparison of experimentally and numerically determined parameters for Motor 4 during HypT12-16

Parameter	Numerical model	Experimental data (HypT12-16)	% difference
Total heating power of combustion [W]	800	750 to 900	-7 to +13%
Cooling power regen system [W]	655	370 ¹	-45%
Δ T Cooling fluid to wall at regen exit [K]	45	119	+160%
Peak Temperature of thermal equilibrium [K]	930	N/A ²	N/A
Δ P injector Ox [Bar]	2.6	2.1	-20%
Δ P injector fuel [Bar]	0.59	0.36	-39%
Δ P Regen cooling system [Bar]	3.15	2.8	-11%
C* efficiency [%]	101%	93%	-8%

None-the-less, the numerical model was essential in providing the designer with a basic understanding of the flow structures formed by a given injector geometry. It allowed many different configurations to be tested at very little cost. Later in the design process, the model was very useful, particularly in the thermal design of the motor where results were found to be in much better agreement with experimentation.

7.7. TEST REPEATABILITY

HypT12-17 burns 3, 4 and 5 have been presented in Section 6.5 where it was shown that for this set of tests, total impulse repeatability was within +3.1 -2.4% of the average, despite the fact that burn 3 suffered from a 1s period of strong combustion instabilities at startup. Burn 3 was also the lowest performing of the burns, both in terms of total impulse and C* efficiency, likely due to the observed instability.

Many other motor tests observed very erratic mass flow behaviour, leading to highly varied performance. This was avoided in these tests by ensuring the motor was pre-warmed and the feedsystem primed with liquid fuel and oxidizer. HypT12-17 burns 3, 4 and 5 show that if these parameters could be controlled, motor 4 could produce thrust profile repeatability within the specification of ±10%.

The burns were performed in quick succession such that the motor did not have sufficient time to cool back down to the initial temperature of the first burn. Hence, the initial motor surface temperature increased with each successive burn. This could explain the different startup transients observed and the lack of combustion instabilities observed in burns 4 and 5. The starting motor temperature should be more tightly controlled to achieve more consistent motor behaviour.

7.8. EVALUATION OF REQUIREMENTS

In Section 2.2 the thruster requirements were deduced from the top level system requirements. Here, they are repeated and discussed individually in light of the test results presented in Section 6. Motor 4, being the most advanced motor presented, will be used as a focus for this comparison. Comments on how the requirements were satisfied are included below each requirement.

1. The system shall have a thrust rating of 4 +/- 0.5N.

Motor 4 showed a peak thrust of 5 N during HypT12-16. This is slightly higher than anticipated as the motor efficiency is also better than first anticipated. This can easily be adjusted in future iterations as the designer requires.

2. The system shall have a minimum impulse bit of 1Ns.

The minimum impulse bit actually achieved was in the order of 30 Ns. No testing was conducted to investigate this parameter specifically. However, from 3s burn tests, one can calculate the total impulse in the startup and shutdown transients. This impulse was found to be at least 6.4 Ns. This result is so high, largely due to the oversized experimental feedsystem used in the test setup. This meant that both startup and shutdown transients are very long, in the order of seconds, leading to a large minimum impulse bit. It is anticipated that this will be corrected once a more flight representative feedsystem is implemented.

3. The system shall have an impulse bit repeatability of better than 10%.

In HypT12-17, burns 3, 4 and 5, using motor 4, an impulse repeatability of +3.1 -2.4% was demonstrated for burns of a total impulse of 35 Ns. This is well within the specified requirement.

4. The system shall have an Isp vac in excess of 230 s.

Section 6 showed that motor 4 has an I_{sp} of 285s for an expansion ratio of 100 in vacuum. The error on this measurement was determined to be maximum - 10.56%. Hence, an I_{sp} of at least 255 has been demonstrated.

5. The system shall have a maximum single burn time in excess of 100s.

The longest achieved burn time of any motor was HypT12-16 where the motor burnt for 30s before being shutdown due to fear of over-heating. Figure 6.23 shows that the motor is still far away from operating at thermal equilibrium. This is further supported by Figure 6.24 where it can be seen that the regenerative cooling only accounts for approximately half of the total heat dissipated by the end of the burn. If the motor is to operate in vacuum, this fraction will likely have to increase substantially, even if the nozzle extension is to be radiatively cooled, something which may be difficult to achieve in a highly integrated CubeSat design. It is likely that higher temperature materials, a smaller chamber (lower volume and hence lower chamber wall surface area) and/or the use of other cooling methods (film cooling, transpiration cooling etc) may need to be used to achieve a 100s burn time as required.

6. The system shall have a total burn lifetime in excess of 1000s.

No degradation of motor internal parts was measured. Hence, there is no reason to believe that parts may fail before 1000s of operation. Components external to the motor however, such as feed lines, were subjected to intense vibrations during unstable motor starts. This probably contributed to the failure of the pressure sensor port on motor 2 and the fuel inlet port on motor 4. The pressure sensor of motor 4 also showed a tendency to gain an offset during operation. Whether this effect was brought on by heat or shock loading during unstable motor operation is unknown. Lastly, the spark plug was observed to gather a large amount of soot during operation. If this continues to build, it may lead to a short circuit on the spark plug, leading to malfunction.

It must be verified that the above-mentioned components can indeed withstand 1000s of motor operation to meet this requirement.

7. The system shall be restartable in excess of 1000 times.

Motor 4 was started successfully a total of 20 times with no visible degradation to the spark plug after blackening during the first burn. No degradation to the motor itself was observed as long as the motor was kept within temperature limits. For this reason, it is believed that 1000 starts may be possible with the current design. Factors such as soot built up on the spark plug may eventually become an issue as previously mentioned.

8. The system shall have thrust vector capability of +/- TBD degrees.

This capability was not investigated due to time constraints and hence is not elaborated on.

9. The system shall not cause adjacent components to become hot to the extent that they cannot reasonably function.

This requirement was not evaluated beyond quantifying the heat generated by the motor. It was found to be in the order of 800 watts for motor 4. Much of this heat can be recovered by a regenerative cooling cycle. Up to 400 W was achieved in tests. Numerical analysis predicts that the surface temperature of the motor operating at thermal equilibrium will be 900K. This will result in a total radiated heat of 133 W. It is yet unknown if this will have an adverse affect on adjacent components as the integrated system has not yet been designed. 133 W is a very substantial heat load for a 6U CubeSat and must be considered in the thermal design.

10. The system shall fit inside a 2U CubeSat slot.

While this criteria was not evaluated directly, it was taken into consideration when selecting the form factor of the motor in that the motor was kept as short and stubby as possible. Motor 4 is 50 x 24 mm in size and hence fits inside a single unit of a CubeSat. Many other components are required for the thruster system such as valving, tanks, control electronics etc. These components have not yet been sized and so no judgement can be made as to whether the system really does fit inside a 2U CubeSat.

11. The system shall be compatible with an ISIS, Clydespace and Pumpkin 6U CubeSat layout.

As with Requirement 10, this cannot be elaborated on as no proposal was made to integrate the thruster and associated componenrty into the CubeSat format.

12. The system shall be manufacturable.

The system was machined by the author using non-specialized TU Delft equipment. Hence the system is easily manufacturable by a professional. The manufacturing techniques used however do not necessarily suit a design where the system is highly integrated into a CubeSat format. Other manufacturing techniques such as additive manufacturing should be considered to allow for the required level of system integration.

13. The system shall be a working prototype by the 31st of August 2015.

The first successful prototype (motor 2) was fired on 25.08.2015 and the last, (motor 4) was fired on 20.09.2015 hence this requirement was satisfied.

8

APPLICATION TO CUBESETS

Much is now known about the basic working of a bi-propellant CubeSat thruster system. These lessons can be taken from a component level to a system level, where the interaction between the thruster and the rest of the CubeSat can be looked at in more detail.

8.1. THRUST AND VIBRATIONAL LOADING

It has been found in Section 6 that the motor produces a thrust of approximately 4N. For a satellite of 8 kg, this results in an acceleration of $0.5 \frac{m}{s^2}$. While this is not a large acceleration, especially compared to launcher loads which can be up to $60 \frac{m}{s^2}$, some components may be particularly sensitive to acceleration while in operation, such as reaction wheels, solar panels or antennas.

Section 6 also showed that in some instances, such as motor startup, strong low frequency instabilities can occur. These were typically between 100 and 150 Hz and were measured to have a peak-to-peak value as high as 2N, although the actual value could be higher as not all pressure peaks could be resolved due to the nature of the measurement system.

Another instability of 600 Hz and 200 Hz was found on motors 3 and 4 respectively. In motor 4, the peak to peak amplitude was measured to be 0.3N.

Although it is recognised that a motor which is prone to instabilities should not be flown on a satellite, these vibrational modes must be considered. If the thruster incurs some component failure leading to combustion instabilities, such as a partially blocked feedsystem component, the resulting vibrational loads cannot be allowed to cause other satellite components to fail.

8.2. THRUST VECTOR MISALIGNMENT

The proposed [ADCS](#) would use the 4 N motor as main propulsion. Contrary to larger satellites where a reaction control system ([RCS](#)) is used to counter adverse torques, the proposed system would rely on reaction wheels only. The proposed reaction wheels have a maximum actuation torque of 2mNm and a total storage of 60mNms. It is known that the thruster has a thrust of 4N, and so the maximum allowable thrust offset can be calculated with equation 8.1 where the sum of moments on the spacecraft must equal zero.

$$d_{\text{thrust offset}} = \frac{\tau_{\text{max reaction wheels}}}{F} = \frac{0.002}{4} = 5 * 10^{-4} m = 0.5mm \quad (8.1)$$

From equation 8.1, a maximum allowable thrust misalignment of 0.5 mm is found. It is likely that this is not possible for two reasons. Firstly, CubeSats are designed such that components are 'Plug and Play'. If the installation of the thruster requires the centre of gravity to be located within 0.5mm of the thrusting vector, the number of configurations possible to the designer is reduced hugely, possibly eliminating all design options. A misaligned centre of gravity can be corrected for using carefully placed dead mass, however this will not solve the second problem.

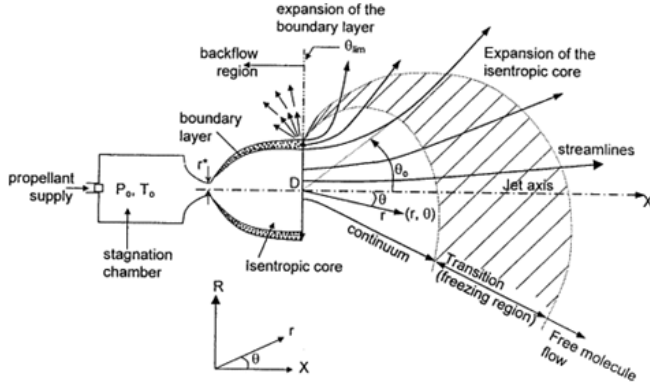


Figure 8.1: Plume characteristics in the space environment [29]

As the thruster fires, it consumes propellant and hence changes the centre of gravity of the satellite, unless the tanks are both placed precisely on the thrust vector. This of course neglects any sloshing or other dynamic effects. If this leads to a change in centre of mass by more than 0.5mm, the reaction wheels will not be able to effectively stabilize the satellite during motor operation.

In the best case scenario, even if the thrust vector offset requirement of 0.5mm was satisfied, the reaction wheel would be saturated within 30s if operating at maximum torque. This would mean that a 100s maximum burn time required by the thruster design would not be practically possible on the satellite.

For the above mentioned reasons, it is likely necessary to include some sort of thrust vectoring system to minimise thrust offset and thus adverse torques.

The thruster incorporates swirl injection of both the oxidizer and fuel. This could result in an adverse torque if the swirl does not dissipate inside the chamber. Numerical models suggest that the total torque produced is < 2mNm and thus this torque should be adequately managed by reaction wheels.

8.3. THRUSTER PLUME EFFECTS

A thruster operating on a low earth orbit (LEO) satellite in space expels a gas plume in order to create a reaction force. The gas plume can cause undesirable effects on the spacecraft surfaces such as disturbance force/torque, thermal loads, and contamination of sensitive components and sensors [29].

The plume from a thruster in space can exhibit a back flow region as shown by Figure 8.1. In a CubeSat, volume is very restricted and hence components are typically packed very tightly together. This could result in the flow back intersecting satellite components. According to Ho Lee[29], this effect causes negligible adverse torque and heating as the density and velocity of the backflow subside drastically in the vacuum of space. The backflow does however deposit significant quantities of exhaust products. This may be an issue depending on the satellite, for example if optics such as cameras or sun sensors are located near the thruster and if there are harmful chemical species in the exhaust plume.

Current in-space propulsion uses Hydrazine mono-propellant thrusters. The exhaust from the decomposition of hydrazine contains a large fraction of condensable fluids such as ammonia. This can be deposited on the structure, particularly solar panels, causing a significant reduction in performance [30]. The propellants used in this study, N_2O and C_2H_6 produce nitrogen, water, carbon dioxide and small amounts of oxygen as combustion products as stated in 4.1. Water could potentially also condense on satellite surfaces. Depending on what surface this is, it could have adverse effects such as creating a short circuit on a PCB. Oxygen has a strong oxidizing capability and could corrode satellite components.

Figure 8.2 shows the mass flux of the plume as a function of angle from the central axis of the thruster from a 10N MON-1/MMH thruster designed by MBB (Messerschmitt-Bölkow-Blohm). It shows that outside of +/- 20 degrees of the axis of the thruster, there is very little flow from the nozzle exhaust. From this data, it is apparent that it is advisable to ensure that no structure is within this angle to minimize interaction between the thruster plume and the satellite. A larger angle can be taken to ensure a conservative approach is taken.

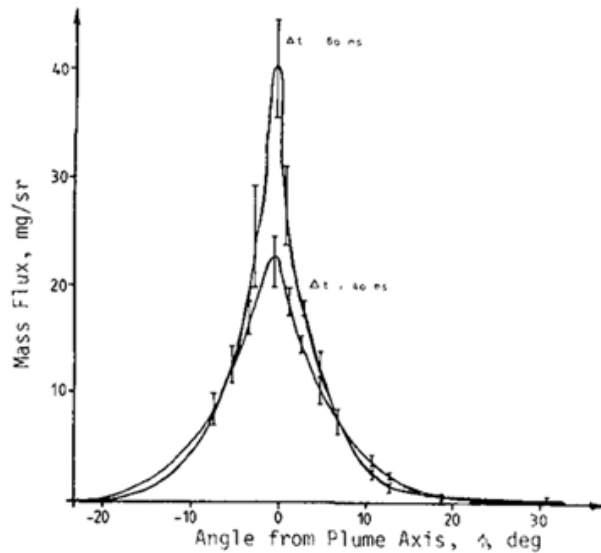


Figure 8.2: Angle of plume from centre axis for a 10N MON-1/MMH thruster [31]

8.4. THRUSTER OPTIMIZATION FOR USE IN A CUBESAT

8.4.1. O/F optimization

The thruster designed in this thesis work has largely been optimized for I_{sp} performance and small package size. It has however come to light that other requirements are indeed important to Hyperion Technologies, particularly robustness of design and maximising impulse density of the system.

The O/F ratio was selected at 10 as this provides the optimum in terms of I_{sp} performance. However, if one were to design for maximum impulse density, as is desirable in a satellite where volume is limited such as a CubeSat, the optimum exists somewhere in the direction where more dense propellant is favoured. In this case, that would be N_2O which has almost twice the liquid density of C_2H_6 , depending on ambient temperature. This would mean an O/F ratio greater than 10 would be favoured.

Hyperion also identified that system robustness, particularly in performance, was an important design parameter. This means that regardless of the satellite state (temperature, current orientation, propellant levels etc) the thruster should provide consistent performance. In testing, it was found that the feedsystem, due to the choking orifices, was prone to blocking either partially or fully during operation. The fuel was found to block far more often than the oxidizer, likely due to the much smaller orifice used to achieve an O/F of 10. This problem could be reduced if a lower O/F was selected, allowing the fuel orifice to be larger and hence less prone to blockage, yielding a more robust system. Of course this choice would have a negative effect on both I_{sp} and impulse density of the system if the O/F is reduced below 10.

8.4.2. $P_{Chamber}$ optimization

In a similar manner, the $P_{Chamber}$ used can be optimized to better suit a CubeSat application. If the chamber pressure is raised, the thruster package will become smaller and hence require less space. This will become even more important if a thrust vector control (TVC) system is required as previously discussed in Section 8.2. Furthermore, a physically smaller thruster will mean less area is available to radiate heat and hence the radiative heat transfer to the CubeSat will be decreased.

Contrary to the previous paragraph, the designer may want to optimize the chamber to be easily machinable and hence have large features. This would require that $P_{Chamber}$ be decreased to increase the nozzle

throat and injector port diameters. This would have the added effect of increasing the operating temperature range in which the feed system can perform. For more information on temperature effects on the feedsystem, please refer to the MSc thesis of T. Knop [26].

8.5. ELECTRICAL REQUIREMENTS

The thruster requires some power to operate. In the test series of HypT12-17, a spark of 2 W constant power was used successfully to ignite motor 4. The valves used in this test were industrial solenoids. Each required 19 W to operate. These valves are inappropriate for satellite use and hence no requirement for valve actuation power can be given here. The spark was found to generate some electromagnetic interference (EMI) and caused interference on pressure sensor measurements. This may also have an effect on the operation of other unshielded electronics within the satellite. Shielding of sensitive components should be considered.

8.6. CUBESAT MANOEUVRABILITY

From section 6.4 it was found that the maximum thruster total impulse achieved in a single burn was 162 Ns. If this thruster had been on a 6U CubeSat, it would have been able to perform some substantial manoeuvres. These possible manoeuvres will be calculated here for a 6U CubeSat which is assumed to have a starting mass of 8 kg. The propellant mass used is given by equation 8.2.

$$\text{Propellant mass used} = \frac{\text{Total impulse}}{I_{spvac} * 9.81} = \frac{162}{285 * 9.81} = 0.058 \text{ kg} \quad (8.2)$$

From Tsiolkovsky rocket equation, 8.3, the ΔV can be found.

$$\Delta V = I_{sp} * g * \ln \frac{m_{start}}{m_{final}} = 285 * 9.81 * \ln \frac{8}{8 - 0.058} = 20.3 \frac{m}{s} \quad (8.3)$$

From Figure 8.3 it can be seen that a ΔV per burn of $20.3 \frac{m}{s}$ would achieve an orbit raise manoeuvre from 450 to 520 km circular, using 2 impulsive shots. This was calculated using NASA's open source DAS [6].

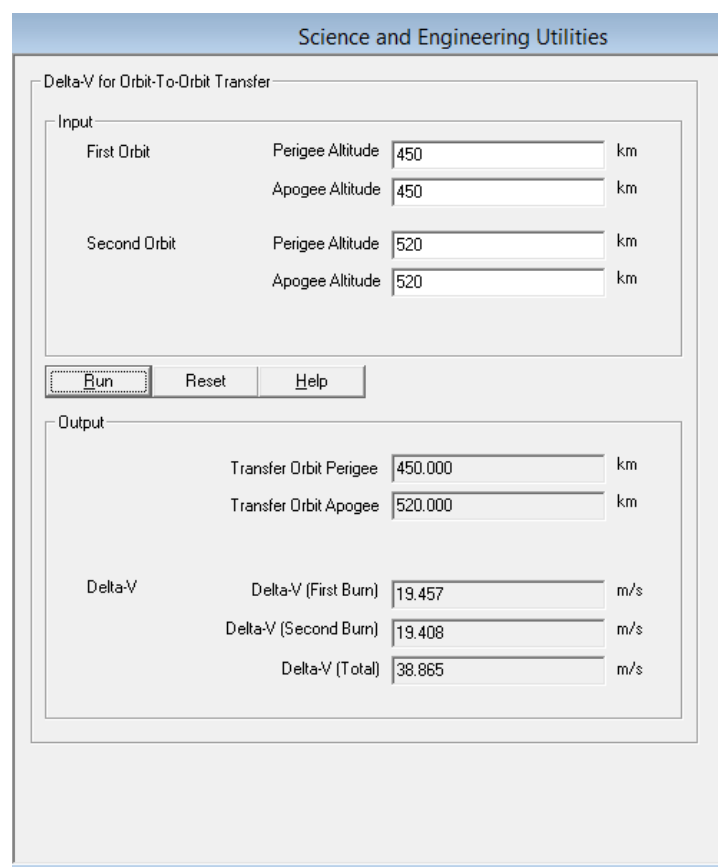


Figure 8.3: DAS output showing the ΔV requirements for a transfer from 450 to 520 km circular orbit transfer

8.7. VACUUM THRUSTER FORM FACTOR

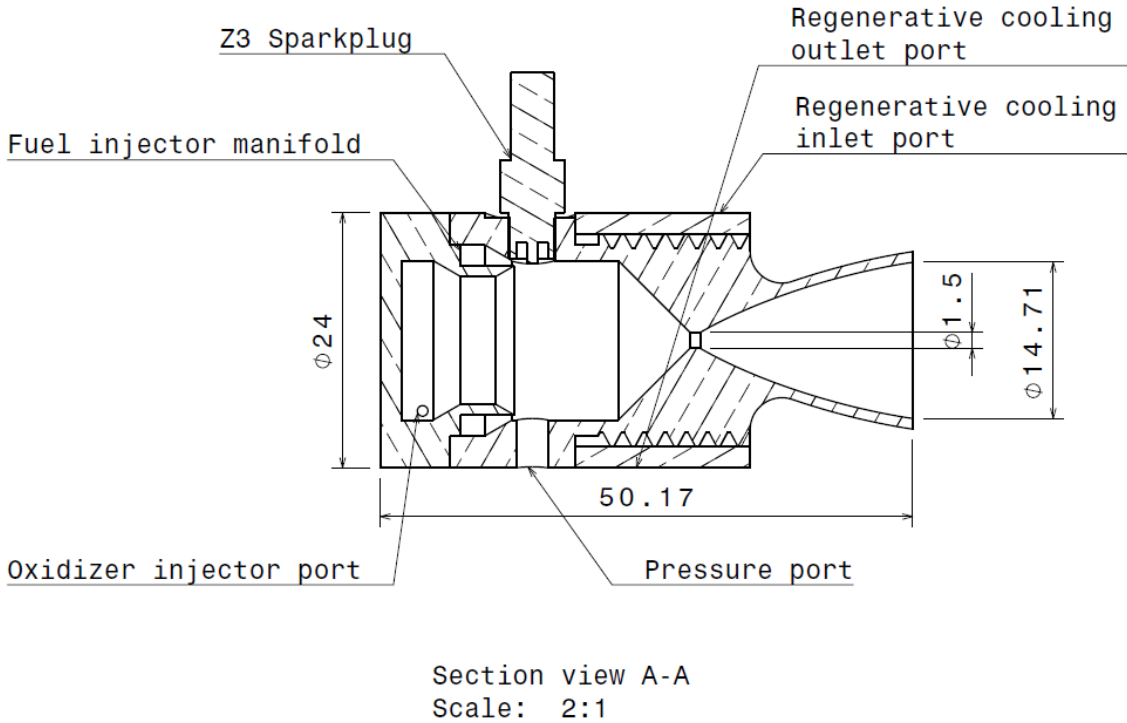


Figure 8.4: Motor 4 configured for vacuum operation, $\frac{A_e}{A_t} = 100$, 80% length bell shaped

8.8. THERMAL DESIGN

Operating a thruster on a CubeSat presents a substantial thermal design challenge. CubeSats do not typically deal with heating sources in the order of hundreds of watts as they typically do not have any high power systems on board, hence it is not standard for them to have any substantial thermal control system. On larger satellites, thrusters are typically mounted on the exterior of the craft where they can effectively radiate to space. In a CubeSat, this is not possible as all componentry must be mounted within the standard CubeSat box and outer surfaces are often reserved for solar arrays.

For the thermal design, the motor can be modelled as a radiative heat source with a given surface temperature. The surface temperature when the motor is operating at equilibrium was never determined experimentally, but has been simulated where it was found that motor 4 had a maximum surface temperature 900K.

The total radiative heat transfer from the motor casing is given by Equation 8.4 where σ is the Stefan-Boltzmann Constant ($5.6703 * 10^{-8} \frac{W}{m^2 K^4}$), T_b is the emitting body temperature (900K), T_a is the ambient temperature (288K), and A is the area ($3.63 * 10^{-3} m^2$).

$$q = \sigma * (T_b^4 - T_a^4) * A = 5.6703 * 10^{-8} * (900^4 - 288^4) * 3.63 * 10^{-3} = 133 W \quad (8.4)$$

As shown above, the CubeSat will encounter a heat source of approximately 133 W. This will likely require some system to either cool the surroundings or insulate the CubeSat from the thruster. Of course, insulating the CubeSat from the thruster will cause the thruster to be unable to effectively reject as much heat, causing it to run at a higher temperature and potentially fail. Further analysis on this topic is outside the scope of this thesis.

9

FUTURE WORK

During the course of this thesis, many phenomena were encountered, resulting in either delays in the project or difficulties in development. While many of these issues have been identified, they have for the most part not been fully understood or solved. This section will detail the areas of improvement required to develop the test prototype further into a working component and later into an integrated part of a CubeSat [ADCS](#).

9.1. MEASUREMENT ACCURACY

In this thesis, an attempt to measure the performance of the various motors was made. It was found that the measurement error was quite large, resulting in a wide range of results. Much of the error originated from natural manufacturing variation due to the simple manufacturing techniques employed. For future motor designs, it would be useful to refine the manufacturing technique such that consistent test articles can be produced. This will greatly aid in the designer's analysis of the motor performance but also to ensure that the product produced is of a consistent quality. This is essential if the motor is to perform on orbit as the designer intends.

Section 6.9 showed that the largest errors exist from estimation of the effective drilling area of both the fuel and oxidizer injectors as well as the nozzle throat. This error could be reduced with by improving the manufacturing tolerance or by characterisation of the injectors and nozzle experimentally. This would yield a 'coefficient of flow' which combines both the area and coefficient of discharge, and hence reduces error on both fronts. Of course, this requires an accurate characterisation system and another operation which requires more time and investment. Alternatively, the injector and throat area could be accurately measured using specialist tools.

9.2. FEED SYSTEM IMPROVEMENTS

From the test results, particularly Figure 6.39, it can be seen that the feedsystem often provides an erratic mass flow rate to the motor, resulting in widely varying motor performance and in many cases, violent starting behaviour. If such behaviour occurs in on a satellite, it could potentially damage vibration sensitive parts such as reaction wheels, solar panels and antennas. Hence, ensuring the feedsystem can provide consistent flow rates to the motor is essential to the flight implementation of the thruster.

The startup and shutdown transients measured during testing resulted in a minimum impulse bit in the order of 6 Ns, six times the required 1 Ns. It was found that reducing the downstream feedsystem volume significantly reduced the shutdown transient and hence the minimum impulse bit. Once testing moves away from a breadboard-type setup utilizing large feedsystem volumes, the startup and shutdown transients will shorten and hence the minimum impulse bit will decrease. Since the startup and shutdown transient lengths are linear with the feedsystem volume, the flight system should reduce the feedsystem volume by at least a factor of 6. Furthermore, the oxidizer and fuel feedsystem volumes should be of equal ratio to the expected volume flow, such that both systems fill and empty at equal rates. This will stop one propellant leading another such as occurred during testing.

The feedsystem could be further improved if a variable orifice system could be implemented whereby the mass flow can be controlled to achieve a desired O/F ratio and $P_{Chamber}$. This would allow the designer to perform much more consistent tests by controlling these variables and hence aid development greatly.

9.3. MOTOR OPTIMIZATION

The last motor presented in this thesis, motor 4, satisfied many of the design requirements, particularly in $I_{sp\ vac}$ where it exceeds the requirements by 18%. While extra $I_{sp\ vac}$ is always welcome, it comes at the cost of other performance parameters which could otherwise be improved, potentially at limited cost in $I_{sp\ vac}$.

The contraction ratio and O/F ratio of the motor, which was determined very early on in the design process, should be revisited to take into account newly obtained knowledge. Particularly, the numerical analysis tools can be used to determine the optimum for these parameters as it was found to agree with experimental results much more closely than the simple analytical tools originally used. This has been further elaborated on in Section 8.4.1.

$P_{Chamber}$ can be optimized either towards manufacturability (lower $P_{Chamber}$) or small thruster form factor (higher $P_{Chamber}$). This has been discussed at length already in Section 8.4.2

Finally, the thruster should be designed such that it can operate at thermal equilibrium. This will require a thermal model, similar to that which was developed in Section 4.3 and then suitable material selection and production.

It is apparent that the motor design needs to be looked at in a more holistic way to find the optimum design parameters. Not only motor performance parameters but also radiative heat transfer to the satellite and the selected machining process need to be considered before factors such as chamber pressure and O/F can be selected in a constructive manner.

9.4. INVESTIGATE HIGH FREQUENCY INSTABILITY (600HZ)

Testing identified a number of combustion instabilities, most of which were feedsystem coupled and could be relatively simply solved. However a higher frequency instability, at 600 Hz in motor 3 and 250 Hz in motor 4, have not been isolated and the root cause is yet unknown. While the instability does not appear to have a severely detrimental effect on the motor performance, it is the major contributor to motor vibration and is therefore undesirable. It is also possible high frequency instabilities will lead to failure of motor components due to fatigue in long duration testing. Therefore it is desirable to understand the cause of these instabilities and eliminate them before implementing the motor into a flight system.

9.5. FURTHER TESTING

The time and resource allocated to this thesis was limited and as such only a limited set of tests could be performed. Also, hardware was regularly damaged during testing due to inadequate design. In fact, testing of a given motor was only halted once it had been damaged beyond a usable state.

The testing conducted was focused firstly on verifying instantaneous performance parameters such as C* efficiency and combustion stability, followed by single burn performance parameters such as startup and shutdown transients, minimum impulse bit and maximum burn time. Limited work was done on repeatability tests where multiple burns were repeated with the same motor and at the same initial condition. Such tests usually resulted in the eventual overheating of the motor as was the case for motors 3 and 4. Further testing should be conducted to better evaluate the repeatability of the system as well as the effects of multiple cold restarts. An on-orbit system may require hundreds of restarts over its lifetime, thus it should be verified that the system can achieve this. In particular, thermal cycling of sensitive components such as the spark plug may not satisfy this requirement due to soot build-up or cracking of the ceramic materials used in them.

Full duration testing of the system should also be performed to verify that 100s burn times can be achieved as required.

Thrust of the motor was found by first determining the combustion performance of the motor and then

estimating the vacuum thrust using standard nozzle efficiency factors and theoretical performance values. While this technique is a well established method of motor performance evaluation, it is recognised that it introduces more errors than are necessary if a direct thrust measurement can be made. Thrust could be measured directly putting the thruster on a thrust bench with a sea level expansion nozzle. The thrust obtained at sea level can then simply be converted to a vacuum equivalent thrust. This can be taken a step further by testing a flight version of the thruster with a vacuum expansion nozzle in a vacuum chamber to experimentally determine the vacuum performance of the thruster, as is typically done for space bound thrusters. This approach would yield the highest fidelity performance measurements possible without actually flying the thruster in space but requires costly testing equipment.

During testing, it was found that surface thermocouple measurements became erratic in some instances, yielding low quantity data. It was found that this was likely because the aluminium tape used to secure the thermocouple did not adhere to the test article well at temperatures above 300 deg C. Furthermore, it served to insulate the motor and even caught fire, altering the measurement by an unknown amount. Both of these issues could be solved if the thermocouples were to be soldered directly to the test article, achieving a much better connection which would be resistant to higher temperatures without significantly altering the measurement.

9.6. REQUIREMENTS VERIFICATION

The requirements set by Hyperion Technologies were based largely on 'intuitive market feeling'. They have been designed such that a propulsion system, applicable to any conceivable CubeSat mission, would be developed. This has resulted in some of the requirements being unnecessarily difficult to achieve and thus become driving requirements. An example of this is the required minimum burn time of 100s. Such a long burn time is only practically achievable using regenerative cooling. This makes the design require a much more complex cooling system and hence understanding of the thermal interaction in the motor. It has been demonstrated with motor 2 that a capacitively cooled motor can also produce satisfactory I_{sp} performance while maintaining a very simple design. It has not been shown that a 6U CubeSat could practically use a 100s burn time, nor that there is any demand for such capability. Hence, this requirement may be an unnecessary and costly design challenge.

All top level requirements should be verified to ensure that they do indeed flow down from higher operational requirement of the intended CubeSat on which the thruster system should fly. This is necessary to ensure the thruster system is optimized according to valid performance requirements.

9.7. INTEGRATION OF FEEDSYSTEM TO THRUSTER IN A CUBESAT CONFIGURATION

This thesis has established that a 4N N_2O , C_2H_6 thruster is a viable propulsion concept for a 6U CubeSat on a component level. The next step in showing that a flight system can be realised is to integrate motor 4 into a 2U CubeSat format which includes propellant management system and TVC system, flight valves, electronics and other flight components. A major challenge will be finding appropriate COTS components such as solenoid valves, ball valves, check valves, pressure sensors and mass flow measuring devices in a package size which is suitable for a CubeSat and integrating them into a small package.

Furthermore, the thermal design of the satellite will present a major challenge. It has been shown that the proposed system will produce more than 133 W of radiative heat to the satellite. This heat has to be ejected or managed in a suitable way such that the satellite doesn't overheat. A thorough understanding of the thermal situation will be critical when considering the location of each component and the heat it will be exposed to during thruster operation. Much work is to be done in this area before a system can be assembled.

10

CONCLUSION

A working prototype 4N N_2O , C_2H_6 motor has been successfully designed and tested in this thesis according to the design requirements set by Hyperion Technologies. The motor was designed using a combination of analytical models and commercial numerical multi physics solvers. The motor was chosen to run at $P_{Chamber} = 15$ bar, an O/F ratio of 10, use regenerative cooling of the oxidizer and to be restartable via a spark igniter. The design was tested at TU Delft to evaluate performance parameters such as combustion efficiency, combustion stability and maximum achievable burn time amongst others. Four design iterations were manufactured and a total of 7 test campaigns performed. Motor 4 demonstrated a C* efficiency of between 91 and $96\% \pm 11\%$ and a maximum burn time of 30 seconds. Not all performance parameters specified by Hyperion technologies could be achieved, particularly requirements on minimum impulse bit could not be achieved due to the large breadboard style feedsystem used in the prototype stage. It is expected this will be solved once the system is moved to a more flight like system where feedsystem fluid volumes are much lower.

Several major difficulties were encountered in the development of the motor. It was found that an insufficient pressure drop over the fuel and/or oxidizer injector brought on by either bad design or due to low mass flow would lead to feedsystem coupled instabilities between 100 and 140 Hz. In some cases this would lead to the motor extinguishing entirely. Instabilities at 250 Hz were also observed and appear to increase in strength with increasing oxidizer injection velocity.

The numerical multi physics model showed good agreement with experimentally obtained data in the areas of regenerative cooling fluid and motor surface temperatures. Although the model appears to be somewhat correct in predicting C* efficiency, no conclusion could be drawn due to the high error of the measured C* efficiency, hence agreement here could be merely coincidental.

It was found that such a propulsion system will emit 130 W of thermal energy to its surroundings, much of which is likely to be the CubeSat itself. This will impose stringent requirements on the satellite in the areas of thermal heat transfer. The thruster will also require either substantially more powerful ADCS actuators or a TVC system if the satellite is to handle the adverse torque due to thrust misalignment with the satellite's centre of mass.

The final motor is 50 mm long and 24 mm in diameter in vacuum configuration and hence can fit into a single unit of a CubeSat. Motor 4 has demonstrated the performance required to raise the orbit of 6U CubeSat from 450 to 520 km.

This thesis has served to raise the TRL of bi-propellant technology for CubeSat applications however further design iterations are necessary to achieve all design requirements specified by Hyperion Technologies. Once this is achieved, the motor can be integrated system for use in a CubeSat.

Many lessons were learnt throughout the course of this research. The author now has a more profound understanding of how theoretical analysis and experimental can be effectively used together to develop a complex system. The lack of accuracy of numerical models can be supplemented well with experimental data while the design iteration time can be reduced from a week with an experimental motor to a matter of

hours if performance is evaluated numerically. Together, these techniques have allowed for a development schedule seldom achieved in a MSc thesis.

If this research were be repeated, more attention should be paid to requirements validation. It is quite possible that some requirements were much stricter than necessary for the standard use case of a 6U CubeSat. This lead to the requirements becoming driving and forcing complex design solutions which otherwise could have been avoided.

A

KELLER 23SY PRESSURE SENSOR DATA SHEET



PIEZORESISTIVE PRESSURE TRANSMITTERS

ABSOLUTE AND GAUGE PRESSURE / ACCURACY 0,25 %FS

The Y-line transmitters have an extremely small temperature error. This is achieved using an additional circuit containing a temperature sensor that subdivides the temperature range into fields that are 1,5 Kelvin (K) wide. The TK zero and TK compensation values are calculated for each field and programmed into the additional circuit. During operation, these values are fed into the analogue signal path depending on the temperature. Each temperature is the „calibration temperature“ for this transmitter. The accuracy thereof is mainly determined by linearity. 120 fields are available, representing a possible temperature range of 180 K. The wider the temperature range, the greater the amount of testing that is needed to minimise the inaccuracy of the mathematical model.

The Series 23 SY / 25 Y product line is outstanding due to its extreme ruggedness towards electromagnetic fields. The limits of the CE standard are undercut by a factor of up to 10 with conducted and radiated fields.

- Series 23 SY Ranges 0,1...1000 bar Fully welded (no internal seals)
- Series 25 Y Ranges 0,5...100 bar Flush, fully welded.

A Comprehensive Range

Absolute, barometric, gauge (positive and negative pressures). Many nominal pressure ranges. Current or voltage output.

Flexibility

A modular concept is used, with fast and economical production achieved by using off-the-shelf sensors. Numerous options and variations are available to meet customers' specific requirements: Pressure ranges, pressure ports, signal outputs, electrical connectors, etc.

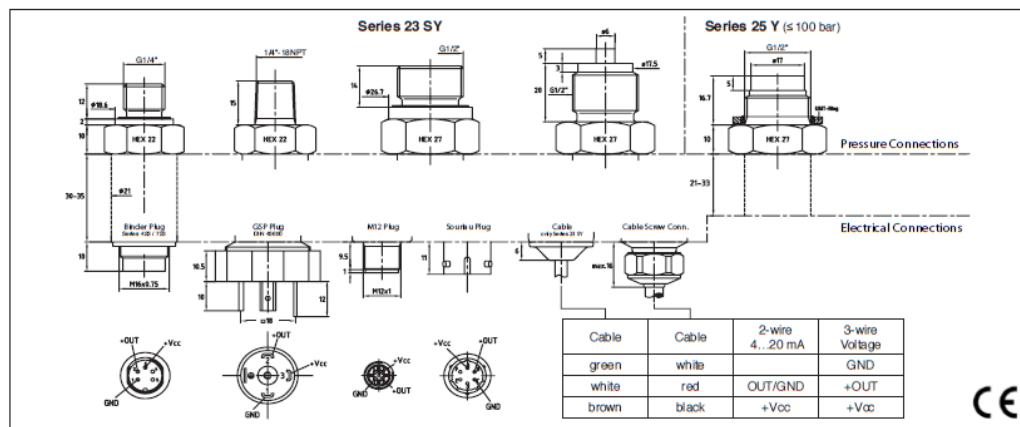
SERIES 23 SY / 25 Y



Series 23 SY



Series 25 Y



Subject to alterations

06/2015

KELLER AG für Druckmesstechnik	St. Gallerstrasse 119	CH-8404 Winterthur	Tel. +41 (0)52 - 235 25 25	Fax +41 (0)52 - 235 25 00
KELLER Ges. für Druckmesstechnik mbH	Schwarzwaldstrasse 17	D-79798 Jestetten	Tel. +49 (0)7745 - 9214 - 0	Fax +49 (0)7745 - 9214 - 60

Companies approved to ISO 9001

www.keller-druck.com



KELLER

Specifications

Pressure Ranges (FS) in bar

PR-23 SY	-1 -0,5 -0,2 -0,1 0,1 ±0,1 0,2 ±0,2 0,5 ±0,5	1 ±1 2 5 10 20
PA-23 SY	-1	1 ±1 2 5 10 20 50 100 200 400 600 1000 ⁴⁾
PAA-23 SY		0,5 1 2 5 10 20 50 100 200 400 600 1000 ⁴⁾
PR-25 Y	-1 -0,5	0,5 ±0,5 1 ±1 2 5 10 20
PA-25 Y	-1	1 ±1 2 5 10 20 50 100
PAA-25 Y		0,5 1 2 5 10 20 50 100
Overpressure	-1 -1 -1 -1 4 4 4 4 4 12 12 40 40 80 80 200 300 1100 1100 1100	

PR: Vented Gauge. Zero at atmospheric pressure

PA: Sealed Gauge. Zero at 1000 mbar abs.

PAA: Absolute. Zero at vacuum

Pressure Range	Linearity ¹⁾	Error Band @ 0...50 °C ²⁾		Error Band @ -10...80 °C ²⁾	
		typ.	max.	typ.	max.
> 2...1000 bar	±0,25 %FS	±0,3 %FS	±0,5 %FS	±0,4 %FS	±0,7 %FS
> 0,3...2 bar	±0,25 %FS	±0,6 %FS	±1,0 %FS	±0,8 %FS	±1,5 %FS
0,1...0,3 bar ³⁾	±0,50 %FS	±2 mbar	±3 mbar	±2,5 mbar	±4,5 mbar

¹⁾ Best fitted straight line, including Hysteresis + Repeatability

²⁾ Linearity + Hysteresis + Repeatability + Temp. Coeff. + Zero + Span Tolerance

³⁾ Pressure Range 0,1 bar: Linearity ±1 %FS Max; Signal output limited to 4...20 mA / 0...5 V / 0...10 V

⁴⁾ Measuring range 1000 bar only suited for static applications

Storage-/Operating Temperature -40...100 °C

Stability	Range > 2 bar	0,1 %FS typ.	0,2 %FS max.
	Range ≤ 2 bar	2 mbar typ.	4 mbar max.

Type	2-wire	3-wire	3-wire	3-wire
Signal Output	4...20 mA	0...10 V	0...5 V	0,5...4,5 V
Limitation Signal Output	3,2...22,3 mA	-1,2...11,2 V	-0,6...5,6 V	0,1...4,9 V
Supply	8...32 VDC	13...32 VDC	8...32 VDC	8...32 VDC
Load Resistance	< (U-8 V) / 0,025 A	> 5 kΩ	> 5 kΩ	> 5 kΩ
Limiting Frequency	2 kHz	2 kHz	2 kHz	2 kHz
Power Consumption		max. 5 mA	max. 5 mA	max. 4 mA
Electrical Connection	- Plug: Binder-423/723 (5-pole), GSP (DIN 43650), M12 (4-pole), Souriau (MIL-C26482) - Cable			
Pressure Connection	Series 23 SY:	G1/4", 1/4"-18NPT, G1/2", G1/2" Mano		
	Series 25 Y:	G1/2"		
Response Time (Supply ON)	(0...99 %) < 5 ms			
Insulation	> 10 MΩ @ 300 V			
EMC	EN 61000-6-2: 2005 / EN 61000-6-3: 2007 / EN 61326-2-3: 2006			
Dead Volume Change	< 0,1 mm³			
Material in Media Contact	- Stainless Steel AISI 316L (1.4404/1.4435) - USIT or Viton® O-Ring (no internal seals)			
Protection Class	Plug: IP65...IP67 (depending on connection and with corresponding mating plug) Cable: IP54	Cable Screw Connection: IP68		
Weight	= 120 g (depending on version)			
Endurance	> 10 million cycles, 0...100 %FS at 25 °C ⁴⁾			
Oil Filling	Silicone oil			

Options

Temperature Range	Other temperature ranges on request. Maximal range: -40...+120 °C
Oil Filling	Fluorocarbon oil (O ₂ -compatible), olive-oil, lowest temperature oil (-55 °C)
Pressure Ranges	Intermediate ranges on request, e.g. barometer 0,7...1,2 bar abs.
Pressure Connection, Electrical Connection	Others on request
Intrinsic Safety (ATEX)	See also data sheet 23 SY EI / 25 Y EI / 26 Y EI

Subject to alterations

06/2015

KELLER AG für Druckmesstechnik
KELLER Ges. für Druckmesstechnik mbH

St. Gallerstrasse 119
Schwarzwaldstrasse 17

CH-8404 Winterthur
D-79798 Jestetten

Tel. +41 (0)52 - 235 25 25
Tel. +49 (0)7745 - 9214 - 0

Fax +41 (0)52 - 235 25 00
Fax +49 (0)7745 - 9214 - 60

Companies approved to ISO 9001

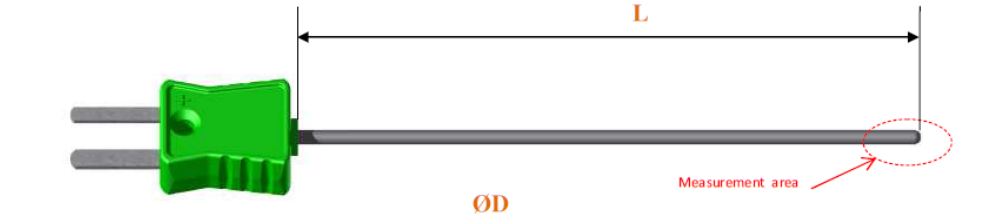
www.keller-druck.com

B

DTMTC8 K TYPE THERMOCOUPLE DATA SHEET

RS Stock No. 8240622
RS Stock No. 8240622

Data sheet DTMTC8

 <p>THERMOCOUPLES SHEATHED WITH MINERAL INSULATION MINIATURE CONNECTOR</p>																		
RANGE :																		
<ul style="list-style-type: none"> -50°C / +1200°C 																		
USE :																		
<ul style="list-style-type: none"> Universal 																		
KEY POINT :																		
<ul style="list-style-type: none"> Unanswerable connection 																		
SPECIFICATIONS:																		
<ul style="list-style-type: none"> Thermocouple K type (Nickel/Chrome-Nickel/Aluminium) Hot junction ungrounded Sheath material: Alloy 600 Mineral pressed insulation Bendable Overmoulded male miniature connector with compensated sprongs, Ambiente temperature : -50°C/+200°C 																		
DIMENSIONS:																		
<ul style="list-style-type: none"> Sheath length - L = 100 mm Sheath diameter - ØD = 1.5 mm Connector = 20x16x8mm 																		
METROLOGICAL DATA :																		
<ul style="list-style-type: none"> As per IEC 584 <i>Standard tolerance TC "K" class 1 :</i> $-40^{\circ}\text{C} < t' < +375^{\circ}\text{C} = \pm 1,5^{\circ}\text{C}$ $375^{\circ}\text{C} < t' < +1000^{\circ}\text{C} = \pm 0.004 \cdot [t]$ Time constant at in water: <2s Output signal FEM (mV) as per curve of "K" type as per norm 																		
Other dimensions: <table border="1"> <thead> <tr> <th>Diameter</th> <th>Length 100mm</th> <th>150mm</th> <th>250mm</th> <th>500mm</th> <th>1000mm</th> </tr> </thead> <tbody> <tr> <td>1mm</td> <td>8240603</td> <td>8240607</td> <td>8240616</td> <td>8240619</td> <td>8240613</td> </tr> <tr> <td>1,5mm</td> <td>8240622</td> <td>8240625</td> <td>8240629</td> <td>8240638</td> <td>8240631</td> </tr> </tbody> </table>	Diameter	Length 100mm	150mm	250mm	500mm	1000mm	1mm	8240603	8240607	8240616	8240619	8240613	1,5mm	8240622	8240625	8240629	8240638	8240631
Diameter	Length 100mm	150mm	250mm	500mm	1000mm													
1mm	8240603	8240607	8240616	8240619	8240613													
1,5mm	8240622	8240625	8240629	8240638	8240631													



BIBLIOGRAPHY

- [1] C. Verhoeven, *On the origin of satellite swarms*, Acta Astronautica **68**, 1392 to 1395 (2011).
- [2] B. T. J. P. Suari, *CubeSat Design Specification*, California Polytechnic State University, San Luis Obispo, rev. 13 ed. (2014).
- [3] D. T. Schmuland, *Hydrazine propulsion module for cubesats*, in *Small Sat Conference* (2011).
- [4] R. K. M. Derek T. Schmuland, Christian Carpenter, *Mission applications of the mrs-142 cubesat high-impulse adaptable monopropellant propulsion system (champs)*, in *48th AIAA/ASME/SAE/ASEE Joint Propulsion Conference & Exhibit* (2012).
- [5] J. B. G. B. E. G. Monna, *Design status of the delfi-next nanosatellite project*, in *International Astronautical Congress 2010* (International Astronautical Federation, 2010).
- [6] NASA, *Debris assessment software*, <http://orbitaldebris.jsc.nasa.gov/> (2015).
- [7] E. G. P. S. J. B. B. Z. R. Reinhard, *Formation flying within a constellation of nano-satellites: The qb50 mission*, in *International Workshop on Satellite Constellation and Formation Flying* (2010).
- [8] S. Powell, *A miniaturized bi-propellant rocket engine thruster*, (2015), literature Study.
- [9] O. B. George P. Sutton, *Rocket Propulsion Elements* (John Wiley & Sons, 2011).
- [10] M. Barrere, *Rocket Propulsion* (Elsevier publishing company, 1960).
- [11] D. H. D.K. Huzel, *Design of Liquid Propulsion Rocket Engines* (National Aeronautics and Space Administration, 1967).
- [12] B. Zandbergen, *AE4-S01 Thermal Rocket Propulsion Course Notes* (TU Delft, 2014).
- [13] S. C. S. Whitmore, *Engineering model for self-pressurizing saturated-n₂O-propellant feed systems*, JOURNAL OF PROPULSION AND POWER (2010).
- [14] D. L. N. Hay, *The discharge coefficient of flared film cooling holes*, in *International Gas Turbine and Aero-engine Congress and Exposition* (1995).
- [15] *Coolprop opensource fluid properties code*, (2015).
- [16] C. J. S. H.F.R. and W. K.F, *Rocket Propulsion and Space Flight Dynamics*, edited by C. J.W (Pitman Publ. Ltd., 1979).
- [17] M. B. Frank Kreith, Raj Manglik, *Principles of Heat Transfer*, edited by S. Meherishi (Global Engineering, 2011).
- [18] G. Z. Laura Simurda, *High performance hybrid propulsion system for small satellites*, in *49th AIAA/ASME/SAE/ASEE Joint Propulsion Conference* (2013).
- [19] D. L. Ellis, *CRCop-84: A High Temperature Copper Alloy for High-Heat-Flux Applications*, Tech. Rep. (Glenn Research Center, Cleveland, Ohio, 2005).
- [20] F. B. Nicolas Bellomo, Marta Lazzarin, *Numerical investigation of the effect of a diaphragm on the performance of a hybrid rocket motor*, in *46th AIAA/ASME/SAE/ASEE Joint Propulsion Conference & Exhibit* (2010).
- [21] N. B. M. F. F. Barato and M. Lazzarin, *Numerical model to analyze transient behavior and instabilities on hybrid rocket motors*, Journal of Propulsion and Power **31**, 643 (2015).

- [22] K. M. Antoniou, A. Akyuzlu, *A physics based comprehensive mathematical model to predict motor performance in hybrid rocket propulsion system*, in *41th AIAA/ASME/SAE/ASEE Joint Propulsion Conference & Exhibit* (2005).
- [23] C. Guobiao and T. Hui, *Numerical simulation of the operation process of a hybrid rocket motor*, in *42th AIAA/ASME/SAE/ASEE Joint Propulsion Conference & Exhibit* (2006).
- [24] K. Kuo, *Fundamental Phenomena on Fuel Decomposition and Boundary-Layer Combustion Process with Applications to Hybrid Rocket Motors*, Final Report for Contract no. NAS8-39945, , Mechanical Engineering Department (Propulsion Engineering Research Center, The Pennsylvania State University, University Park, PA, 2008).
- [25] P. Zarchan, *Liquid Rocket Thrust Chambers: Aspects of Modeling, Analysis, and Design*, edited by P. Zarchan (American Institute of Aeronautics and Astronautics, 2005).
- [26] T. Knop, *A Mass Flow Model for Self-Pressurizing Propellants in Chemical Micro-Propulsion Systems*, Master's thesis, TU Delft (2015).
- [27] Morrison and M. E. Works, *Rimfire z3 spark plug*, <http://sparkplugs.morrisonandmarvin.com/z3.php> (2015).
- [28] K. O. Kverneland, *Metric Standard for Worldwide Manufacturing* (International Organization for Standardization, 2012).
- [29] S. W. C. K. H. Lee, *Interaction effect analysis of thruster plume on leo satellite surface using parallel dsmc method*, *Selected contributions of the 23rd International Conference on Parallel Fluid Dynamics*, Selected contributions of the 23rd International Conference on Parallel Fluid Dynamics **Volume 80**, 333 (2013).
- [30] I. D. Boyd, *Interactions between spacecraft and thruster plumes*, Journal of Spacecraft and Rockets **38** (2001).
- [31] H. Trinks, *Experimental investigation of bipropellant exhaust plume flowfield, heating and contamination, and comparison with the contam computer model predictions*, in *AIAA 18th Thermophysics Conference* (1983).